MARINE GEOLOGICAL INSTITUTE

GEOLOGICAL AGENCY
MINISTRY OF ENERGY AND MINERAL RESOURCES
Jalan Dr, Junjunan No. 236, Bandung-40174, Indonesia
http://www.mgi.esdm.go.id, E-mail: ejournal.p3gl@gmail.com

ISSN 1410 - 6175

BULLETIN OF THE MARINE GEOLOGY VOLUME 40, NUMBER 2, DEC. 2025 - ISSN 1410-6175

ISSN 1410-1675

BULLETIN OF THE MARINE GEOLOGY

VOLUME 40 • NUMBER 2 • DEC. 2025

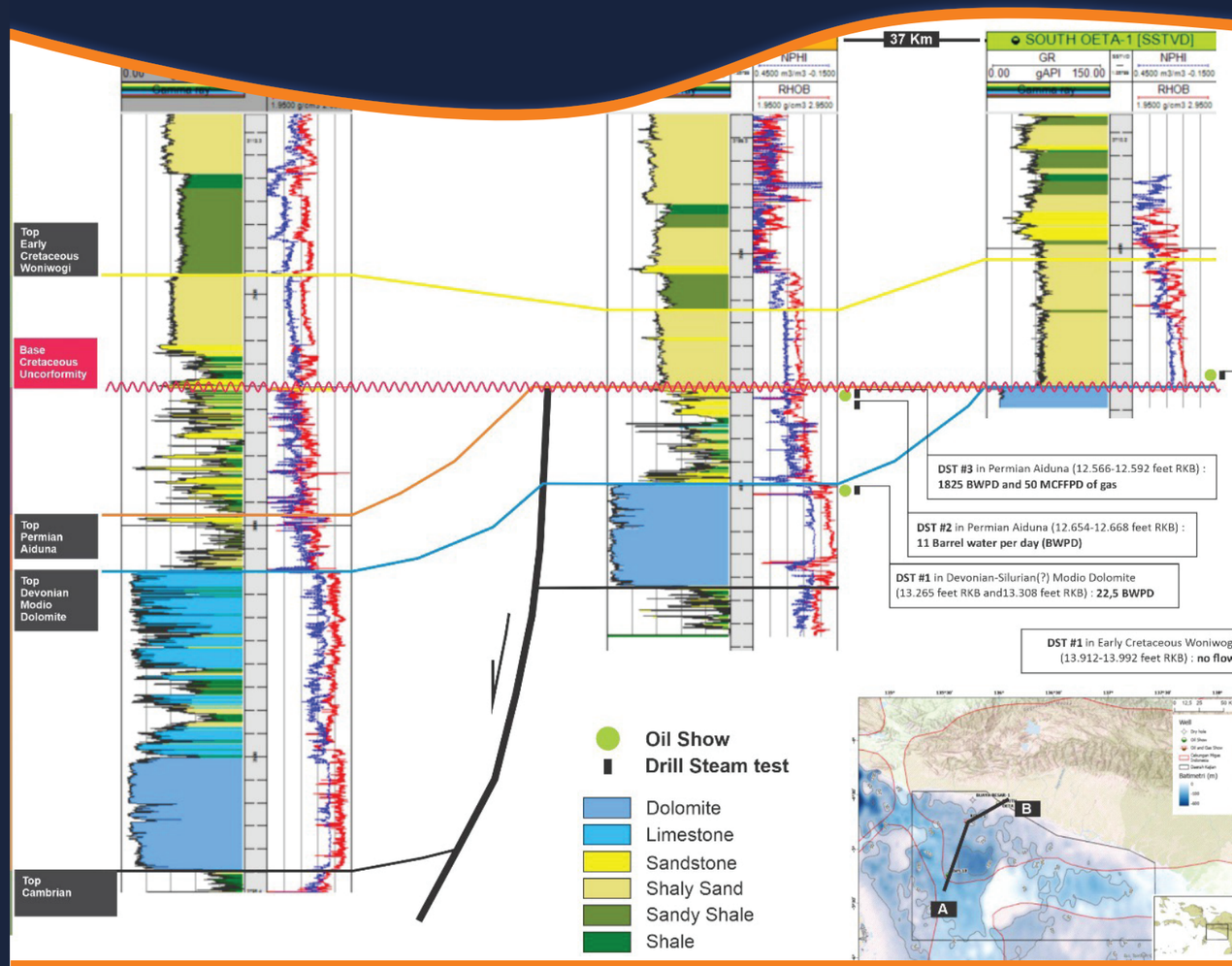

BoMG	VOL. 40	NO. 2	P. 75-149	BANDUNG, DEC. 2025	ISSN 1410-6175

Accredited : RISTEK-BRIN 200/M/KPT/2020

MARINE GEOLOGICAL INSTITUTE
GEOLOGICAL AGENCY
MINISTRY OF ENERGY AND MINERAL RESOURCES

BALAI BESAR SURVEI DAN PEMETAAN GEOLOGI KELAUTAN
BADAN GEOLOGI
KEMENTERIAN ENERGI DAN SUMBER DAYA MINERAL

BULLETIN OF THE MARINE GEOLOGY

Vol. 40, No. 2, DECEMBER 2025

INSURED EDITOR

Director of Marine Geological Institute

CHIEF OF EDITORIAL BOARD

Imam Setiadi, S.Si., M.T.

VICE CHIEF OF EDITORIAL BOARD

Dra. Ai Yuningsih

EDITORIAL BOARDS

Dr. Luli Gustiantini, S.T., M.T. (Marine Geological Institute of Indonesia)
Siti Marina, S.T., M.Phil. (Marine Geological Institute of Indonesia)
Yulinar Firdaus, S.Si., M.T. (Marine Geological Institute of Indonesia)
Andrian Wilyan Djaja, S.Si., M.T. (Marine Geological Institute of Indonesia)
Sony Mawardi, S.T. (Marine Geological Institute of Indonesia)
Nazar Nurdin, S.T., M.T. (Marine Geological Institute of Indonesia)
Shaska Ramadhan Zulivandama, S.T., M.T. (Marine Geological Institute of Indonesia)
Muhammad Zulfikar, S.T., M.T. (Marine Geological Institute of Indonesia)
Irwan Hidayat Suherman, S.Si. (Marine Geological Institute of Indonesia)
Swasty Aninda Piranti, S.T., M.T. (Marine Geological Institute of Indonesia)
Faris Nauval Rasyid, S.T. (Marine Geological Institute of Indonesia)
Ir. Riza Rahardiawan, M.Sc. (Marine Geological Institute of Indonesia)
Dr. Ir. Noor Cahyo Dwi Aryanto, M.T. (National Research and Innovation Agency)
Dr. Eng. Budi Muljana, S.T., M.T. (Padjajaran University)

SCIENTIFIC REVIEWERS

Dr. Moh. Heri Hermiyanto Z., M.T. (Centre for Geological Survey)
Dr. Ir. Susilohadi (National Research and Innovation Agency)
Dr. Ronaldo Irzon, S.T., M.T. (Centre for Geological Survey)
Dr. Dra. Lia Jurnaliah, M.Si. (Padjajaran University)
Dr. Setianingsih, S.T., M.T. (Bandung Institute of Technology)

PUBLISHER BOARDS

Edi Suhanto, S.Si., M.T.
Bakti Nata Kusumah, S.Si.
Drs. Judy Muliawan Eddy
Nanang Suryana
Dwi Hartanto
Muhammad Abdillah Islamy, S.Pd.
Dwinanda Pratya Annisa M., S.pd.
Widya Anindita, S.Kom.

GRAPHIC DESIGN

Dery Rochiman, A.Md.

For communication of this publications, please contact :
MARINE GEOLOGICAL INSTITUTE
Dr. Junjunan 236, Bandung-40174, Indonesia
Telephone : +62-22-6032020, 6032201, Fax : +62-22- 6017887
E-mail : ejournal.p3gl@gmail.com

Cover Figure : South–north stratigraphic correlation flattened at the base Cretaceous unconformity horizon. (Source: Setiadi, et al, 2025)

Preface

We are pleased to present the second issue of the Bulletin of the Marine Geology (BoMG) for 2025. This edition comprises five peer-reviewed research articles that contribute substantially to the advancement of earth sciences, marine studies, and disaster mitigation in Indonesia. The range of topics highlights the diversity and dynamism of geological and geophysical research within the Indonesian archipelago, a region characterized by abundant natural resources and complex geological processes.

The first article discusses the hydrocarbon potential of the offshore Akimeugah Basin through Mesozoic–Paleozoic geological and geophysical reconstructions, providing new perspectives on petroleum prospects in eastern Indonesia. The second paper examines acoustic facies surrounding the Salahnama and Pandang Island intrusion complexes in the Malacca Strait, offering insights into seafloor sediment characteristics and seismic reflector patterns. The third addresses geohazard issues by identifying earthquake and tsunami risk zones in southern Java using gravity data, contributing to hazard mitigation and regional planning. The fourth article focuses on the geochemistry of marine and coastal sediments in the Limau Waters, aiming to determine sediment provenance, weathering intensity, and maturity to better understand sedimentary processes and support marine mineral exploration. The final paper investigates foraminiferal distribution in the Waipoga Waters, North Papua, to reconstruct paleoenvironmental conditions and Holocene oceanographic changes.

We expect this issue to serve as a valuable scientific reference and to foster broader collaboration in marine geology, geophysics, and disaster studies in Indonesia. We sincerely thank the authors for their high-quality contributions, the reviewers for their constructive and objective assessments, and the editorial team for their commitment to the successful publication of this journal. It is our hope that this edition will provide new insights, enrich scientific knowledge, and benefit researchers, practitioners, academics, and policymakers.

Bandung, December, 2025

Chief Editor

ISSN 1410-6175

BULLETIN OF THE MARINE GEOLOGY

Vol. 40, No. 2, December 2025

Contents

HYDROCARBON POTENTIAL OF THE OFFSHORE AKIMEUGAH BASIN FROM MESOZOIC-PALEOZOIC BASED ON GEOLOGICAL AND GEOPHYSICAL ANALYSIS

POTENSI HIDROKARBON CEKUNGAN OFFSHORE AKIMEUGAH UMUR MESOZOIKUM-PALEOZOIKUMBERDASARKAN ANALISIS GEOLOGI DAN GEOFISIKA

Imam Setiadi[1*], Faris N. Rasyid[1], Shaska R. Zulivandama[1], Yulinar Firdaus[1], Lauti D. Santy[2], Hanif M. Saleh[2], Muhammad G. Rachman[3], Andrian W. Djaja[1], Nazar Nurdin[1],Riza Rahardiawan[1], Sub-arsyah[1]

[1] Marine Geological Institute, Indonesia

[2] Center for Geological Survey, Indonesia

[3] Department of Geological Engineering, UPN Veteran Yogyakarta

*Corresponding author: setiadi_i@yahoo.com

(Received 21 July 2025; in revised from 28 July 2025; accepted 29 December 2025)

DOI : 10.32693/bomg.40.2.2025.954

ABSTRACT: Akimeugah Basin is one of the basins with discovery status, however hydrocarbon production has not yet been established. One of potential petroleum play type for further investigation, estimated to contain hydrocarbon reserves in the offshore Akimeugah Basin, is the Mesozoic–Paleozoic sedimentary play, interpreted to have originated from the Australian passive margin. This study aims to analyze geological and geophysical data to delineate the sub-basin pattern and characterize petroleum system elements. The analysis integrates gravity data interpretation, geochemical evaluation of source rocks, and subsurface interpretation based on seismic and well data. Results indicate that source rocks in the Kola-1 well are primarily composed of Type III (gas-prone) and secondarily of Type II (oil/gas-prone) kerogen. Thermal maturity analysis shows that the Woniwogi, Aiduna, and Modio Formations have reached the oil window. Reservoir potential has been identified in the Tipuma Formation (Triassic), Aiduna Formation (Permian), and Modio Dolomite (Devonian–Silurian). Seal rocks consist of regional and intraformational units composed of tight siltstone and shale. Trapping mechanisms in this area include a combination of structural traps such as fault-bounded anticlines and stratigraphic traps represented by sub-unconformities. Identified exploration leads include seven within the Modio Dolomite structural play, six within the Permian Aiduna Sandstone play, and four within the Triassic Tipuma Sandstone play.

Keywords: gravity, seismic, well, hydrocarbon, offshore Akimeugah

ABSTRAK: *Cekungan Akimeugah merupakan salah satu cekungan dengan status penemuan (discovery basin), namun hingga saat ini belum terdapat produksi hidrokarbon. Salah satu tipe play migas yang diperkirakan memiliki potensi cadangan untuk diteliti lebih lanjut di wilayah cekungan offshore Akimeugah yaitu play type sedimen berumur Mesozoikum dan Paleozoikum yang berasal dari passive margin Australia. Penelitian ini bertujuan untuk menganalisis data-data geologi dan geofisika guna mendelineasi pola subcekungan serta mengkarakteristisasi elemen-elemen sistem petroleum. Analisis data meliputi interpretasi gravity, analisis geokimia batuan induk, serta interpretasi bawah permukaan berdasarkan data seismik dan sumur. Hasil yang diperoleh menunjukkan bahwa batuan induk pada sumur Kola-1 terdiri dari batuan – batuan*

induk tipe III (gas-prone) dan beberapa batuan induk tipe II (oil/gas prone). Batuan induk yang telah mencapai tingkat kematangan (oil window) meliputi batuan induk Formasi Woniwogi, Formasi Aiduna, dan Formasi Modio. Potensi reservoir terdapat di pada Formasi Tipuma (Triasik), Aiduna (Permian), dan Modio Dolomite (Devonian-Silurian). Seal rock berasal dari batuan penutup regional dan intraformasi, berupa batulanau dan serpih yang cukup rapat. Mekanisme perangkap di area ini merupakan kombinasi antara perangkap struktural (antiklin yang dibatasi patahan) dan perangkap stratigrafi (sub-unconformity). Leads yang teridentifikasi meliputi tujuh lead pada Modio Dolomite structural play, enam lead pada Permian Aiduna Sandstone structural play, dan empat lead pada Triassic Tipuma Sandstone structural play.

Kata Kunci: *gravity, seismik, sumur, hidrokarbon, offshore Akimeugah*

INTRODUCTION

Indonesia's petroleum potential is reflected in the presence of 128 identified sedimentary basins (Kementerian Energi dan Sumber Daya Mineral Republik Indonesia – Badan Geologi, 2022), many of which remain insufficiently explored. Updating the national sedimentary basin map through the integration of new data and comprehensive geological and geophysical studies is essential to improve the accuracy of the national hydrocarbon resource inventory. The presence of hydrocarbons in several wells within the Akimeugah Basin, including South Oeta-1, Kola-1, Buaya Besar-1, and ASM-1, indicates an active petroleum system in the region (Tim Evaluasi Data Migas, 2024). Hydrocarbon indications have been found in various types of reservoir rocks; however, no commercial production has been established in the basin to date. To identify new hydrocarbon reserves, the application of appropriate geological concepts is crucial, especially in defining the type of petroleum play, so that exploration strategies can be more focused and effective. One potential petroleum play estimated to hold significant reserves involves Mesozoic and Paleozoic sedimentary rocks originating from the Australian passive margin. A previous study by Bachri (2014) emphasized the importance of these sedimentary rocks, predominantly of Mesozoic age, which serve both as source rocks and reservoir rocks. This aligns with stratigraphic correlations of Mesozoic sedimentary rocks in northern Australia, which have been proven to contain hydrocarbons, as observed in the Bonaparte, Carnarvon, and Canning basins (Struckmeyer et al., 2006).

Stratigraphic traps are also present in the Akimeugah Basin, particularly in its southern part. In addition to the presence of source rocks, reservoir rocks, and seal rocks, the Papuan region also displays anticlinal structures and ramp anticlines (Panggabean & Hakim, 1986), which have great potential as hydrocarbon traps. The primary regional seal in the Akimeugah Basin and across most of Papua consists of thick shale layers from the Piniya Formation. Satyana (2017) stated that the Paleozoic play in the Arafura Sea and southern Papua is one of the most prospective plays, which requires the integration of geological, geophysical, and geochemical analyses to validate and confirm whether the oil generated in this region shares similarities with petroleum systems in Australia. Post

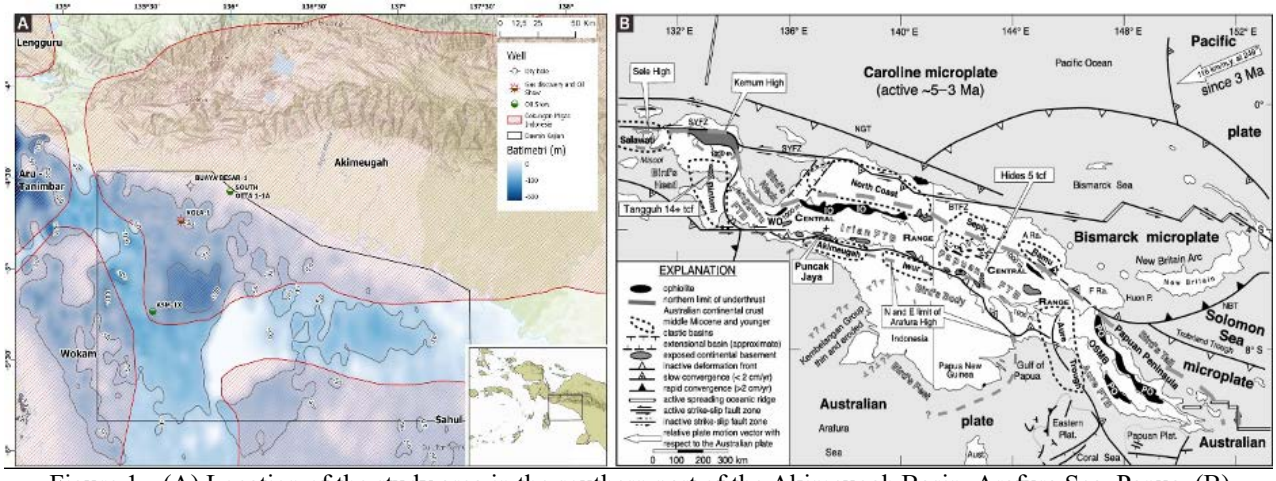

Figure 1. (A) Location of the study area in the southern part of the Akimeugah Basin, Arafura Sea, Papua. (B) Regional tectonics framework of Papua, modified after Sapiie (1998).

mortem drilling analyzes indicate that the failures of four exploration wells in the study area, which are Kola-1, ASM-1X, South Oeta-1, and Buaya Besar-1, were generally caused by structural or stratigraphic traps, seal ineffectiveness, and migration pathway issues (Tim Evaluasi Data Migas, 2024). In the Kola-1, Drill Stem Test (DST) number three (DST#3) was conducted on the Permian Aiduna interval at depths of 12,566 to 12,592 ft measured from the Rotary Kelly Bushing (RKB). The test yielded a flow of 1,825 barrels of water per day (BWPD) and 50 thousand cubic feet per day (MCFPD) of gas. Additionally, oil shows were identified in the Aiduna Formation and Modio Dolomite Formation.

The objective of this study is to analyze and re-evaluate geological and geophysical data, including gravity, seismic, and well data, in order to delineate sub-basins, characterize the petroleum system elements, and identify hydrocarbon potential within the Offshore of Akimeugah Basin in Papua. The study area is located in the southern part of the Akimeugah Basin, specifically in the offshore zone, as illustrated in Figure 1.

Regional Geology

Akimeugah Basin is located in eastern Indonesia, at the convergence of three tectonic plates: the Eurasian continental plate, the Indo-Australian continental plate moving northward, and the Pacific oceanic plate moving westward (Hamilton, 1979). The basin lies along the Australian continental margin and is classified as an intracontinental rift basin (Moore et al., 1996). Numerous studies have examined the tectonic and regional geological aspects of eastern Indonesia and northern Australia, including those by Carter et al. (1976), Bowin et al. (1980), Pigram & Panggabean (1984), Dow & Sukamto (1984), Peck & Soulhol (1986), Pigram & Davies (1987), Audley-Charles (1988), Bradshaw et al. (1988), Daly et al. (1987, 1991), Henage (1993), Struckmeyer et al. (1993), Metcalfe (1996), Hall (1996), Kendrick & Hill (2001), and Davies (2010). The Akimeugah Basin evolved from the Pre-Tertiary to the Tertiary period and is categorized as a foreland basin that has undergone rifting processes (Harahap, 2012). Miharwatiman et al. (2013) identified the basin as part of the broader Arafura Basin located on the Arafura Platform. The development of this basin began during the Proterozoic to Paleozoic era as a failed rift along the northwestern margin of the Australian continent during the Late Proterozoic.

Based on the tectonic history, most of Papua, particularly its southern region where the suture between the Pacific and Australian plates is located, is underlain by Australian continental crust. This includes overlying sediments derived from the northwestern Australian shelf (Bradshaw et al., 1988). These geological characteristics indicate a strong similarity with proven hydrocarbon systems in northern Australia. In Papua, a comparable setting is reflected in the stratigraphic framework of the Bintuni and Salawati basins, which according to Darman and Sidi (2000), contain Mesozoic sedimentary rocks as well as metamorphic Paleozoic rocks that are believed to originate from the Australian crust.

The development of the petroleum system in the Akimeugah basin occurred during the Paleozoic and Mesozoic eras, when the Australian Plate was situated at passive margin (Barber et al., 2003). The collision between the Australian and Pacific plates during the Late Miocene led to basin subsidence followed by rapid sedimentation, resulting in the deposition of thick sedimentary sequences up to 2,750 m in thickness, known as the Buru Formation. The substantial thickness of these sediments exerted significant loading on the older sedimentary rocks, promoting the maturation of hydrocarbons generated during the Paleozoic and Mesozoic. The tectonic evolution of Papua indicates that Australia, Papua, and Papua New Guinea originated from a shared geological domain. Therefore, the hydrocarbon potential identified in both Australia and Papua New Guinea can be correlated with the petroleum prospectivity of the Akimeugah Basin (Pigram & Panggabean, 1984). According to the terminology of the Australian Geological Survey Organization (Struckmeyer et al., 2006), there are three major petroleum systems in the Bonaparte Basin of northern Australia: the Larapintine System, which consists of marine facies source rocks of Early to Middle Paleozoic age (including shale and carbonate); the Gondwanan System, dominated by terrestrial facies source rocks of Permian age; and the Westralian System, composed of marine source rocks of Jurassic age. Based on age correlation, the Larapintine System is comparable to the Pre-Permian sequence in the Akimeugah Basin, the Gondwanan System corresponds to the Tipuma and Aiduna sequences, and the Westralian System aligns with the Kemblengan sequence.

Stratigraphy

The stratigraphy of the study area can be grouped based on depositional sequences (Figure 2). There are three major megasequences that developed along the

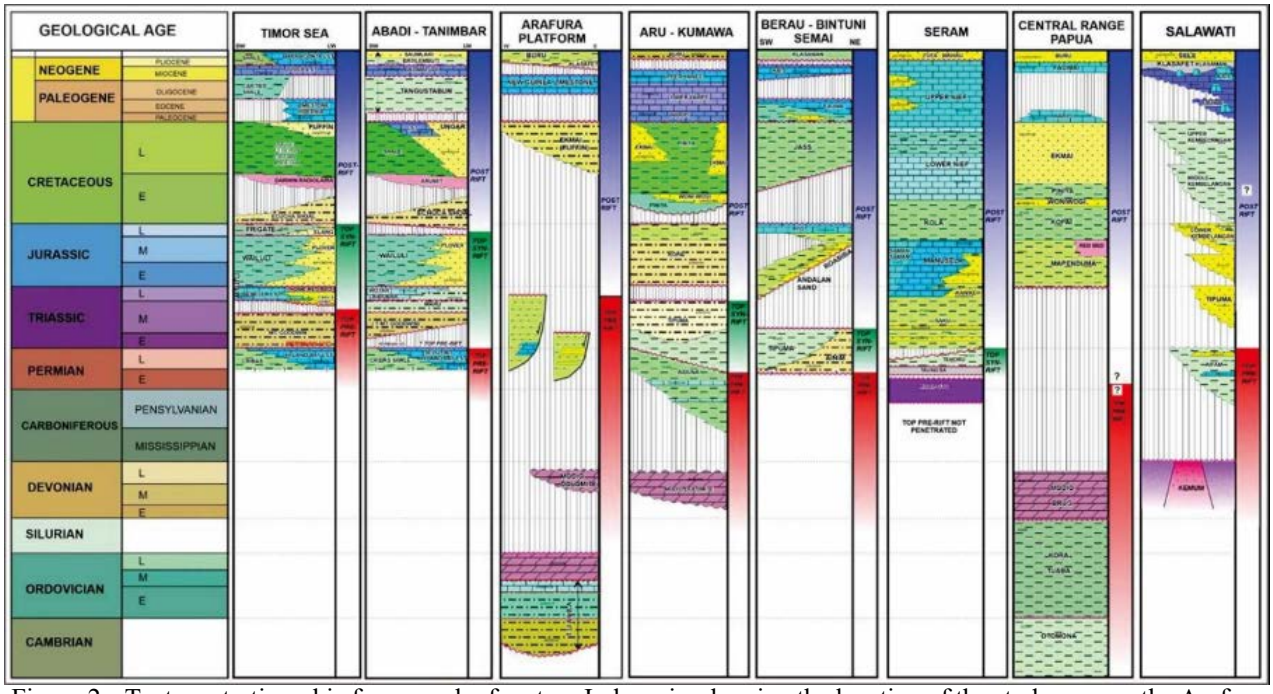

Figure 2. Tectonostratigraphic framework of eastern Indonesia, showing the location of the study area on the Arafura Platform (Siregar et al., 2024).

Australian continental margin in eastern Indonesia (Siregar et al., 2024), namely the pre rift, syn rift, and post rift megasequences. The lowermost unit is the pre rift megasequence, which formed prior to the rifting phase. In Arafura platform, this megasequence consists of the Tuaba Formation which was deposited during the Cambrian-Ordovician period, with an estimated thickness of up to 3,000 meters (Rusmana et al., 1995). The Tuaba Formation comprises quartz sandstone at the base, overlain by reddish siltstone and mudstone. Above this lies the Modio Formation, dated to the Devonian, which is characterized by dark gray dolomite with well-developed thin bedding at the base, transitioning upward into fine clastic rocks consisting of alternating micaceous siltstone and very fine to fine grained sandstone.

The syn rift megasequence includes the Aiduna Formation of Permian age and the Tipuma Formation of Triassic age. The Aiduna Formation consists of interbedded shale and siltstone, with occasional coal layers of lacustrine facies and sandstone interbeds containing shale of fluvial meandering channel facies. Overlying the Aiduna Formation is the Tipuma Formation, which consists of gray, red, and green claystone, sandstone, conglomerate, and minor micritic limestone. The thickness of the Tipuma Formation reaches up to 500 meters (Panggabean & Hakim, 1986).

Above the Tipuma Formation, during the Late Jurassic to Late Cretaceous, the Kemblengan sequence was deposited, marking the onset of the post rift megasequence. This megasequence is bounded by an unconformity of Cretaceous age. In several locations, the Cretaceous unconformity has eroded the Jurassic sequence and the upper parts of the Paleozoic sequences (Miharwatiman et al., 2013). The Kemblengan sequence is subdivided into four formations, from oldest to youngest: Kopai Formation, Woniwogi Formation, Piniya Formation, and Ekmai Formation. During this phase, the Australian Plate was classified as a stable passive margin. This sequence consists of carbonate mudstone and fine sandstone (Kopai), quartz sandstone with interbedded mudstone (Woniwogi), calcareous mudstone, fine sandstone, and nodular limestone (Piniya), as well as sandstone, clastic limestone, and shale (Ekmai). Overlying the Kemblengan Group is the New Guinea Limestone Group of Tertiary age, which is subsequently overlain by the Buru Formation of Plio-Miocene age. The Buru Formation consists of bluish gray mudstone, sandy shale, sandstone, conglomerate, limestone, and coal.

METHODS

This study utilizes subsurface data consisting of well data, 2D seismic data, and gravity data (Figure 3). The gravity dataset is a compilation from several sources, including marine gravity data acquired by

the Marine Geological Institute in 2017, onshore gravity data from the Geological Survey Center database, and regional gravity data from the Arafura offshore survey in the Papua region. Seismic and well data were obtained from the Center for Data and Information Technology (PUSDATIN), Ministry of Energy and Mineral Resources. The seismic dataset includes 47 lines acquired during the 2000 and 2009 surveys. Four exploration wells were used in this study, namely ASM 1X, Kola 1, South Oeta 1, and Buaya Besar 1. Gravity analysis was carried out using spectral analysis and 2D forward modeling to delineate the configuration of the basement, basin boundaries, and depocenters. Well data were used for geochemical analysis of the source rocks to assess their maturity and hydrocarbon generation potential. In addition, petrophysical analysis was conducted to evaluate the physical properties of the reservoir rocks. Seismic data were used to map subsurface structures and characterize the reservoir through seismic inversion and sweetness attribute analysis.

RESULTS

Gravity Analysis

Understanding the configuration of sedimentary basins is crucial, as they represent key depositional environments that facilitate the generation, migration, and entrapment of hydrocarbons within a petroleum system. The results of gravity analysis show the presence of several sub-basins and structural patterns controlled by geological structures within the offshore Akimeugah basin, as shown in Figure 4.

This study successfully distinguishes the basinal pattern in the area and name it as West Kola High, Kola Basin and East Kola High. Kola Basin is likely the most prominent basin at the area, bounded by a ~N-S trending normal fault with a strike-slip component at the west and east. East Kola high shows a characteristic of the stable platform with a ~E-W trending shallow basin at the central. The stratigraphy of this basin cannot finely identified because the lack of well data. But, it can be the new potential basin also at that area. Spectral analysis of gravity data indicates that the depth

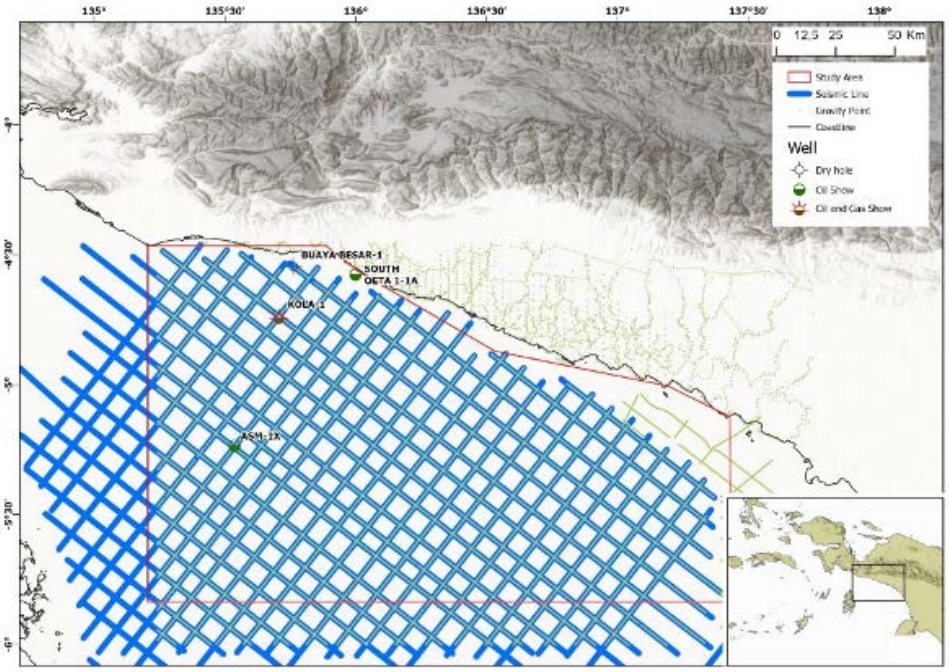

Figure 3. Distribution of wells, seismic lines, and gravity data in the Offshore Akimeugah Basin.

The integration of gravity analysis, source rock geochemical evaluation, petrophysical analysis, seismic attributes and inversion, along with subsurface interpretation, was used to define the basin configuration, identify petroleum system elements, and map hydrocarbon leads of Mesozoic and Paleozoic age in the Offshore Akimeugah Basin.

to basement varies between 2 and 6 km, with an average depth of approximately 3.61 km. These findings are further supported by the results of 2D gravity modeling (Figure 4b).

Well Log Analysis

Well evaluation in this study utilized log data from four wells located in the Offshore Akimeugah Basin: ASM-1X, Kola-1, South Oeta-1, and Buaya Besar-1. Stratigraphic correlation was conducted

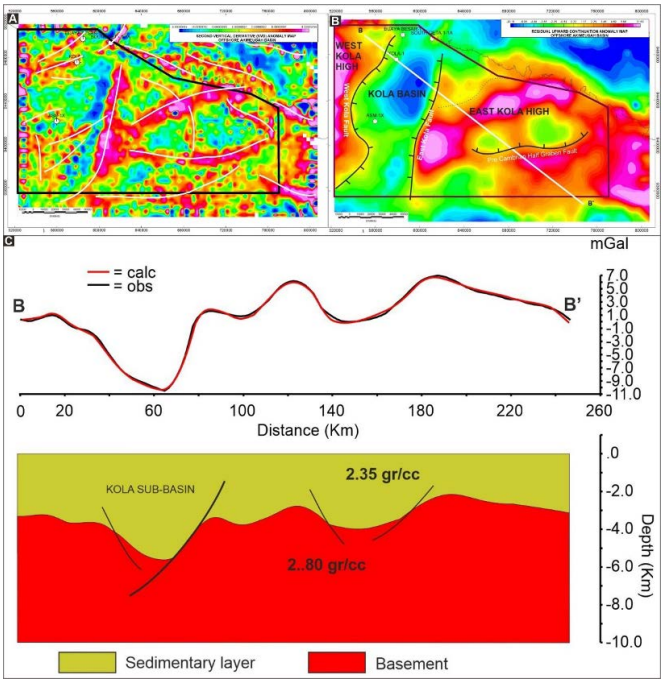

Figure 4. Gravity analysis of the Offshore Akimeugah Basin, Papua. Second Vertical Derivative (SVD) anomaly map (A); Residual anomaly map from upward continuation (B); 2D gravity model along section B–B'(C).

along a south–north cross-section passing through wells ASM-1X, Kola-1, and South Oeta-1 (Figure 5), using the base Cretaceous unconformity horizon as a flattening reference. This unconformity separates two megasequences: the post-rift megasequence above the Cretaceous unconformity, and the syn-rift megasequence below it, ranging from the Late Mesozoic to the Cenozoic. In the ASM-1X, the base Cretaceous unconformity coincides with the top of the Triassic Tipuma Formation. In Kola-1, this

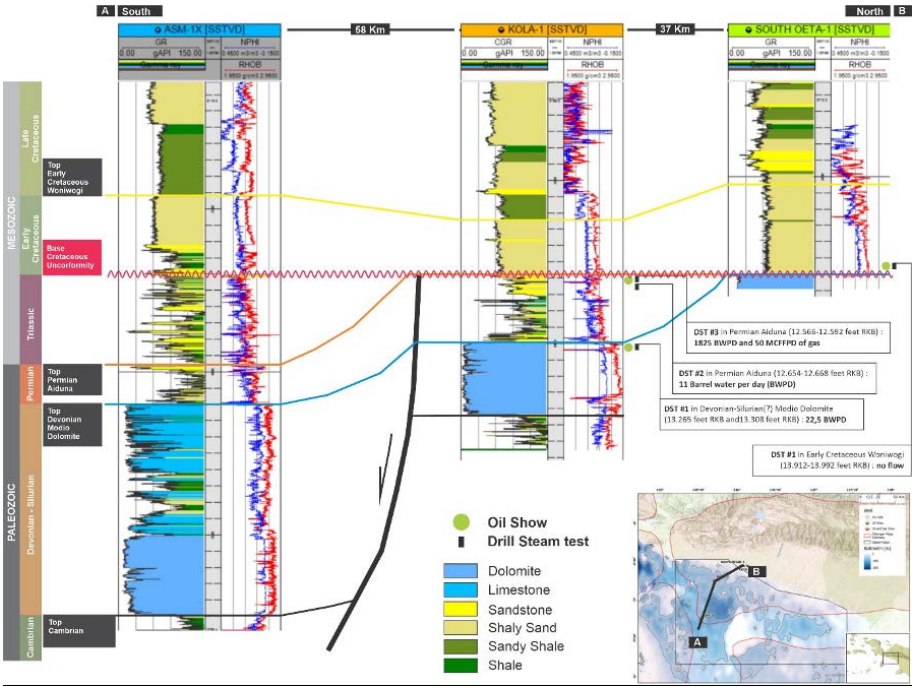

Figure 5. South–north stratigraphic correlation flattened at the base Cretaceous unconformity horizon.

Table 3. Calculated petrophysical parameters from Kola-1 and ASM-1X wells.

WELL	AGE/FORMATION	ZONA	FACIES	PETROPHYSICAL PARAMETER								
				TOP	BOTTOM	GR_MAX	GR_SH	GROSS	NET	NTG	VSH	POR
KOLA-1	Permian Aiduna	KP-1A	Mouth Bar dan Distributary Channel	3829,9	3850	131	42	20,1	9,6	0,48	0,38	0,125
		KP-1B	Mouth Bar dan Distributary Channel	3856,7	3886,3	114	64	29,6	0	0,00	0,4	0,143
		KP-2A	Braided Channel	4007	4032	148	31	25	14	0,56	0,36	0,09-0,188
	Devonian-Silurian Modio Dolomite	KD-1A		4205,6	4224,7	103	4	19,1	3,9	0,20	0,17	0,058-0,27
ASM-1X	Triassic Tipuma	AT-1A	Distributary Channel	2792,3	2813,7	119	58	21,4	18	0,84	0,36	0,145
		AT-2A	Mouth Bar	2874,6	2888,9	110	12	14,3	9,7	0,68	0,15	0,189
		AT-2B	Distributary Channel	2893,4	2920	118	40	26,6	26	0,98	0,36	0,145
		AT-2C	Mouth Bar	2923	2933	103	61	10	9,7	0,97	0,38	0,133
	Permian Aiduna	AP-1A	Braided Channel	3067,8	3093,9	152	46	26,1	20	0,77	0,49	0,08
	Devonian-Silurian Modio Dolomite	AD-1A		3424	3500	112	16	76	14,8	0,19	0,4	0,017

horizon aligns with the top of the Permian Aiduna Formation, while in South Oeta-1, it corresponds to the top of the Devonian–Silurian Modio Dolomite. Based on the correlation section, the Triassic sequence is only developed in the ASM-1X. The Permian sequence is observed in both ASM-1X and Kola-1, whereas in South Oeta-1, the pre-rift megasequence is represented by the Devonian–Silurian Modio Dolomite Formation.

Petrophysical evaluation of wells Kola-1 and ASM-1X is summarized in Table 1. In the Tipuma Formation, analysis from ASM-1X indicates four reservoir zones, with effective porosity values ranging from 0.133 to 0.189 and water saturation between 0.68 and 0.768. Depositional facies within these zones include mouth bars, distributary channels, and braided channels.

The Aiduna Formation, evaluated from both ASM-1X and Kola-1, also reveals four reservoir zones. Zone AP-1A in ASM-1X and zones KP-1A, KP-1B, and KP-2A in Kola-1 exhibit net-to-gross values ranging from 0.048 to 0.56 and effective porosity values between 0.125 and 0.188. Identified facies in this formation include distributary channels and mouth bars.

Meanwhile, the dolomite and limestone of the Modio Formation, interpreted from ASM-1X and Kola-1, reflect a shallow marine depositional environment. These carbonates display an average effective porosity of approximately 0.27 and water saturation of around 0.8. The most favorable reservoir potential is associated with karstified zones formed through diagenetic processes or with intervals showing fractured structures, making them prime targets for hydrocarbon exploration.

Geochemical Analysis

Geochemical analysis was conducted by Maxus Aru Inc on well Kola-1, which reaches a total depth of 14,300 ft (4,358.64 m), penetrating as deep as the Silurian-aged Pre-Modio Formation. The analytical methods employed include Total Organic Carbon/ Rock-Eval Pyrolysis (TOC/REP), vitrinite reflectance, gas chromatography (GC), gas chromatography–mass spectrometry (GC-MS), and carbon isotope analysis.

The TOC vs. PY cross-plot (Figure 6a) indicates that the majority of source rocks in well Kola-1 exhibit gas-generating potential with fair quality. Source rocks from the Aiduna Formation demonstrate fair to excellent gas potential. Several source rock samples with excellent gas-generating potential originate from the Buru, Piniya, Woniwogi, and Aiduna formations. Meanwhile, the Pre-Modio Formation has been identified as an oil-prone source rock but with poor generative quality.

Thermal maturity assessment based on the Tmax vs. Hydrogen Index (HI) cross-plot (Figure 6b) reveals that source rocks from the Woniwogi, Aiduna, Modio, and Pre-Modio formations have reached the oil window. The plot also shows that most source rocks contain Type III kerogen (gas-prone). Two Permian-aged source rock samples (Aiduna Formation) indicate mixed Type II/III kerogen, capable of generating both oil and gas, while one Lower Miocene–Pliocene sample (Buru Formation) contains marine Type II kerogen, indicating oil-prone characteristics.

Furthermore, the vitrinite reflectance (Ro) vs. depth cross-plot (Figure 6c) demonstrates that source rock maturity begins to be reached at around 3,320 m,

particularly in rocks from the Piniya, Woniwogi, Aiduna, Modio, and Pre-Modio formations. Two samples from the Pre-Modio Formation have even attained the wet gas maturity level. Between depths of 3,150 and 2,700 m, Ro values decrease to around 0.3, indicating possible tectonic uplift and erosion. Unconformities are also indicated at intervals of 3,836–3,838 m and 4,175–4,280 m.

The burial and thermal history modeling results for well Kola-1 are presented in Figure 7. Based on the model, the Permian Aiduna source rock began to enter early maturity (Ro = 0.55) during the Early Cretaceous, around 132 Ma. Peak oil maturity (Ro = 0.7) was reached between 119 and 89 Ma, and late oil maturity (Ro = 1) was achieved in the Late Cretaceous, around 85.9 Ma. At present, the early oil window is identified at 3,609 meters depth, peak oil maturity at 3,849 m, and late oil maturity at 4,043 m.

Seismic Interpretation

Seismic interpretation was carried out on several seismic lines available in the Offshore Akimeugah area and its surroundings. The interpretation process involved several stages, including seismic mistie analysis, well-to-seismic tie, horizon and fault interpretation, and the construction of subsurface structural maps. The stratigraphic markers used in the interpretation were derived from well data analysis (Figure 5), and include the following key horizons: Base Cambrian, Modio Dolomite (Devonian), Aiduna Formation (Permian), Unconformity/Lower Triassic Tipuma, Kemblengan Group Woniwogi (Early Cretaceous), Kemblengan Group Piniya-Ekmai (Late Cretaceous), Intra New Guinea Limestone Group (Late Oligocene), Batugamping Nugini (Late Miocene), and Buru Formation (Pliocene).

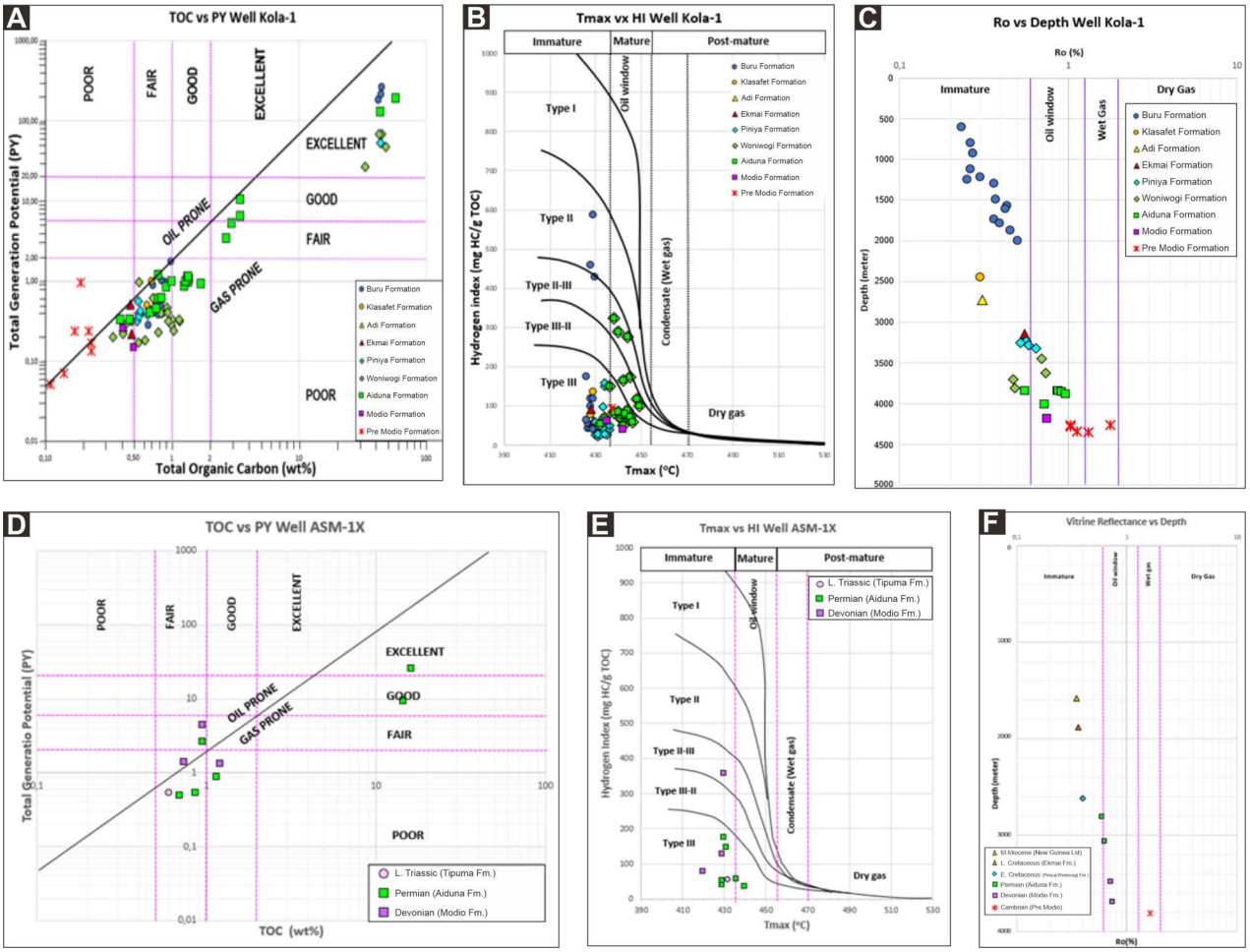

Figure 6. Cross-plot of TOC vs Pyrolysis Yield (PY) for well Kola-1 and ASM-1X (A and D); Cross-plot of Tmax vs HI for Kola-1 and ASM-1X (B and E); Cross-plots of Tmax and vitrinite reflectance (Ro) vs depth in Kola-1 and ASM-1X (C and F).

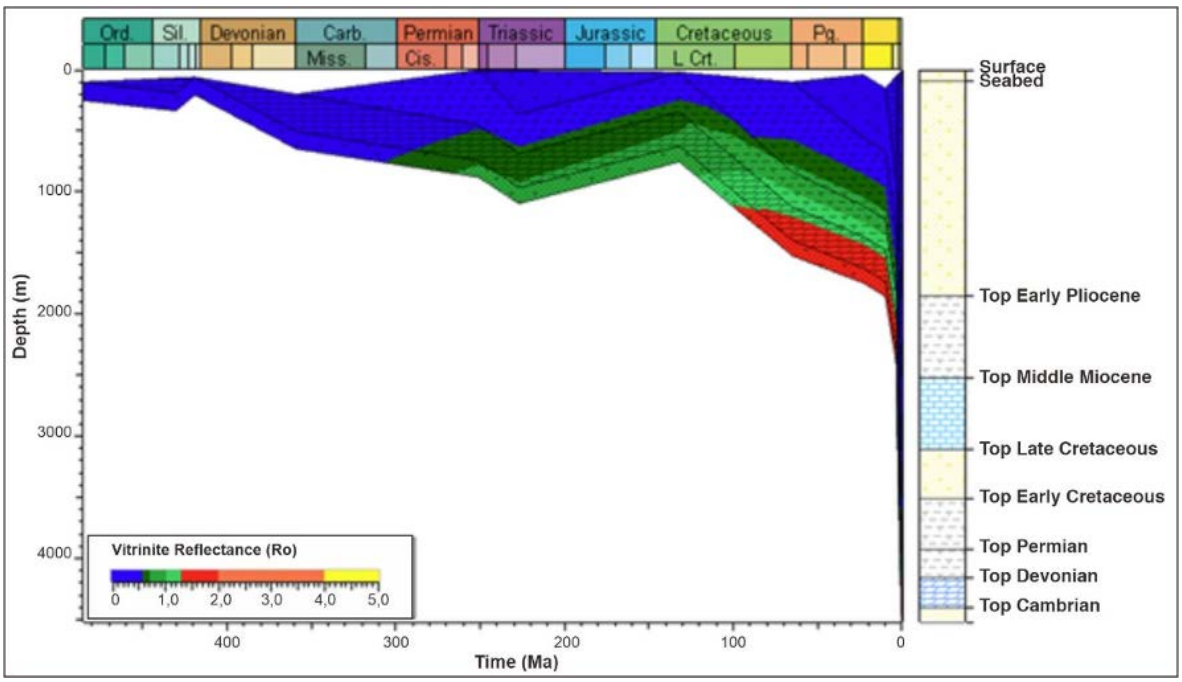

Figure 7. Burial history diagram of Kola-1

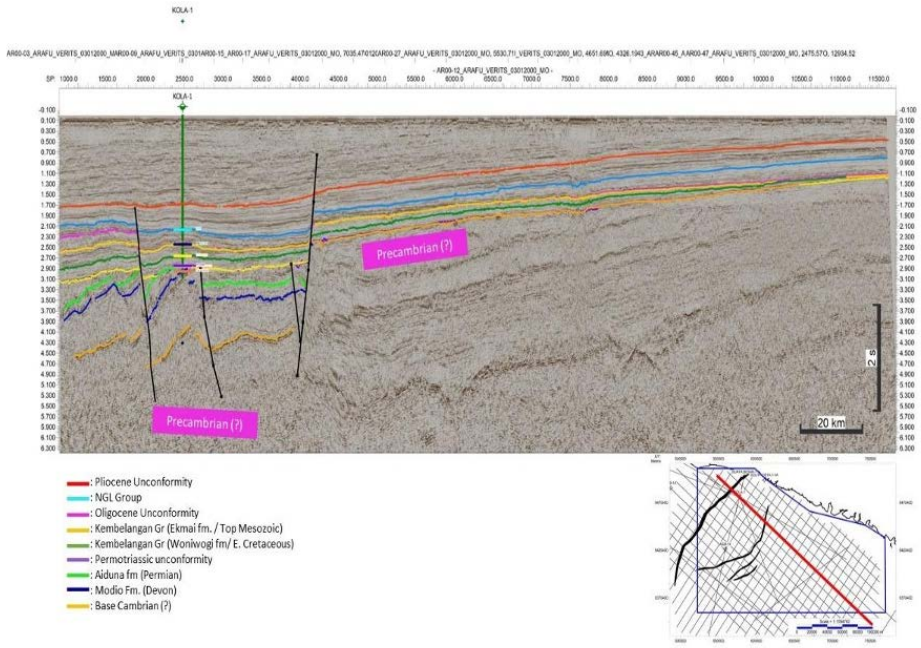

Figure 8. Seismic interpretation of Line AR00-12 crossing the Kola-1. Paleozoic rock units are observed in the western part of the seismic section.

Figure 8 illustrates the internal structures of various stratigraphic intervals. Several types of seismic reflector terminations were identified, including onlap, downlap, and toplap (erosional truncation). These patterns suggest depositional sequences and transgressive surfaces. The Devonian Modio Dolomite exhibits a parallel internal configuration with toplap terminations, indicating deposition in a carbonate platform environment followed by erosion due to tectonic uplift.

The deposition of the Permian Aiduna Formation and the Lower Triassic Tipuma Formation occurred in a continuous sequence, as evidenced by the parallel reflectors and lack of erosional truncation. After the deposition of the Tipuma Formation, a major tectonic event caused folding and partial erosion of the Modio, Aiduna, and Tipuma

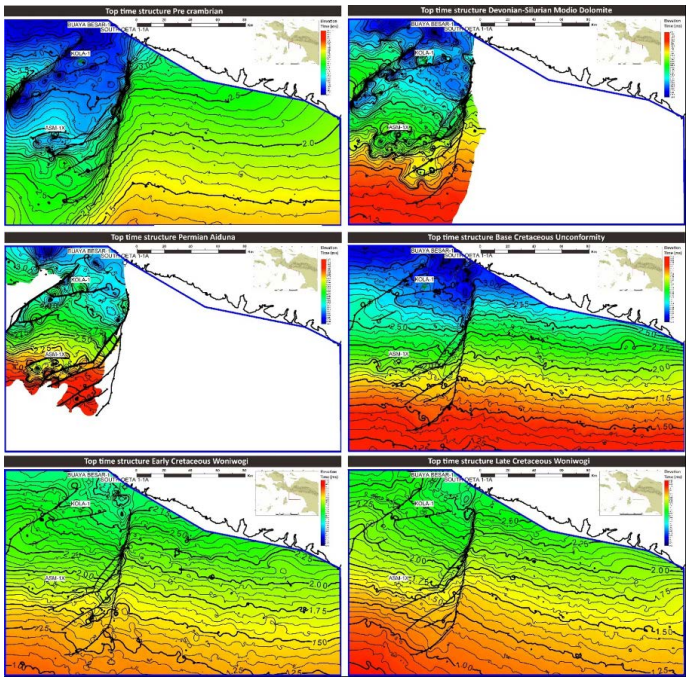

Figure 9. Seismic-derived time structure map of the Offshore Akimeugah Basin.

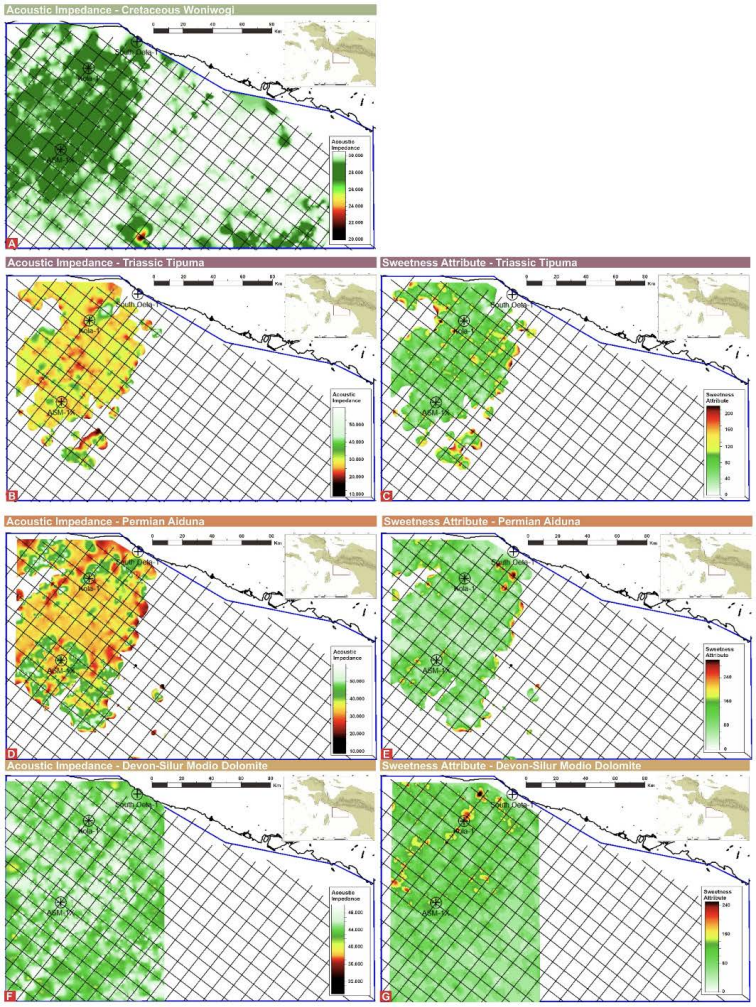

Figure 10. AI and sweetness attribute maps for the Tipuma (B, C), Aiduna (D, E), and Modio Dolomite (F, G) intervals.

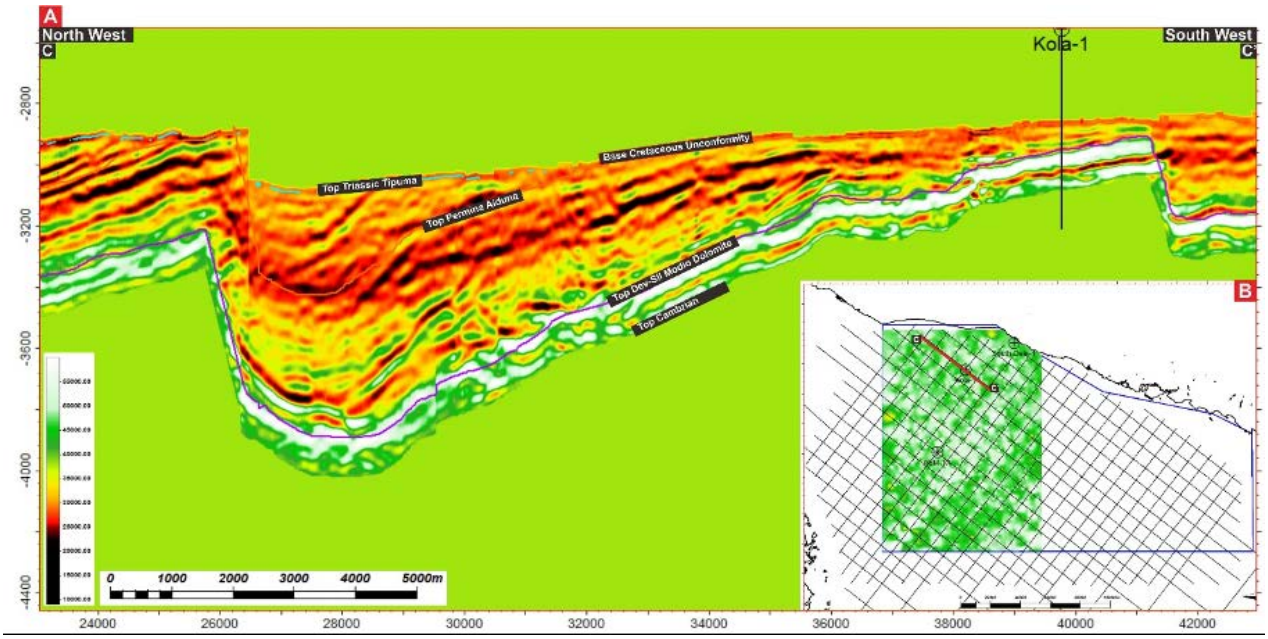

Figure 11. Distribution of low-impedance zones embedded in high-impedance settings (A); AI map of the Modio Dolomite Formation from seismic inversion (B).

Formations. This is reflected in toplap terminations toward overlying Lower Cretaceous sediments, forming a pop-up structure and an unconformity known as the Mesozoic Unconformity. Time-structure maps for key interpreted horizons are presented in Figure 9.

Seismic interpretation reveals that the Cretaceous interval, which unconformably overlies the Paleozoic sequences in the Arafura Basin, has the potential to function as a regional seal. Seismic inversion results for the Late Cretaceous to Jurassic Unconformity interval indicate acoustic impedance (AI) values ranging from 10,000 to 33,000 ft/s*g/cc. The main target within this interval is the Woniwogi shale (Base Cretaceous), characterized by AI values between 29,000 and 30,000 ft/s*g/cc, as indicated by green to white colors in the inversion results (Figure 10a). The AI distribution suggests that Woniwogi shale is primarily concentrated in the eastern and northern parts of the study area.

In the AI distribution maps of the Tipuma and Aiduna Formations (Figures 10b and 10d), potential lead zones are represented by red to dark hues, and are located northwest of Kola-1 and north of ASM-1X. Similar lead patterns are observed in the sweetness attribute maps (Figures 10c and 10e), which largely coincide with the inversion anomalies. Although additional anomalies appear in the southern region in the sweetness attribute map, they are less pronounced than those seen in the AI inversion.

In the Modio Dolomite Formation, seismic inversion results (Figure 11a) show low impedance zones interspersed within high-impedance areas. These high impedance zones may function as internal seals, enabling hydrocarbon entrapment within porous dolomite. The distribution of low impedance zones, mapped within 150 ms below the Top Modio Dolomite, are shown in yellow to brown shades. Sweetness attribute analysis (Figure 11b) reveals similar trends, and black outlines mark inversion derived leads that correlate well with sweetness anomalies. However, in the southern part of the study area, sweetness anomalies appear less distinct (Figure 10g).

DISCUSSIONS

Basin Configuration

Gravity analysis delineates the structural configuration of the Akimeugah Basin (Figure 12), revealing two prominent highs; West Kola High and East Kola High, separated by a north–south trending depocenter known as the Kola Basin. This basin is bounded by two major fault systems; the East Kola Fault to the east and the West Kola Fault to the west. Several exploratory wells (Buaya Besar, South Oeta, Kola-1, and ASM-1X) are located within the Kola Basin, confirming its significance as a key exploration target. A notable feature on the East Kola High is a west–east trending sub-basin, which appears as a half graben on seismic sections, bounded

by north dipping normal faults (Figure 12). The formation of this pre-Cambrian half graben and the Kola Basin reflects distinct tectonic regimes and kinematic histories, requiring further evaluation. Limited well data over the East Kola High poses challenges in fully resolving the tectonic evolution of this sub-basin.

To reconstruct the basin history, palinspastic restoration was performed along regional seismic line B–B′, oriented NW–SE, across the Kola Basin. The restoration indicates that basin development commenced during the pre-Cambrian with the deposition of units Pre-Cambrian-1, Pre-Cambrian-2 and Pre-Cambrian-3 under extensional tectonics,

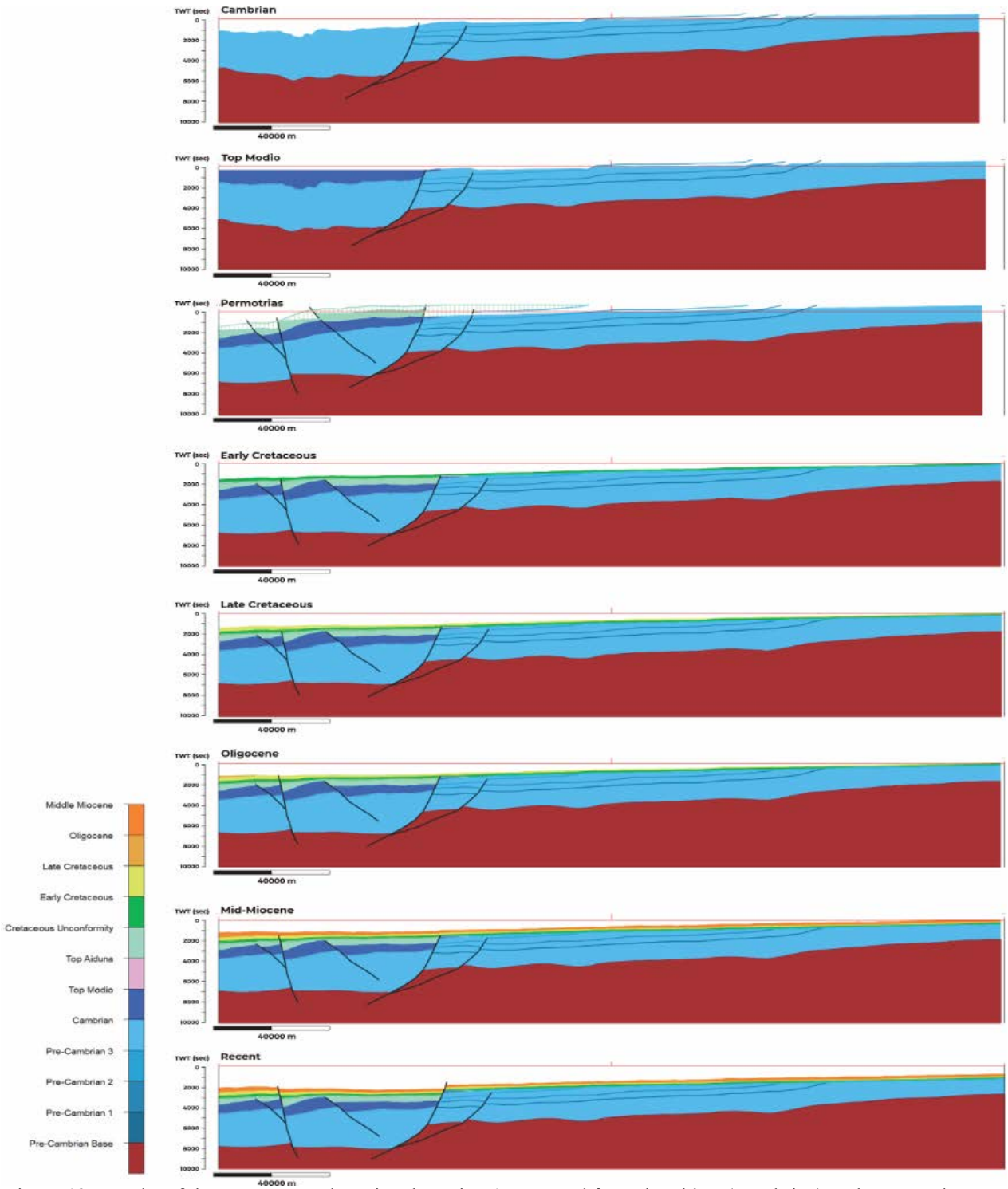

Figure 12. Results of the reconstructed Regional Section 1, arranged from the oldest (Cambrian) at the top to the youngest (Recent) at the bottom. The section line corresponds to B–B′ shown in Figure 4b.

forming normal fault-bounded depressions. Continued extensional activity during the Cambrian resulted in the initiation of the Kola Basin and deposition of the Modio Formation. Sedimentation persisted through the Permo-Triassic until a Permo-Triassic unconformity developed, associated with uplift and erosion.

During the Early Cretaceous, inversion occurred as a consequence of the extensional regime affecting Regional Line B–B′. The resulting accommodation space led to basin sagging, as evidenced by the continued deposition of sedimentary units up to the Recent. This long-term sagging since the Early Cretaceous reactivated pre-existing normal faults within the Kola Basin and its surroundings due to overburden loading. Palinspastic analysis indicates that the Akimeugah Basin has remained generally tectonically stable. No evidence of compression was observed, as typically indicated by negative extension/ shortening values. Strain analysis along regional sections 1 show exclusively positive values, confirming that basin development has been dominated by extension and sagging. These characteristics are typical of an undisturbed passive-margin setting.

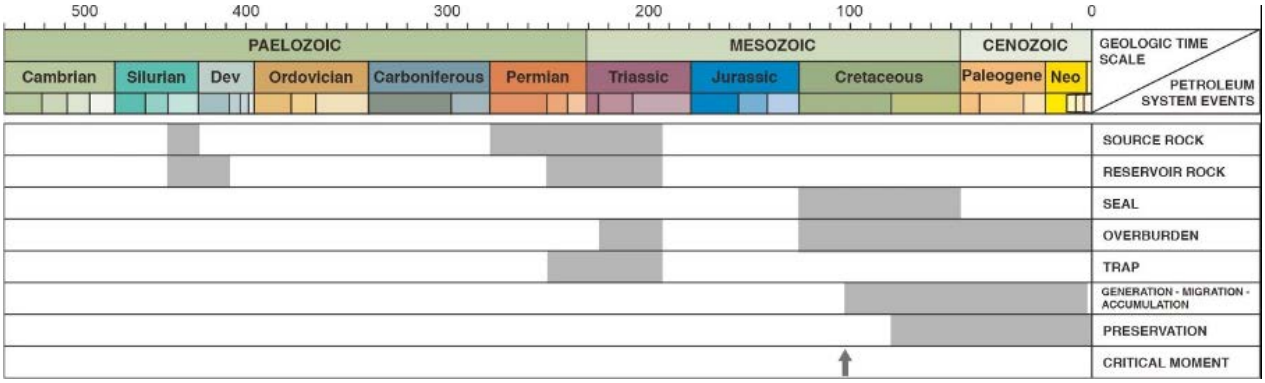

Figure 13. Petroleum system elements and processes in the Offshore Akimeugah Basin.

Petroleum System

The petroleum system of the Offshore Akimeugah Basin is characterized by identified source rocks, reservoirs, seals, and traps, integrated from seismic interpretation, petrophysical analysis, and geochemical evaluation (Figure 13).

Source Rocks

The Aiduna Formation ranges from fair to excellent as a gas-prone source rock. Based on crossplots of Tmax and vitrinite reflectance (Ro) versus depth (Figure 6b and 6c), source rock intervals within the Aiduna Formation in the Kola-1 well enter the oil window at approximately 3,619 m (Tmax) and 3,450 m (Ro). Geochemical analyses including gas chromatography (GC), gas chromatography–mass spectrometry (GC-MS), and carbon isotope studies of samples at 3,843.5 m depth indicate that the organic matter is predominantly of terrestrial origin, deposited under anoxic to suboxic conditions, supporting its potential for gas generation at relatively mature levels.

Based on the similarity of facies and depositional environment between the Aiduna and Tipuma Formations (Figure 5), Tipuma Formation exhibits significant potential as a hydrocarbon source rock, with a predominance of gas-prone characteristics. Organic matter within this formation is primarily Type III kerogen, with minor contributions of Type II kerogen capable of generating both oil and gas The organic input is largely of terrestrial origin, deposited in deltaic to estuarine environments under oxic to suboxic conditions. Source rock quality varies from fair to good, as indicated by total organic carbon (TOC) content and hydrogen index (HI), both of which reflect the hydrocarbon generation potential (Figure 6d, 6e, and 6f).

In terms of thermal maturity, Tipuma Formation is generally capable of reaching gas-mature levels, particularly at intermediate to greater burial depths or in areas with a history of elevated geothermal gradients. This implies that, under suitable burial and thermal conditions, the Tipuma Formation is more likely to enter the gas window rather than the oil window, making it a promising candidate for natural gas exploration. Further geochemical analyses, including Rock-Eval pyrolysis and vitrinite reflectance, are required to confirm hydrocarbon generation capacity within specific areas.

Reservoir Rocks

Reservoir potential in the Offshore Akimeugah area has been identified within three primary

formations: the Triassic Tipuma, the Permian Aiduna, and the Devonian–Silurian Modio Dolomite. Evidence includes oil shows observed in the Kola-1 well, where native hydrocarbons (oil stain and chlorotene cut) were recorded in the upper Permian Aiduna interval (12,581–12,589 ft RKB). Minor oil shows were also reported in the upper Devonian–Silurian(?) Modio Dolomite (13,255–13,270 ft RKB) as dull yellow-brown fluorescence, dark brown staining, and very slow solvent cuts. Drill Stem Test (DST) #3 conducted on the Permian Aiduna (12,566–12,592 ft RKB) yielded 1,825 barrels of water per day (BWPD) accompanied by 48.4–56.6 thousand cubic feet per day (MCF/D) of gas. Chromatographic analysis of the produced gas indicated the presence of methane (C1), ethane (C2), propane (C3), iso-butane (C4), n-butane (C4), pentane (C5), and nitrogen.

In addition to mud log and test data, reservoir potential was further evaluated through facies analysis and petrophysical interpretation (Table 1). The Permian Aiduna and Triassic Tipuma, deposited during the syn-rift phase, are characterized by deltaic reservoir facies dominated by distributary channels and mouth bars, as indicated by log character and moderate porosity values. In the Modio Dolomite, reservoir quality is supported by oil shows, petrophysical analysis, and seismic inversion, which reveal low-impedance zones in the lower part of the formation associated with enhanced porosity, possible fracture development, and karstification due to diagenetic processes. These features collectively identify the Modio Dolomite as a key exploration target within the regional petroleum system.

Seal Rocks

Seal effectiveness in the study area is attributed to both regional and intraformational seals. The regional seal in the offshore Akimeugah Basin is identified as the Cretaceous Klembengan Group (Woniwogi, Piniya, and Ekmai formations), supported by seismic inversion results showing high impedance values. Additionally, tight limestone and dolomite layers act as effective intraformational seals. The Arafura Platform is entirely overlain by Cretaceous and Tertiary sequences that unconformably overlie the Palaeozoic. Well data from Kola-1 and ASM-1 indicate that the lowermost part of the Cretaceous consists predominantly of tight siltstones and shales, further enhancing the sealing effectiveness.

Traps

Tectonic events during the Middle Jurassic induced extensive faulting, folding, and erosional truncation affecting pre-existing units, including the Modio Dolomite, Aiduna, and Tipuma formations. Hydrocarbon trapping mechanisms in this area are a combination of structural traps, mainly fault-bounded anticlines, and stratigraphic traps associated with sub-unconformities.

Play Concept

Petroleum plays identified in the offshore Akimeugah Basin, based on seismic interpretation, petrophysical evaluation, and geochemical analysis, include the Devonian Modio Dolomite stratigraphic–structural play, the Permian Aiduna Sandstone structural play, and the Triassic Tipuma Sandstone structural play. A schematic overview of the petroleum play concepts in the Offshore Akimeugah Basin is shown in Figure 14.

Modio Dolomite stratigraphic–structural play

The Devonian Modio Dolomite serves as the primary reservoir, structurally associated with southwest–southeast trending faults. Source rocks are inferred to originate from Cambrian intervals and shales of the Aiduna Formation. Seismic attribute analysis reveals high impedance zones, suggesting the presence of internal seals within the Modio Dolomite, enhancing hydrocarbon entrapment potential.

Permian Aiduna Sandstone structural play

This play involves Permian Aiduna sandstones as the reservoir, associated with southwest–southeast trending fault systems. Source rocks are likely Cambrian intervals and Aiduna shales. Seismic inversion indicates that the overlying Woniwogi Formation provides an effective top seal, allowing for hydrocarbon retention in the Aiduna reservoir.

Triassic Tipuma Sandstone structural play

The Triassic Tipuma Sandstone, similarly associated with major southwest–southeast trending faults, serves as the reservoir. Potential source rocks include Cambrian intervals and shales of both the Aiduna and Tipuma formations.

Lead Potential

Lead identification and petroleum system play mapping are supported by seismic sweetness attribute analysis and seismic inversion of the

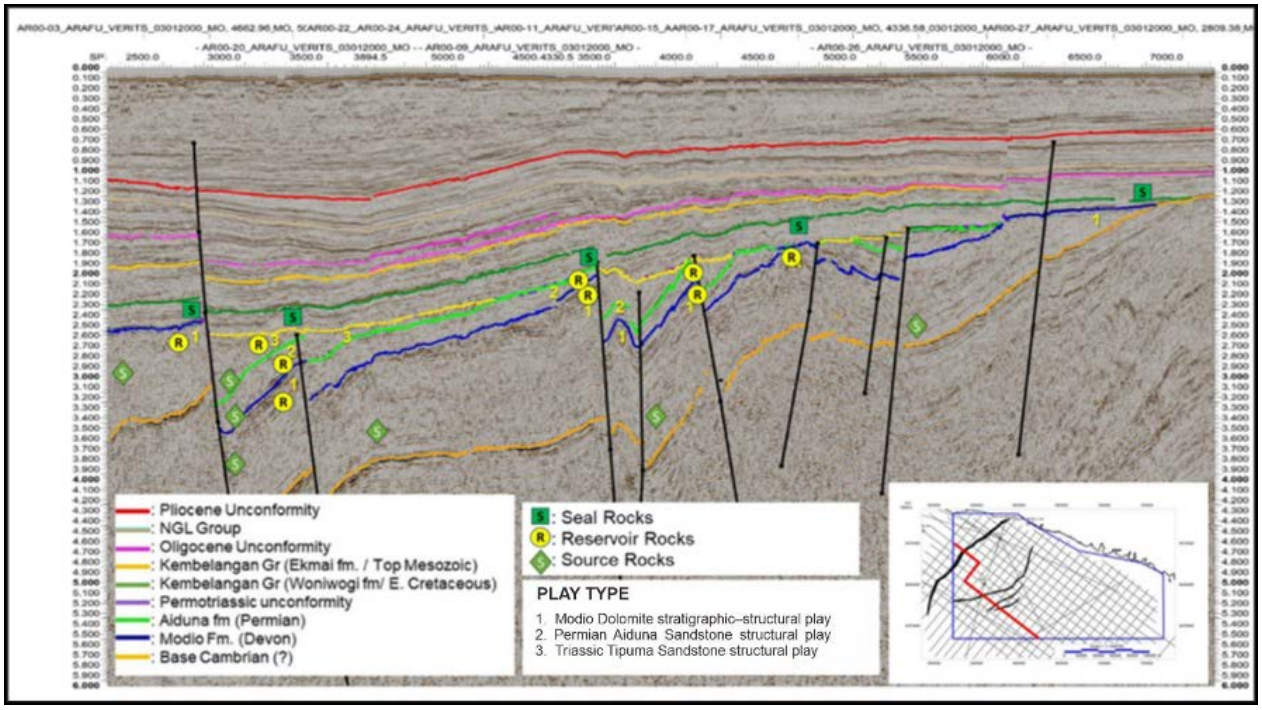

Figure 14. Petroleum play concept in the Offshore Akimeugah area.

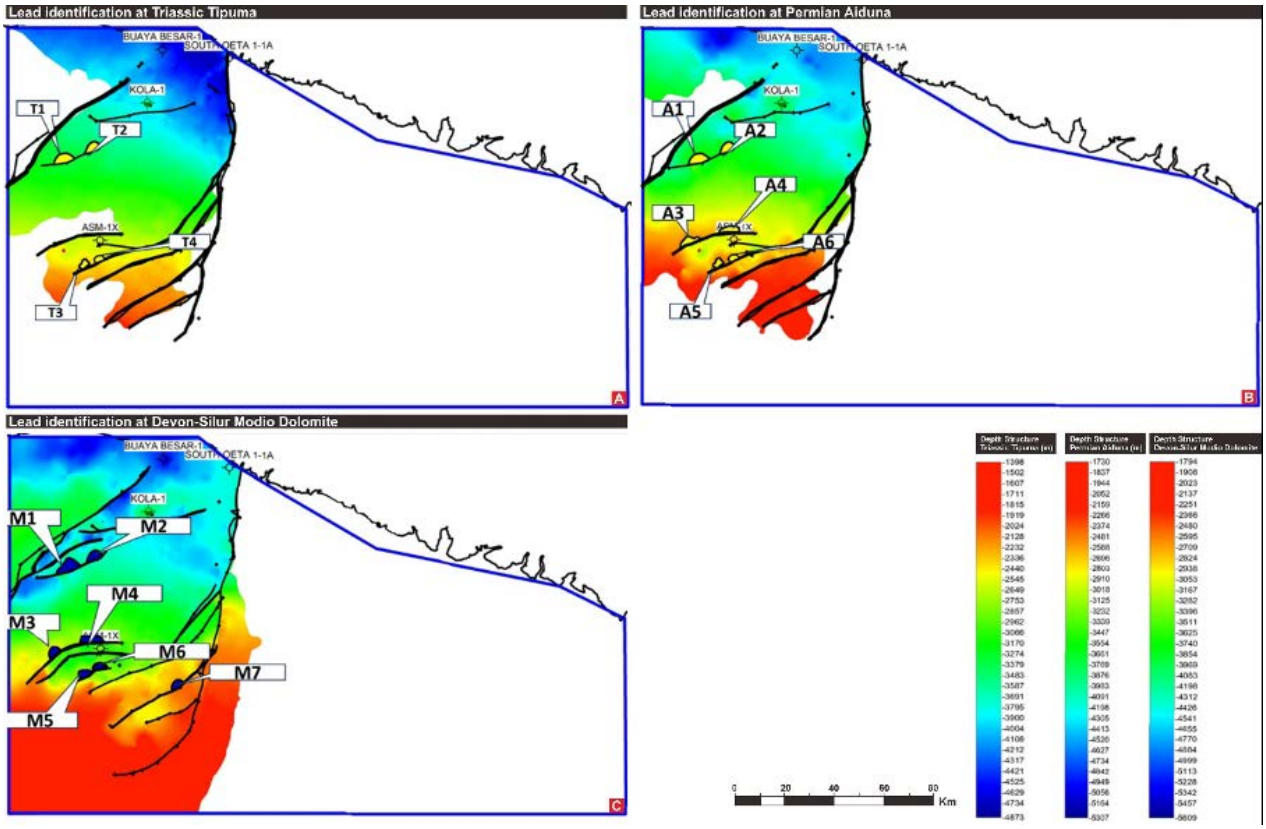

Figure 15. Lead identification in the Offshore Akimeugah Basin

Tipuma, Aiduna, and Modio Dolomite formations. The integration of seismic interpretation with sweetness attribute and inversion results enabled the delineation of potential leads in the Offshore Akimeugah area. A total of four leads are identified in the Triassic Tipuma Sandstone structural play (Figure 15a), six leads in the Permian Aiduna Sandstone structural play (Figure 15b), and seven leads in the Modio Dolomite structural play (Figure 15c).

CONCLUSIONS

Based on gravity data analysis, a total of five sedimentary sub-basins have been delineated in the study area. The underlying basement rocks consist of metamorphosed Australian continental crust with an estimated density of approximately 2.8 gr/cc. Gravity modeling results indicate that the basement depth ranges from 2 to 6 km, with an average depth of about 3.61 km. Source rocks identified in several wells within the study area are dominated by Type III (gas-prone) kerogen, with some intervals containing Type II (oil/gas-prone) kerogen. Mature source rocks within the oil window include the Woniwogi, Aiduna, Modio, and Pre-Modio formations. Reservoir potential, as indicated by petrophysical and seismic inversion analyses, resides in the Triassic Tipuma Sandstone, Permian Aiduna Sandstone, and fractured Devonian–Silurian Modio Dolomite. Sealing effectiveness in the area is provided by both regional and intraformational seals. The Lower Cretaceous section in the Kola-1 and ASM-1 wells consists of tight siltstone and shale, while the widespread Woniwogi shale is interpreted as the primary regional seal. Hydrocarbon trapping mechanisms comprise a combination of fault-bounded structural anticlines and stratigraphic sub-unconformity traps. Identified petroleum plays in the Offshore Akimeugah area include the Modio Dolomite stratigraphic–structural play, Permian Aiduna Sandstone structural play, and Triassic Tipuma Sandstone structural play. A total of seven leads have been delineated in the Modio Dolomite, six in the Aiduna Sandstone, and four in the Tipuma Sandstone.

ACKNOWLEDGEMENTS

We would like to thank the Center for Data and Information of the Ministry of Energy and Mineral Resources (KESDM) for granting data access and the Marine Geological Survey and Mapping Center for facilities and technical support. Special thanks go to the Marine Geological Resources Working Group and our fellow geologists and geophysicists for their constructive input and collaboration during this study.

REFERENCES

Audley-Charles, M. G., 1988. Evolution of the southern margin of Tethys (North Australian region) from Early Permian to Late Cretaceous. *Geological Society, London, Special Publications,* 37(1): 79-100. https://doi.org/10.1144/GSL.SP.1988.037.01.06

Bachri, S., 2014. Kontrol tektonik dan struktur geologi terhadap keterdapatan hidrokarbon di daerah Papua. *Jurnal Geologi dan Sumber Daya Mineral,* 15(3): 133–141.

Barber, P., Carter, P., Fraser, T., Baillie, P., & Myers, K., 2003. Paleozoic and Mesozoic petroleum systems in the Timor and Arafura Seas, Eastern Indonesia. *In*: *Proceedings of the Indonesian Petroleum Association, 29th Annual Convention*. Indonesian Petroleum Association: 1–16.

Bowin, C., Purdy, G. M., Johnston, C., Shor, G., Lawver, L., Hartono, H. M. S., & Jezek, P., 1980. Arc-continent collision in Banda Sea region. *AAPG Bulletin,* 64(6): 868–915. https://doi.org/10.1306/2F91886D-16CE-11D7-8645000102C1865D

Bradshaw, M. T., Yeates, A. N., Beynon, R. M., Brakel, A. T., Langford, R. P., Totterdell, J. M., & Yeung, M., 1988. Palaeogeographic evolution of the North West Shelf region. In P. G. Purcell & R. R. Purcell (Eds.), *The North West Shelf, Australia: Proceedings of the Petroleum Exploration Society of Australia Symposium*. Petroleum Exploration Society of Australia: 29–54.

Carter, D. J., Audley-Charles, M. G., & Barber, A. J., 1976. Stratigraphical analysis of island arc-continental margin collision in Eastern Indonesia. *Journal of the Geological Society,* 132(2): 179–198.

Daly, M. C., Hooper, G. G. D., & Smith, D. G., 1987. Tertiary plate tectonics and basin evolution in Indonesia. *In*: *Proceedings of the 16th Annual Convention of the Indonesian Petroleum Association*. Indonesian Petroleum Association: 400–425.

Daly, M. C., Cooper, M. A., & Wilson, I. (1991). Cenozoic plate tectonics and basin evolution in Indonesia. *Marine and Petroleum Geology,* 8(1): 2–21.

Darman, H., & Sidi, F. H., 2000. *An outline of the geology of Indonesia*. Indonesian Association of Geologists.

Davies, H. L., 2010. Shallow-dipping subduction beneath New Guinea and the geologic setting of the Grasberg, Ok Tedi, Frieda River and Porgera mineral deposits. *In: Abstracts, Australian Earth Sciences Convention*. Geological Society of Australia.

Dow, D. B., & Sukamto, R., 1984. Western Papua: The end product of oblique plate convergence in the Late Tertiary. *Tectonophysics,* 106(1–2): 109–139.

Hall, R., 1996. Reconstructing Cenozoic SE Asia. In R. Hall & D. Blundell (Eds.), *Tectonic evolution of Southeast Asia.* Geological Society, Special Publication, 106: 153–184.

Hamilton, W., 1979. *Tectonics of the Indonesian region* (US Geological Survey Professional Paper 1078). United States Geological Survey.

Harahap, B. H., 2012. Tectonostratigraphy of the southern part of Papua and Arafura Sea, Eastern Indonesia. *Indonesian Journal of Geology,* 7(3): 167–187.

Henage, L. F., 1993. Mesozoic and Tertiary tectonics of Papua: Evidence for non-rotation of Kepala Burung. *In*: *Proceedings of the 22nd Annual Convention of the Indonesian Petroleum Association*. Indonesian Petroleum Association: 763–792.

Kendrick, R. D., & Hill, K. C., 2001. Hydrocarbon play concepts for the Irian Jaya Fold Belt. In *Proceedings of the 28th Annual Convention of the Indonesian Petroleum Association*. Indonesian Petroleum Association: 353–367.

Kementerian Energi dan Sumber Daya Mineral Republik Indonesia – Badan Geologi, 2022. *Peta cekungan sedimen Indonesia 2022*. Kementerian ESDM.

Metcalfe, I., 1996. Pre-Cretaceous evolution of SE Asian terranes. In R. Hall & D. Blundell (Eds.), *Tectonic evolution of Southeast Asia*. Geological Society, Special Publication, 106: 97-122.

Miharwatiman, J. S., Kleibacker, D. W., Backer, J. A., Andria, L., & Elliot, J., 2013. Exploration of the Arafura Basin, Indonesia. *In*: *Proceedings of the 37th Annual Convention and Exhibition of the Indonesian Petroleum Association* (IPA13-G-184). Indonesian Petroleum Association.

Moore, A., Bradshaw, J., & Edwards, D., 1996. Geohistory modelling of hydrocarbon migration and trap formation in Arafura Sea. *PESA Journal, 24*: 35–51.

Panggabean, H., & Hakim, A. S., 1986. Reservoir rock potential of the Paleozoic–Mesozoic sandstone of the southern flank of the Central Range, Irian Jaya. *In*: *Proceedings of the 15th Annual Convention of the Indonesian Petroleum Association*. Indonesian Petroleum Association, 1: 461–481.

Peck, J. M., & Soulhol, B., 1986. Pre-Tertiary tensional periods and their effects on the petroleum potential of Eastern Indonesia. *In*: *Proceedings of the 15th Annual Convention of the Indonesian Petroleum Association*. Indonesian Petroleum Association: 341–369.

Pigram, C. J., & Panggabean, H., 1984. Rifting of the northern margin of the Australian continent and the origin of some microcontinents in Eastern Indonesia. *Tectonophysics,* 107(3–4), 331–353.

Pigram, C. J., & Davies, H. L., 1987. Terranes and the accretion history of the New Guinea Orogen. *BMR Journal of Australian Geology and Geophysics,* 10: 193–211.

Rusmana, E., Parris, K., Sukanta, U., & Samodra, H., 1995. *Geological map of the Timika Quadrangle, Irian Jaya*. Geological Research and Development Center.

Sapiie, B., 1998. Strike-slip faulting, breccia formation and porphyry Cu–Au mineralization in the Gunung Bijih (Ertsberg) mining district, Irian Jaya, Indonesia (Doctoral dissertation). University of Texas at Austin.

Satyana, A. H., 2017. Future petroleum play types of Indonesia: Regional overview. *In*: *Proceedings of the 41st Annual Convention and Exhibition of the Indonesian Petroleum Association*. Indonesian Petroleum Association.

Siregar, P. H., Panggabean, H., & Sebayang, D. A., 2024. New understanding of the Mesozoic tectonostratigraphy of Eastern Indonesia. *Berita Sedimentologi,* 50(1). https://doi.org/10.51835/bsed.2024.50.1.459

Struckmeyer, H. I. M., Yeung, M., & Pigram, C. J., 1993. Mesozoic to Cainozoic plate tectonic and palaeogeographic evolution of the New Guinea region. *In*: *Proceedings of the 2nd PNG Petroleum Convention*. PNG Petroleum Convention: 261–290.

Struckmeyer, H. I. M., Earl, K. L., & Totterdell, J. M., 2006. *Petroleum geology of the Arafura and Money Shoal Basins* (Geoscience Australia Record 2006/22). Geoscience Australia.

Tim Evaluasi Data Migas, 2024. *Laporan kegiatan evaluasi data geologi dan geofisika (G&G) Cekungan Offshore Akimeugah, Papua*. Balai Besar Survei dan Pemetaan Geologi Kelautan. Unpublished.

ACOUSTIC FACIES AROUND THE INTRUSIVE COMPLEX OF SALAHNAMA AND PANDANG ISLANDS, MALACCA STRAIT

AKUSTIK FASIES DI SEKITAR KOMPLEKS INTRUSI PULAU SALAHNAMA DAN PULAU PANDANG, SELAT MALAKA

Subarsyah[1*], Ali Albab[1], Shaska R. Zulivandama[1], Eko Saputro[1], Arif Ali[1], Imam Setiadi[1], Muhammad Zulfikar[1], Faris Nauval Rasyid[1], Riza Rahardiawan[1]

[1] Marine Geological Institute, Indonesia

*Corresponding author:

(Received 16 April 2025; in revised from 17 April 2025; accepted 29 December 2025)

DOI : 10.32693/bomg.40.2.2025.938

ABSTRACT: Salahnama and Pandang Islands lie on the main range of the granite province; both islands are located in the Sunda Shelf, Malacca Straits. These islands are composed of intrusive rocks from Berhala. The rock's existence will offer a significant contribution to the distribution of surface sediments in the surroundings. The sea dynamics and the geometry of the Malacca Strait will also have an impact on the seabed. Apart from that, global factors such as sea level changes will lead to transformation of the depositional environment and subsurface geology in the strait. Geological conditions of the seabed surface and subsurface can be understood and interpreted based on the acoustic characteristics and reflector patterns of a seismic section. Then, based on the acoustic character and reflector pattern, an acoustic facies can be defined. Seismic data measurements have been carried out around Salahnama and Pandang Islands in 2024. Based on the results of the seismic section, the acoustic facies in the study area are classified into 6 (six), which include AF I – AF VI. Seabed morphological features in the form of sand dunes were identified in the first acoustic facies (AF I); this feature is formed due to geometric aspects, surface currents, and bottom current's which may or may not be triggered by tidal vortices. Acoustic Facies II (AF II) is characterized by sandwave or ripple marks formed by strong seabed currents. AF III was formed after the Last Glacial Maximum (LGM) ended and the depositional environment returned to a shallow marine environment, characterized by a transparent pattern in the seismic section. The erosional truncation at the upper boundary of AF IV indicates a change in the depositional environment from shallow marine to coastal or terrestrial environments during the Last Glacial Maximum period. AF V is acoustic bedrock, and AF VI is characterized by a chaotic pattern, which is interpreted as granitic intrusive rocks.

Keywords: Berhala, Facies, Acoustic, Salahnama and Pandang

ABSTRAK: *Pulau Salahnama dan Pandang terletak pada jalur utama granit, kedua pulau berlokasi di Paparan Sunda, Selat Malaka. Kedua pulau ini tersusun atas batuan intrusif Berhala, keberadaan pulau-pulau ini akan memberikan kontribusi yang signifikan terhadap sebaran sedimen permukaan di sekitarnya. Dinamika laut dan geometri Selat Malaka juga akan memberikan pengaruh terhadap kondisi geologi dasar laut, selain itu faktor global berupa perubahan muka air laut akan memberikan perubahan terhadap lingkungan pengendapan dan geologi bawah permukaan di Selat Malaka. Kondisi geologi permukaan dasar laut dan bawah permukaan dasar laut saat ini dapat dipahami dan diinterpretasikan berdasarkan karakter akustik dan pola reflektornya dari suatu penampang seismik. Kemudian berdasarakan karakter akustik dan pola reflektor dapat didefinisikan suatu akustik fasies. Pengukuran data seismik telah*

dilakukan di sekitar Pulau Salahnama dan Pandang pada tahun 2024. Berdasarkan penampang seismik yang dihasilkan, akustik fasies di area studi diklasifikasikan menjadi 6 (enam) yang meliputi; AF I – AF VI. Fitur morfologi dasar laut berupa gumuk pasir teridentifikasi pada akustik fasies pertama (AF I), fitur ini terbentuk akibat aspek geometri, arus permukaan dan arus bawah permukaan yang mungkin terpicu tidal vortis ataupun tidak. Akustik Fasies II (AF II) dicirikan dengan sandwave atau ripple mark yang terbentuk akibat arus dasar laut yang kuat. AF III terbentuk setelah Last Glacial Maximum (LGM) berakhir dan lingkungan pengendapan kembali menjadi lingkungan laut dangkal, dalam penampang seismik dicirikan dengan pola transparan. Ketidakselarasan berupa erosional truncation pada batas atas AF IV merupakan indikasi dari perubahan lingkungan pengendapan dari laut dangkal menjadi lingkungan Pantai atau terrestrial selama perioda Last Glacial Maximum. AF V merupakan batuan dasar akustik dan AF VI dicirikan dengan pola chaotic yang diinterpretasikan sebagai batuan intrusi granitic.

Kata Kunci: *Berhala, Fasies, Akustik, Salahnama dan Pandang*

INTRODUCTION

Salahnama and Pandang Islands are situated in the Sunda Shelf which is part of the relatively stable core 'Sundaland', (Gorsel, 2018). On the Sunda Shelf two significant geological events contribute to the formation of acoustic facies around the intrusive complex of these two islands, in addition the impact of recent ocean dynamics; such as currents, tides and waves.

The present geology of the region is characterized mainly by a granitic belt. These Southeast Asian granitic intrusions are classified into four provinces; the Eastern Province, Main Range Province, Western Province, and the Volcanic Arc Suite (McCourt et al., 1996; Cobbing, 2005). The Eastern Province was initiated by subduction of the Palaeo-Tethys beneath the Cathay Islands which is a composite of the South China, North China, Indochina, West Sumatra, and West Burma plates. The Main Range Province is influenced by the collision of the Sibumasu and the East Malaya-Indochina plates, in contrast the Western Province is related to subduction Ceno Tethys (Metcalfe, I., 2013). The Final province, which is geographically restricted to the Barisan Mountains, exhibits a wide range of composition, (Cobbing, 2005). Salahnama and Pandang Islands are assumed to be located within the granite formations of the Main Range Province (Figure 1).

In the geological maps published by the Indonesian Center of Geological Survey (Bennette, et. al 1981), these two islands are constructed by intrusive rocks from the Berhala Region. The age of the Berhala intrusion is estimated to be Middle Permian. Cobbing (2005) suggested that the Main Range Province granite may have formed 247 to 143 million years ago, or between the Jurassic and Triassic periods. Therefore, the Berhala intrusion may be younger than previously thought.

Sea level changes during the Last Glacial significantly impacted to formation of acoustic facies around these intrusive complexes, The Sunda Shelf was fully exposed and connecting mainland Southeast Asia with Sumatra, Java and Borneo, (Bird, et. all, 2005, Figure 2). During the Last Glacial, Sundaland experienced erosion and a terrestrial environment.

Identifying acoustic facies is a valuable approach for understanding recent geological conditions, as well as the geological processes and sea dynamics that impact the current state of the seabed. In this publication we will examine various acoustic facies around the intrusive complexes of Salahnama and Pandang Islands to gain insights into recent geological conditions and the processes involved.

The geological fact that channels formed during the Last Glacial Period in this region is fascinating, considering that the presence of channels is often associated with the potential for placer minerals. One of the important acoustic facies that can be used to analyze the potential of mineral placers is the acoustic facies within a channel. It would be very valuable to be able to analyze the acoustic facies character within the channel to identify the potential for placer minerals

Study Area

The study area is situated on the waters of the of Salahnama and Pandang Islands, within the narrow and shallow part of the Malacca Straits. It covers approximately 168 km2 and is defined by the coordinates Longitude 99^{o} 37.5' E to - 99^{o} 47.5' E and Latitude 3^{o} 29' N - to 3^{o} 19' N (see Figure 3).

METHODS

The analysis and identification of acoustic facies were primarily conducted on single channel seismic data, complemented with seabed surface samples. A total of 353 km of survey lines were analyzed, consisting of 285 km, including 23 northeast-southwest lines spaced at 0.5 and 1.0 km, and 68 km of 5 northwest-southeast lines, spaced at 2 to 3 km. Ninety grab samples were collected for this study, as illustrated in Figure 4. These data were obtained from a marine mapping project conducted by Marine Geological Institute of Indonesia. The boomer seismic energy of a 300 joules was generated by an Applied Acoustic Boomer System, which was fired at a fixed spacing of 20 m and recorded at a sweep duration of 250 milliseconds.

The analysis and interpretation of seismic dataset were carried out by the using SonarWiz7 software. The seismic profile was converted from two ways time to depth using an acoustic speed assumption of 1600 m/s. The identification of acoustic facies was defined based on their internal and external reflector configuration/geometry, reflection strength, penetration depth and lateral continuity and were then classified into several categories. The analysis of this data focused on identification of granitic rock on seismic profile.

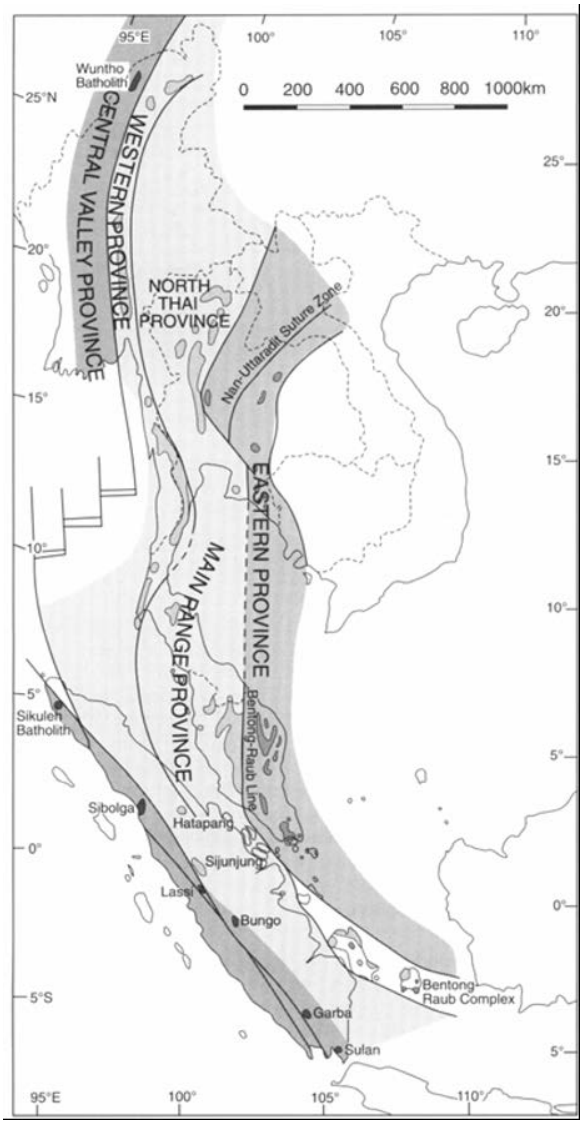

Figure 1. Granitic provinces of Sumatra and adjacent areas (modified after Cobbing et al. 1992 and McCourt et al. 1996).

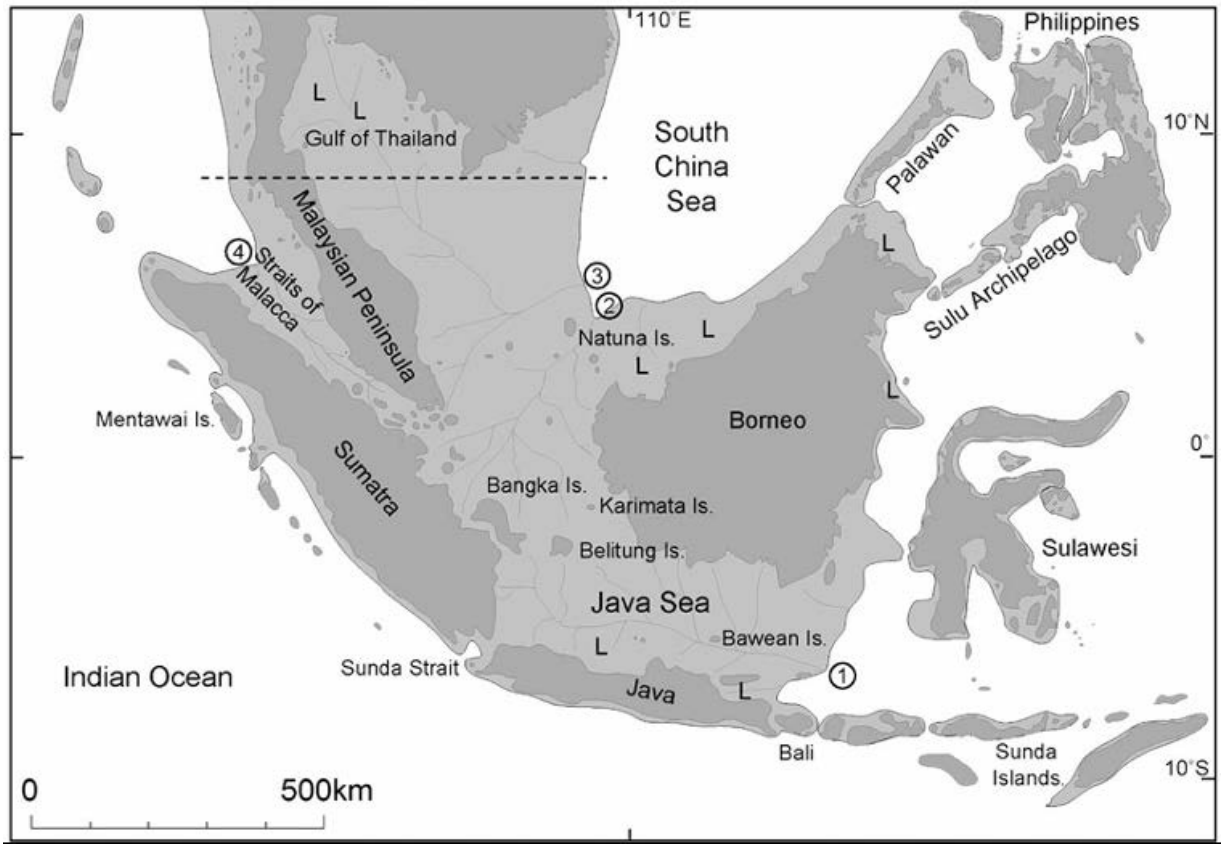

Figure 2. Sundaland at the Last Glacial Maximum, showing the modern distribution of land in dark grey and the additional land exposed during the LGM in light grey (adapted from Voris, 2000).

Figure 3. Study area, Malacca Straits

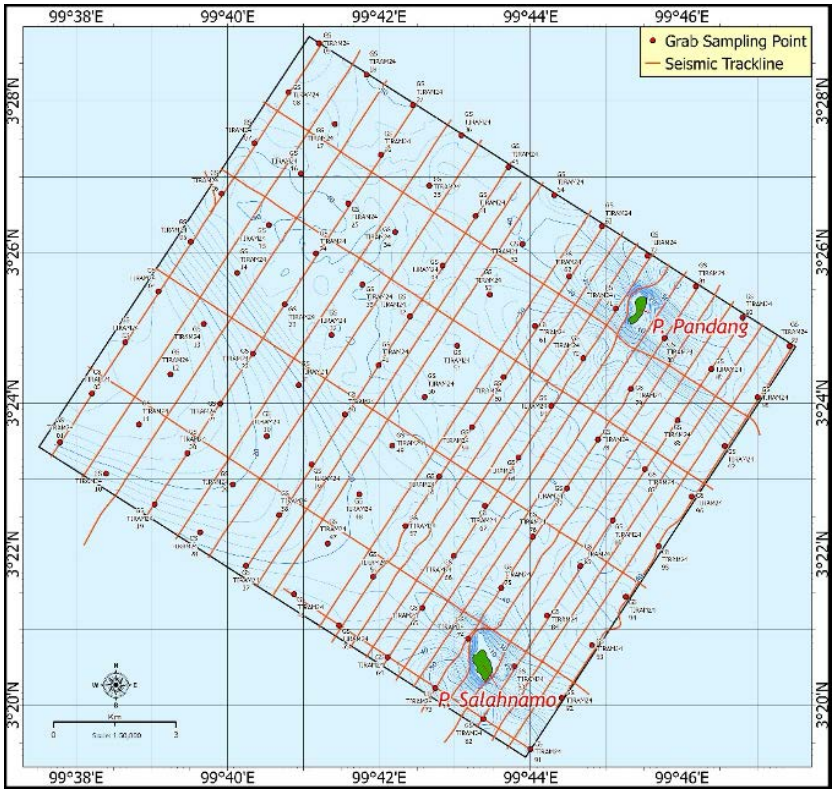

Figure 4. Line survey and locations of seabed sampling

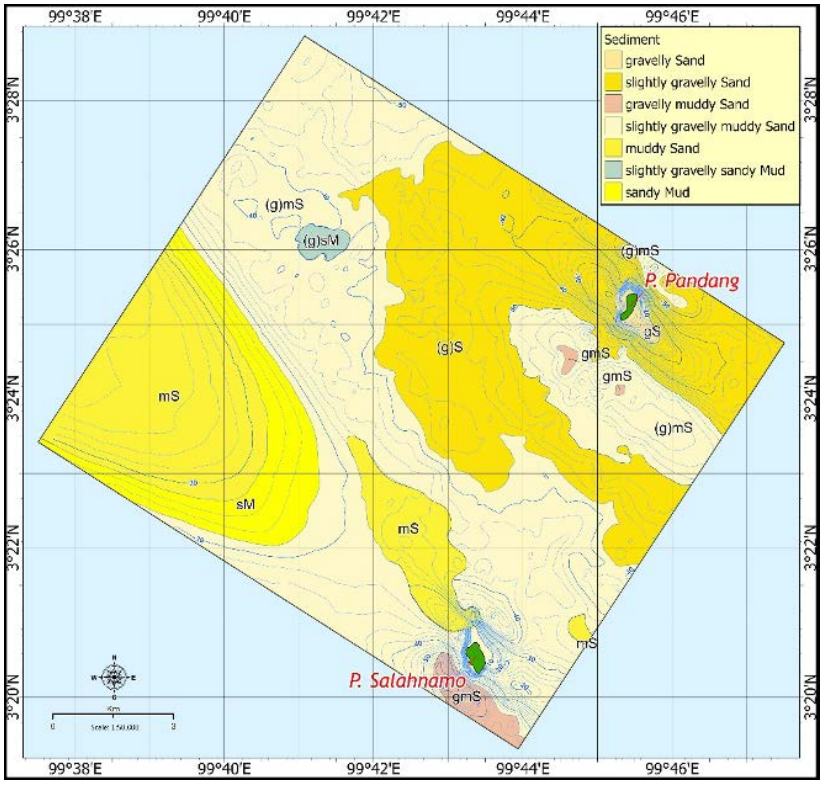

Figure 5. Distribution of Surficial Sediments

RESULTS AND DISCUSSION

Acoustic facies classification is done based on differences acoustics character, sediment types and geomorphological patterns, (Novak, et. al, 2020 and Schulten, et. al, 2023), six acoustic facies (AFI~AFVI) can be identified in this study based on these variations. The acoustic characters are described in detailed on the Table 1 and are illustrated in Figure 6 and Figure 7. The six identified acoustic characters include: gently oblique prograding reflectors, prolonged, transparent, divergent, deformed and chaotic types. The characteristics are generally correlated with sedimentary properties and bottom conditions during sedimentary process.

Acoustic Facies I

This facies is represented by gently oblique prograding reflectors is distributed in the northwestern part of study area. The sea bottom condition identified are smooth and mounded, which can be interpretated as a sand bank. This sand bank likely formed in the Malacca Straits due to its geometric configuration and the influence of surface and bottom currents, potentially triggered by tidal vortices. Tidal vortices are chain of spiral eddies that occur in the environment where strong tides and currents flow through straits. Acoustic blanking has also been identified in these acoustic facies, Indicating the accumulation of significant organic material. The orientation of sand banks is parallel to the shoreline, with an approximate length of 10 to 12 km. This facies was identified in unit I of seismic section (Figure 7). The facies may consist of muddy sand and gravelly muddy sand as shown in Figure 5.

Acoustic Facies II

Facies II, is characterized by a prolonged type, a prolonged type of acoustic facies is characterized by a strong, long-lasting, and often high-amplitude seafloor reflection with very little to no sub-bottom penetration (Dowdeswell, et. al, 2014), is distributed from the center to the northeast part of the study area. The prolonged type is characterized by the disappearance of acoustics signals downward. On seismic profiles, the facies shown irregular surfaces associated with the existence of bedforms of sand waves (Table 1). Depositional sand waves may be associated with strong bottom currents in the center of Malacca Straits.

The grab samples indicate that the surficial sediments on these facies varies from gravelly muddy sand to gravelly sand as shown in Figure 5.

Acoustic Facies III

This acoustic facies is represented by transparent characters. Transparent characters only found in the subsurface unit, known as unit III. These transparent acoustic facies commonly consist of homogenous material. In the Malacca Strait, the most likely depositional environment for these characters to occur is shallow marine. The deposition in the marine environment has repeatedly occurred in the Sundaland due to flooding events started during the Middle Pleistocene (Susilohadi, et. al, 2024).

Acoustic Facies IV

The acoustic facies IV, acoustic facies within the channel, can be divided into three different acoustic facies. Facies IV (a) is characterized by a low lateral continuity of reflector and divergent – clinoform reflectors. Divergent reflector character commonly indicates a lateral sediment variation during the depositional or that the depositional surface tilted progressively (Deng, et.al 2024) but in this study area the lateral variation during the depositional was the most likely cause these acoustic facies. High amplitude and low lateral continuity indicate terrigenous deposition such as inter-bedded channel sands and shales. Terrigenous sediments are commonly made up of sand, mud, and silt, and are usually related to the composition of their source rocks (Cullers and Podkovyrov, 2002).

Facies IV (b) is characterized by chaotic-like reflectors within the channel fill, a chaotic acoustic signature is interpreted as a mixture of sediments, including coarse gravel and heavy minerals, which create an irregular internal structure that reflects seismic waves in a disorganized manner. Facies IV (c) is characterized by homogeneous/transparent reflectors within a channel that might indicate a finer-grained, less mineral-rich sediment, like silt or clay. An erosional truncation is identified at the top of the facies boundary which may an indicator of an erosion during the eustatic depression of sea level fall. During the Last Glacial Maximum (LGM) sea level fall by ~ 120 meters and fully exposed the Sunda Shelf.

Acoustic Facies V

Acoustic facies V is represented by a transparent character. Transparent acoustic reflection in this facies is believed due to weaker acoustic energy and is defined as the acoustic basement.

Acoustic Facies VI

Facies VI is characterized by chaotic reflection pattern. In this study area, this characters associated with granitic intrusive rocks which made up the Islands of Salahnama and Pandang. The rocks can be identified not only on the sea bottom but also on the subsurface, the appearance rock on the seabed manifested by formation of rocky bottom.

The sea dynamics and geometry of Malacca Straits have a significant contribution to recent geological processes; the developments of morphological features such as sand banks and ripple marks are evidence of their contribution. Meanwhile, the granitic belt plays a role as a sediment supplier especially for coarser sediments in the study area, granitic intrusive bodies can be easily identified on the seismic section. Regarding sea dynamics, some features that are important to understand further is the mechanism of sand bank formation that is identified as the acoustic facies I (AFI).

Sea level changes associated with the Last Glacial had an impact on changes in the depositional environment. Depositional environment changes occurred from shallow marine to coastal or terrestrial environments primarily during the transition from Pleistocene to Holocene Epochs. In the seismic section, this change can be easily recognized by erosional truncation.

CONCLUSSIONS

Acoustic facies analysis provides a fast and effective method for characterizing and understanding geological history also identifying potential resources. Acoustic facies I provide evidence on how sand banks can form in the straits through a sea dynamic. Acoustic facies II provide an overview of how sedimentary structures can be formed by strong bottom current and wave. Analysis of acoustic facies, within the channel as seen in the acoustic facies four, can contribute information related to the potential of mineral placers. Chaotic-like reflectors within the channel (acoustic facies IV) have a greater potential of placer mineral rather than divergent-clinoform and homogenous-transparent reflector. Therefore, knowledge of acoustic facies can be used to identify channels that have the potential for placer minerals.

ACKNOWLEDGEMENTS

The authors are indebted to the head of the Marine Geological Institute of Indonesia (MGI) for permission to use the seismic data from this institute. The authors thank to team leader and all members of teams of mineral survey and mapping at Tanjung Tiram Waters, Malacca Straits. The authors also would like to thank all those who have helped and supported this research.

REFERENCES

Bennette, J.D., M.C. Bridge, N.R. Cameron, A. Djunuddin, S.A. Ghazali, D.H. Jeffery, W. Kartawa, W.Keats, N.M.S. Rock dan S.J. Thompson, 1981. *The Geology of the Langsa Quadrangle, Sumatra, Skala 1:250.000.* Pusat Penelitian dan Pengembangan Geologi, Direktorat Jenderal Pertambangan Umum, Departemen Pertambangan dan Energi.

Bird, I. M., Taylor, D., and Hunt, C., 2005. Palaeoenvironments of insular Southeast Asia duringthe Last Glacial Period: a savanna corridor in Sundaland. *Quaternary Science Reviews*: 2228-2242.

Cobbing, E.J., Mallick, D.I.J., Piteld, P.E.J. & Teoh, I.H., 1986. The granites of the Southeast Asian Tin Belt. *Journal of the Geological Society of London*, 143, 537–550.

Cobbing E.J., Pitfield, P. E. J., Darbyshire, D. P. F. AND Mallick, D. I. J., 1992, The granites of the South-East Asian tin belt. *Overseas Memoir 10 British Geological Survey.*

Cobbing, E.J., 2005, Granites, Barber, A.J., Crow, M.J., Milsom, J.S., Sumatra: Geology, Resources and Tectonic Evolution, *Geological Society, London*.

Cullers, R. L., and Podkovyrop, V. N., 2002. The source and origin of terrigenous sedimentary rocks in the Mesoproterozoic Ui group, southeastern Russia. *Precambrian Research* 117 157-183 – Elsevier.

Dowdeswell, J.A., Hogan, K.A., Cofaigh, C. O., Fugelli, E.M.G., Evans, J., Noormets, R., 2014. Late Quaternary ice flow in a West Greenland fjord and cross-shelf trough system: submarine landforms from Rink Isbrae to Uummannaq shelf and slope. *Quartenary Science Review*, 292-309.

Deng, X., Huang, K. and Li, X., 2024. Sedimentary Characteristics and Evolution of the Late Miocene to Quaternary Tributary Channels in the Head of Bounty Channel, *New Zealand. Appl. Sci* 14 6160.

McCourt, W.J., Crow, M.J., Cobbing, E.J., Amin, T.C., 1996. *Mesozoic and. Cenozoic plutonic evolution of SE Asia: Evidence from Sumatra, Indonesia*. Geol. Soc.

Metcalfe, I., (2013). Gondwana Dispersion and Asian Accretion: Tectonic and. Paleogeographic Evolution of Eastern Tethys. *Australian Journal of Earth*.

Mollengraaff, G.A.F., 1921. Modern Deep-Sea Research in the East Indian Archipelago. *Geographical Journal* 57, 95–121.

Novak, A., Smuc, J., Poglajen, S., and Vrabec, M., 2020. *Linking the high-resolution acoustic and sedimentary facies of a transgressed Late Quaternary alluvial plain (Gulf of Trieste, northern Adriatic)*, 419.

Schulten, I. Micallef, A., Krastel. S., Urlaub, M., Gutescher, M. A., and Kopp, H., 2023. *Reconstruction of the 1908 Messina gravity flow (central Mediterranean Sea) from geophysical and sedimentological data*, 459.

Susilohadi, Novico, F., Husson, L., Rahardiawan, R., Prabowo, H., Widodo, J., and Sudjono, E. H., 2024. Quaternary deposition and erosion in the northeastern Sunda Strait: An interplay between sea level, tectonics, and magmatic activity. *Journal of Asian Earth Sciences* X 12.

Van Gorsel, J.T. 2018. *Bibliography Of the Geology of Indonesia and Surrounding Areas Edition 7.0.* https://vangorselslist.com.

Table 1. **Six Acoustic Facies Defined at Study Area**

Acoustic Facies	Acoustic Character/Types	Sediments/Rock	Bottom Condition & Geomorphology	Sedimentary Environments	Interpretation
AFI	gently oblique reflector 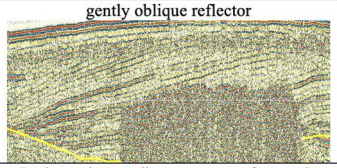	Muddy Sand/Gravelly Muddy Sand	Elongated Shaped Smooth and Mounded Bottom Sand Bank Features	Tidal Vortice along The Straits	Sand banks formed probably due to geometrical aspect and tidal vortices. In several parts below the sand bank was identified acoustic blanking due to presence of gas which is believed to be biogenic in origin.
AFII	Prolonged type, disappearance of acoustic signals to down direction 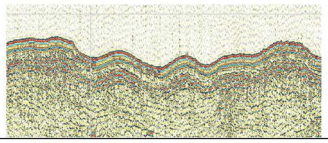	Gravely Muddy Sand – Gravely Sand	Irregular Surface, Sand Wave, Mega Ripple, Rocky Bottom.	Coastal – Shelf Sea	Absorbing of acoustic signals by irregular bottom condition, medium to coarse sediments including gravel and shell fragment. Sand wave and mega ripple identified in the northeast. The appearance this sediment structures associated with strong currents (in the middle of the straits).
AFIII	Transparent type Non-internal reflector in limited thickness 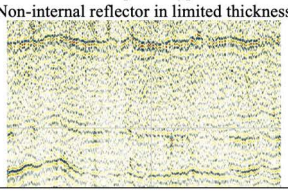	Homogeneous Sediments	-	Shallow Marine	Transparent acoustic reflection commonly occurred due to penetrating of acoustic signal to soft homogeneous sediments.
AFIV	Low lateral continuity of reflector, Divergent-Clinoform Reflector 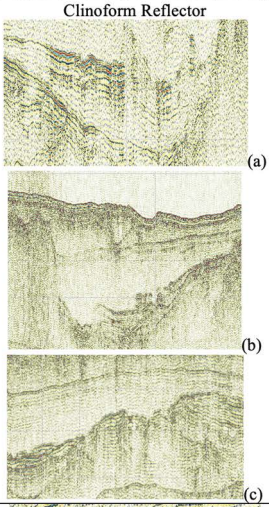 (a) (b) (c)	Terrigenous Sediments	-	Terrigeneous Depositional	(a) Divergent-clinoform reflectors indicate that there were lateral variations in depositional rates or that the depositional surface tilted progressively. (a) High amplitude and low lateral continuity indicate terrigenous deposition such as inter-bedded channel sands and shales. (b) Chaotic-like reflectors within the channel fill, a chaotic acoustic signature is interpreted as a mixture of sediments, including coarse gravel and heavy minerals, which create an irregular internal structure that reflects seismic waves in a disorganized manner. (c) Homogeneous/Transparent reflectors within a channel might indicate finer-grained, less mineral-rich sediment, like silt or clay.
AFV	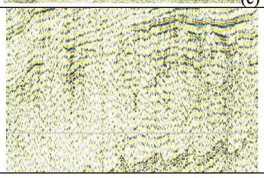	Sedimentary Rocks	-	Shallow Marine	Transparent acoustic reflection in these facies occurred due to weaker acoustic energy
AFVI	Chaotic 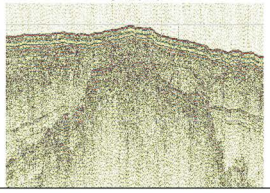	Granitic Intrusive Rocks	Irregular Surface, Rocky Bottom	-	Intrusive granitic rocks identified in the survey area by chaotic character as an internal reflector.

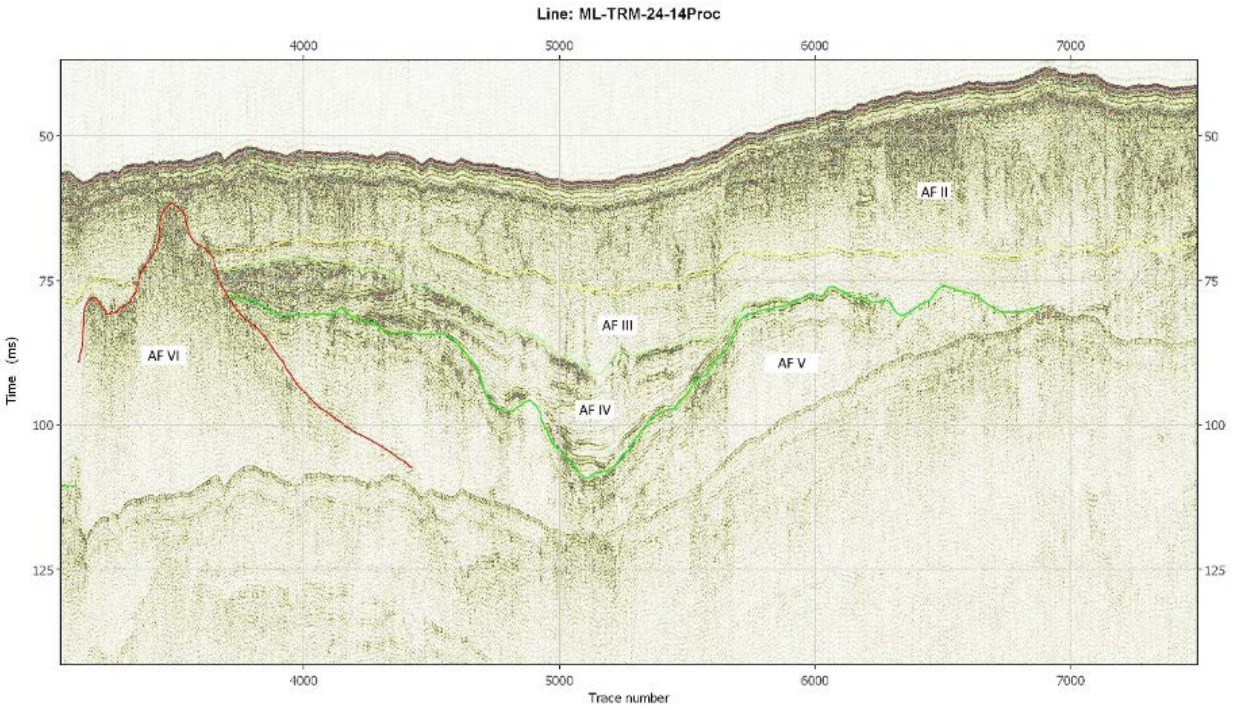

Figure 6. Seismic section line 14 and interpretation of acoustic facies within the line

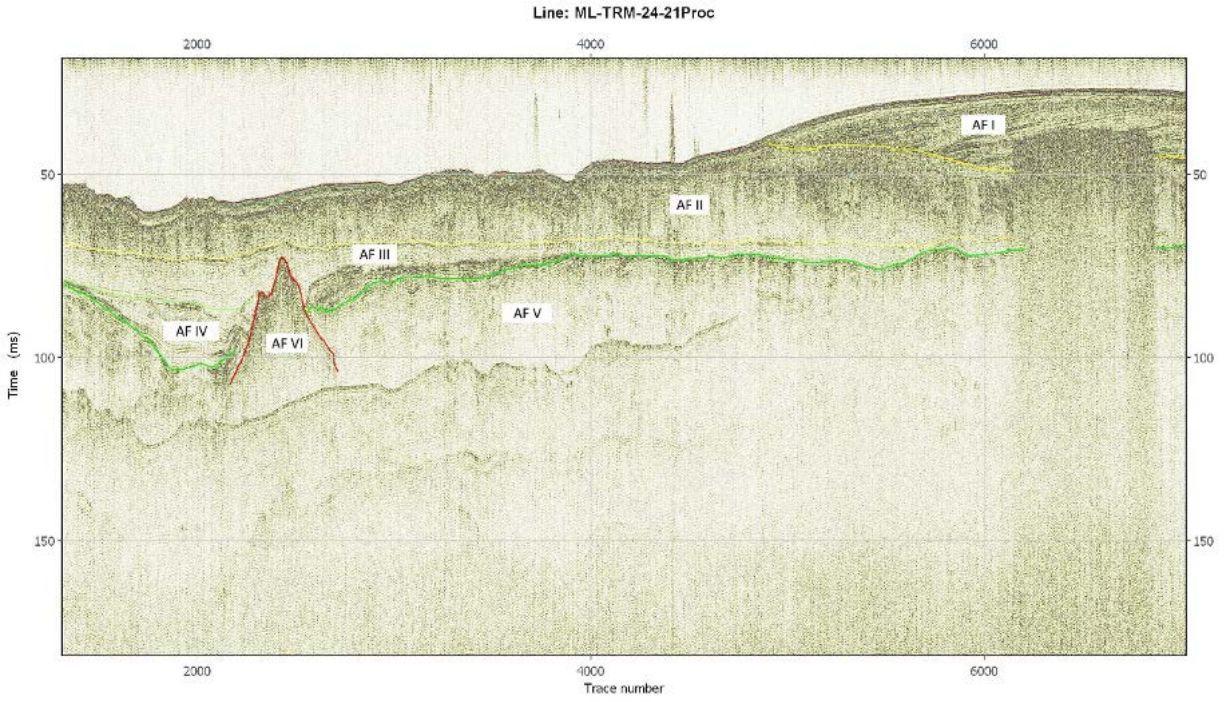

Figure 7. Seismic section line 21 and interpretation of acoustic facies within the line

IDENTIFICATION OF EARTHQUAKE AND TSUNAMI RISK ZONES IN SOUTHERN JAVA USING GRAVITY METHOD

IDENTIFIKASI ZONA RISIKO GEMPA BUMI DAN TSUNAMI DI SELATAN JAWA MENGGUNAKAN METODE GAYA BERAT

Isna Karima[1*], Agustya Adi Martha[2], Nurul Hudayat[2*], Tati Zera[1]

[1] Physics, Faculty of Science and Technology, UIN Syarif Hidayatullah Jakarta, Jakarta
[2] National Research and Innovation Agency - BRIN, Jakarta

*Corresponding author: nurul.hudayat@brin.go.id

(Received 27 March 2025; in revised from 28 March 2025; accepted 29 December 2025)

DOI : 10.32693/bomg.40.2.2025.934

ABSTRACT: The southern part of Java has a high level of disaster risk because it is affected by a subduction zone where the Indo-Australian plate thrusts beneath the Eurasian plate. Six tsunami events occurred in the southern part of Java, caused by earthquakes in the area, based on BMKG catalogue data from 416 to 2023. Given the very large population on the island of Java, the possibility of causing more casualties is greater. Therefore, it is very necessary to have thorough mitigation preparation to estimate the possibility of areas experiencing a large earthquake that triggers a tsunami. This study aims to determine areas with a high level of earthquake and tsunami risk distribution using the gravity method with data from the TOPEX satellite in the form of free air anomaly data and topographic data. After data processing and an anomaly map were obtained, it showed that areas with a high level of earthquake risk were located around the subduction zone and Java Trench. This is due to the geological conditions of the southern part of Java, located in the subduction zone where many active faults were found.

Keywords: Earthquake, tsunami, gravity, subduction zone, Southern Java

ABSTRAK*: Wilayah selatan Jawa memiliki tingkat risiko bencana yang tinggi karena terletak pada zona subduksi yang terbentuk akibat aktivitas tumbukan lempeng Indo-Australia yang menunjam ke lempeng Eurasia. Sebanyak enam kejadian tsunami terjadi di wilayah selatan Jawa yang disebabkan oleh gempa bumi di wilayah tersebut berdasarkan data katalog BMKG dari tahun 416 sampai dengan tahun 2023. Mengingat jumlah penduduk di Pulau Jawa yang sangat banyak, maka kemungkinan menimbulkan korban jiwa yang lebih banyak menjadi lebih besar. Oleh karena itu, sangat diperlukan persiapan mitigasi yang matang untuk memperkirakan kemungkinan wilayah mengalami gempa bumi besar yang memicu tsunami. Penelitian ini bertujuan untuk mengetahui wilayah dengan tingkat sebaran risiko gempa bumi dan tsunami yang tinggi menggunakan metode gayaberat dengan data dari satelit TOPEX berupa data anomali udara bebas dan data topografi. Setelah dilakukan pengolahan data dan diperoleh peta anomali, menunjukkan bahwa wilayah dengan tingkat risiko gempa bumi yang tinggi berada di sekitar zona subduksi dan palung Jawa. Hal ini berdasarkan kondisi geologi wilayah selatan Jawa yang berada pada zona subduksi dan banyak ditemukan patahan aktif.*

Kata Kunci: *Gempa bumi, tsunami, gaya berat, zona subduksi, Selatan Jawa*

INTRODUCTION

Java Island has complex geological conditions and is characterized by high seismic activity due to the influence of an active seismotectonic arc system, resulting in a high level of disaster risk (Anggarajati et al., 2024). Earthquakes arise from seismic processes associated with the sudden release of accumulated energy within the Earth, which is characterized by the rupture of rock layers (Prananda et al., 2022).

The released energy is generally generated by the accumulation of stress along the plate boundary, which progressively increases until it exceeds the strength of the rocks and induces rupture. In Java, seismicity is commonly categorized into earthquakes originating from the southern Java subduction zone and those associated with the active Java fault zone. Earthquakes within the subduction zone occur at shallow to deep depths and typically have magnitudes greater than 4 Mw. Large-magnitude events of up to 8.5 Mw have been recorded in western Java, whereas earthquakes of 5–6 Mw are common along the southern part of the island. Subduction-zone earthquakes generally exhibit thrust and normal-fault mechanisms, while horizontal (strike-slip) mechanisms are rarely observed in this subduction (Jayadi et al., 2023).

Earthquakes with thrust-fault mechanisms have been documented along the Cimandiri Fault, including the Gandasoli Sukabumi (1982) and Cibadak Sukabumi (2000) events. A similar thrust-fault mechanism was identified for the 1990 Majalengka earthquake on the Baribis Fault. Right-lateral strike-slip fault was recorded during the 1995 Bumiayu earthquake along the Bumiayu Fault, whereas the 2006 Yogyakarta earthquake exhibited a left-lateral strike-slip mechanism. Normal-fault earthquakes, meanwhile, are associated with extensional processes within the seismic gap zone (Soehaimi, 2008).

The gravity method is a geophysical technique used to detect subsurface density. This method has been applied to identify fault structures (Martha et al., 2023), hydrocarbon exploration (Juwita et al., 2024; Wibowo et al., 2024) and evaluate geothermal prospects (Hudayat et al., 2024). For earthquake and tsunami mitigation, gravity data can support regional assessments by delineating structurally vulnerable zones in southern Java and identifying areas with elevated seismic and tsunami hazard potential.

Geological Setting

Java Island is characterized by complex tectonic conditions resulting from the convergence between the Indo-Australian Plate, which is subducting beneath the Eurasian Plate (Haryanto, 2006). This convergent interaction produces recurrent episodes of tectonic compression and extension, generating frequent seismicity associated with several active fault systems (Helmi and Haryanto, 2008). Three major active surface-expressed faults—the Cimandiri, Baribis, and Lembang faults—were formed through tectonic processes operating from the Cretaceous to the Quaternary (Haryanto, 2006).

The southern margin of Java constitutes a convergent plate boundary forming an active subduction zone driven by the motion of the Indo-Australian Plate. As a result, Java is situated within a region of elevated seismicity due to its location along this subduction corridor (Indriana, 2008). This subduction pathway is part of a shallow megathrust system extending approximately 5,500 km from south of Bangladesh and continuing along the western and southern margins of Sumatra, Java, Bali, and into eastern Indonesia (Saraswati and Anjasmara, 2014).

The geological setting of Java within the megathrust zone confers a high level of geohazard potential, particularly the possibility of large earthquakes occurring within existing seismic gap segments. Such major seismic events may influence volcanic activity and can generate tsunamis, given that large offshore earthquakes are one of the primary tsunami-generating mechanisms (Ashar, 2017). Considering Java's dense population relative to other regions, the potential impacts are substantial. Consequently, comprehensive mitigation planning is essential to anticipate areas that may experience significant seismic events (Erlangga, 2020).

METHODS

The data used in this study consist of secondary gravity and topographic datasets totaling 87,966 measurement points. These datasets were obtained from the TOPEX satellite altimetry database (TOPEX, 2025). The gravity anomalies are derived from satellite radar altimetry, in which satellites such as TOPEX/Poseidon, GEOSAT, and ERS-1—operating at altitudes of approximately 800 km—emit microwave pulses toward the ocean surface. The recorded two-way travel time yields precise sea surface height (SSH) relative to a reference ellipsoid. Because the ocean surface closely conforms to the

geoid, SSH reflects variations in the Earth's gravitational field.

Along-track SSH profiles are differentiated to obtain sea surface slopes (vertical deflections), which are resolved into north–south and east–west components. These slope components are subsequently transformed into gravity anomalies using Fourier-based processing techniques designed to reduce long-wavelength errors and enhance short-wavelength signals that are attenuated by ocean depth (~4 km). The effective resolution is constrained by altimeter noise arising from ocean-surface roughness, with a typical measurement precision of 10–20 mm after averaging. This supports along-track resolutions of approximately 20–30 km (e.g., ~24 km for combined GEOSAT/ TOPEX global coverage) and gridded products at ~2 arc-minutes (~3.7 km at the equator). However, upward continuation effects limit the reliability of wavelengths shorter than ~20 km, and comparisons with shipborne gravity measurements indicate anomaly accuracies on the order of 4–7 mGal (Sandwell and Smith, 1997).

The acquired gravity data were processed using conventional gravity-method procedures. This method measures spatial variations in gravitational acceleration produced by density contrasts within the subsurface. Its fundamental basis follows Newton's law of universal gravitation (Telford et al., 1990), which states that the attractive force between two masses m_1 and m_2 separated by distance r is: (Equation 1)

$$\boldsymbol{F} = \gamma \frac{m_1 m_2}{r^2} \hat{\mathrm{r}} \quad (1)$$

F is the force generated between two particles of mass m_1 and m_2, r is the distance between the two particles, r^ is the unit vector of m_1 and m_2, and γ is the universal gravitational constant (6.6732×10^{-11} N m^2/kg^2).

Measurements of gravitational acceleration at the Earth's surface are affected by variations in latitude, topography, elevation, Earth–Sun positional effects, and subsurface density heterogeneity (Basid and Hidayat, 2011). To quantify these density contrasts, gravity anomalies are obtained by comparing observed gravity values with corresponding theoretical gravity at the same location. In this study, the complete Bouguer anomaly was calculated using Equation 2 (Telford et al., 1990):

$$CBA = FAA - BC + TC \quad (2)$$

where CBA denotes the complete Bouguer anomaly, FAA is the free air anomaly, BC represents the Bouguer Correction, and TC is the Terrain Correction, all expressed in mGal.

RESULTS AND DISCUSSION

The study area extends from West Java to Central Java, within coordinates 107.010°E to 111.70°E and 9.00°S to 5.00°S. This research utilizes topographic data and gravity anomaly data retrieved from the Topex website. Following initial preprocessing, a topographic map was generated, as presented in Figure 1. Based on the resulting topographic map, high-elevation regions are represented by red to pink zones, with elevation values ranging from approximately 0.228 m to 3014.34 m. These areas correspond to the upland physiographic domains of West Java and Central Java, consistent with the mountainous terrain along the southern segment of Java Island, including prominent ranges such as the Dieng Complex Volcano. Medium elevations are depicted by yellow to orange zones, spanning –1075.18 m to 0.228 m. Low-elevation zones, indicated by blue to green ranges from –6645.07 m to –1075.18 m, represent the Indian Ocean bathymetry and are associated with the southern Java subduction system.

Overall, the integrated topographic and bathymetric map delineates the major physiographic gradients across Java Island—from highland regions to the deep oceanic basin. When interpreted in the context of regional tectonics, these morphological patterns indicate the convergent interaction between the Eurasian Plate and the Indo-Australian Plate along the southern margin of Java.

corrections applied to the Free-Air Anomaly and topographic data yield the Bouguer anomaly map as shown in Figure 2 reveals subsurface density variations in the study area. The Bouguer anomaly values rangebetween -175 mGal to 171.52 mGal and are categorized into three groups. The high anomaly values, ranging from 51.89 mGal to 171.52 mGal, are represented by red to pink colors. Moderate anomalies, spanning from 20.53 mGal to 51.89 mGal, appear as yellow to orange zones. The low anomalies, have values between -175.00 mGal to 20.53 mGal, are indicated by blue to green colors. The distribution pattern shows high anomalies around the Java Island and the Java Trench, while low anomaly values dominate the Indian Ocean area.

The transition from blue to green on the map suggests the location of the Java subduction zone.

The Bouguer anomaly map shown in Figure 2 range from –175 mGal to 171.52 mGal, are classified into three main categories. High anomaly values between (51.89–171.52 mGal) are represented by red to pink color, moderate anomalies (20.53–51.89 mGal) are depicted in yellow to orange, and low anomalies (–175.00–20.53 mGal) appear in blue to green.

The spatial distribution indicates that high anomalies are concentrated around Java Island and the Java Trench, while low anomalies are predominant in the Indian Ocean region. The gradational change from blue to green on the anomaly map marks the transition zone associated with the Java subduction system, reflecting contrasts in crustal density between the overriding and subducting plates.

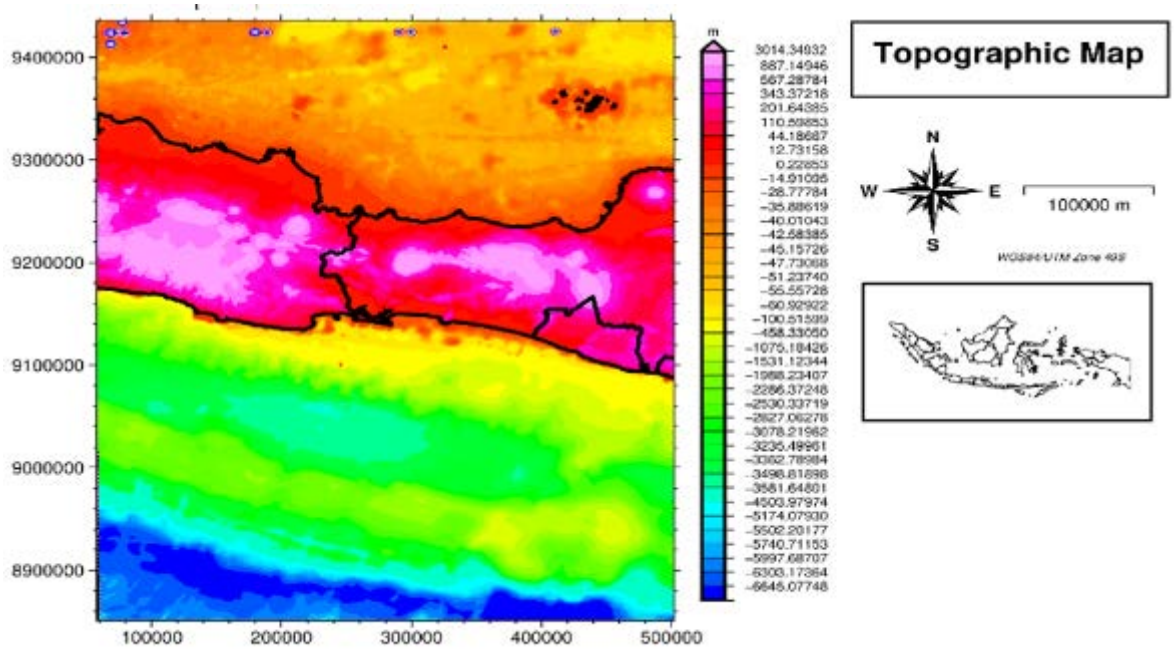

Figure 1. Topographic and bathymetric map of the study area showing elevation variations from Onshore Java to the Java Trench.

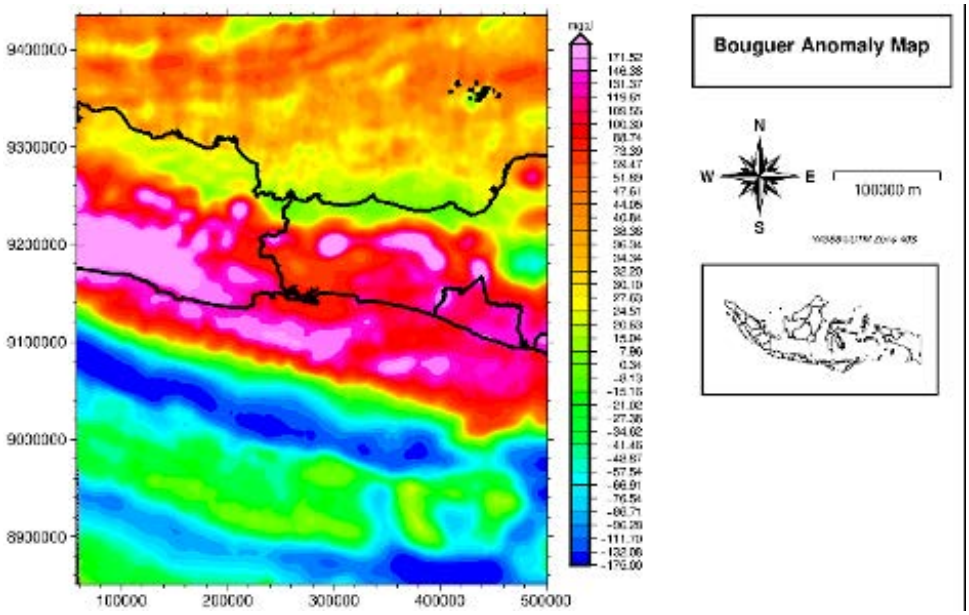

Figure 2. Complete Bouguer anomaly map presenting the gravity field, used to delineate density contrasts and regional structural trends.

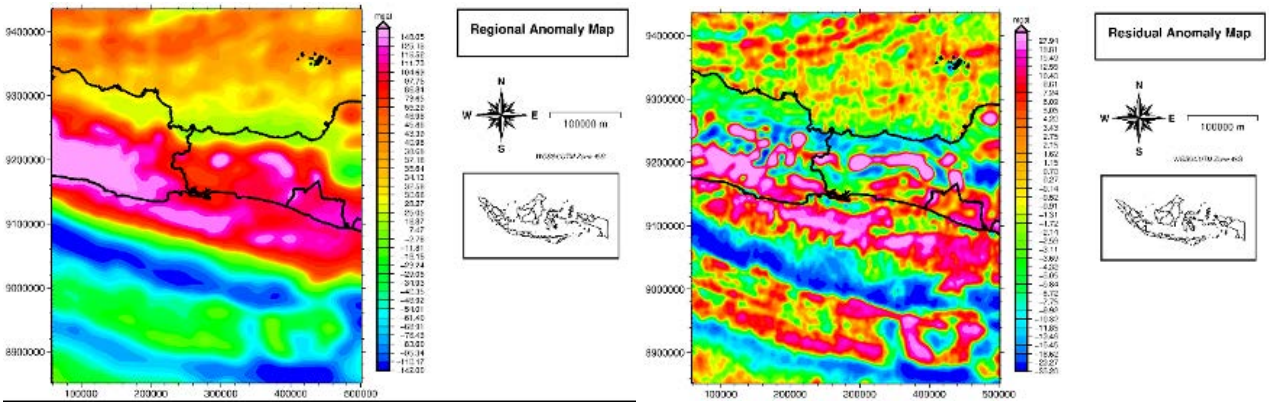

Figure 3. Regional gravity anomaly; (b) residual gravity anomaly derived from separation of long and short wavelength components.

The gravity anomalies were filtered to minimize noise and suppress unwanted interference. In this study, an upward continuation filter was applied to the gravity data, extending the field to an elevation of 5 km. This technique effectively transforms gravity observations at the surface into their equivalent response at a higher measurement level. The resulting upward-continued field yields a regional anomaly map with a smoother character, implying a more homogeneous distribution of long-wavelength anomalies. As shown in Figure 3a, the regional anomaly map reveals that high-gravity values are concentrated across Java, whereas the low-gravity zones, depicted in green, delineate the subduction system south of Java.

In contrast, the residual anomaly map (Figure 3b) exhibits a more heterogeneous, high-frequency anomaly pattern, reflecting density contrasts within the shallow subsurface. High residual anomalies are distributed across Java Island and within the Java Trench. However, several localized high-residual anomalies also occur in areas interpreted as part of the subduction zone, deviating from the expected pattern. Under typical conditions, low-gravity anomalies are anticipated in such settings due to the presence of thick sedimentary sequences or relatively low-density crustal materials. The occurrence of high anomalies in these regions may instead be attributed to local geological structures, such as uplifted crustal blocks, magmatic intrusions, or shallow, dense lithologies (Novitri et al., 2025).

The second vertical derivative (SVD) map was performed to enhance the characterization of subsurface density variations by amplifying short-wavelength gravity gradients. This method is effective for delineating major geological structures such as faults, lithological contacts, and potential indicators of natural resources or geohazards.

In the SVD map shown in Figure 4, the anomalous values exhibit a distinct distribution, divided into positive (red–yellow) and negative (blue–green) zones. Positive SVD values represent

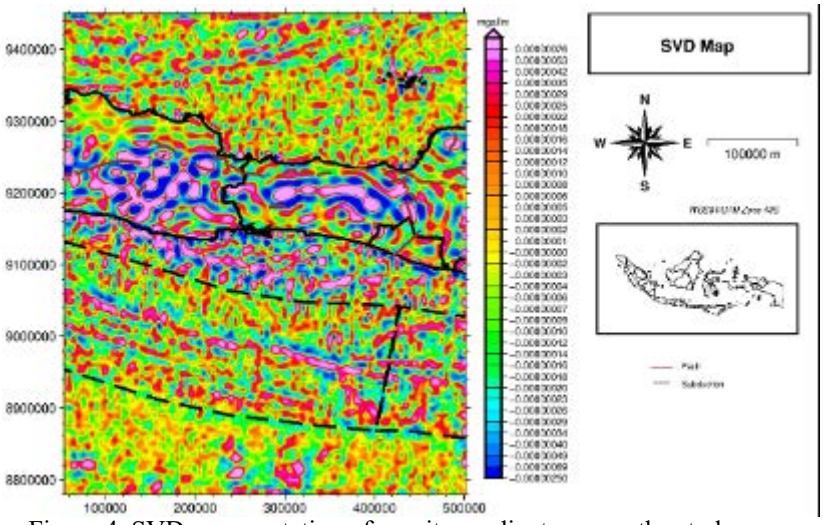

Figure 4. SVD representation of gravity gradients across the study area.

short-wavelength, high-frequency anomaly zones commonly associated with sharp lithological boundaries or near-surface structural discontinuities. These positive values, however, do not directly indicate higher-density rocks and must be interpreted in relation to local geological conditions.

Negative SVD values correspond to short-wavelength, low-frequency anomalies that may delineate structural depressions such as sedimentary basins or normal-faulted blocks. Similar to the positive anomalies, these values do not inherently signify lower-density rocks but instead emphasize the geometry of subsurface structures.

The sharp transitions between positive and negative SVD zones likely represent major structural boundaries, including fault systems or fold hinges, reflecting zones of significant lateral density variation.

SVD also reveals a contrast between high and low anomalies over short distances toward the southwestern and southern parts of the study area. When qualitatively analysed and correlated with regional geological data, the anomaly pattern is consistent with features that may be associated with the subduction zone. However, as SVD enhances high-frequency components related to shallow density contrasts, interpretations regarding deeper structures such as subduction zones must be made cautiously and supported by additional geophysical evidence. The observed patterns include linear trends that may indicate active faults and major tectonic boundaries. A dominant anomaly trend aligns with the subduction direction in the southern part of Java, suggesting the influence of subduction-related crustal deformation due to interactions between oceanic and continental plates. Additionally, anomaly patterns oriented west-east and southwest-northeast likely correspond to the regional fault system in West Java and Central Java, further supporting the presence of significant active faulting and crustal deformation.

On the tsunami distribution map shown in Figure 5 a) there are six events that have occurred on the island of Java based on data from the BMKG catalog from 416 to 2023. It is important to note that records before the modern instrumental period are historical reconstructions with high uncertainty and should be interpreted cautiously. Point 1 corresponds to the Pangandaran tsunami, which occurred on July 17, 2006, at longitude 107.314° E and latitude 9.672° S, associated with an earthquake of magnitude 7.0 Mw. Point 2 marks the tsunami event near Pelabuhan Ratu, on September 2, 2009, located at longitude 107.32° E and latitude 8.24° S, triggered by the 7.3 Mw Tasikmalaya earthquake. Point 3 (blue) denotes an earthquake that occurred in the Java Sea in 1823 with a magnitude of 6.8 Mw. Point 4 represents an earthquake whose shaking reached the Semarang region of Central Java in 1840, although its magnitude remains unknown. Point 5 marks the October 20, 1859 event, during which a tsunami was reported in Pacitan. Point 6 corresponds to the September 11, 1921 earthquake, which had a magnitude of 7.5 Mw and generated a tsunami observed at Parangtritis, Yogyakarta.

The earthquake distribution map in Figure 5(b) shows seismic events that occurred in the southern part of Java from 2004 to 2024 with magnitudes exceeding 2.5 Mw. The analysis indicates that earthquake clusters are concentrated along the subduction zone, the Java Trench, and onshore Java. This pattern corresponds with the distribution of active fault segments documented in the 2017 active fault database compiled by PusGEN, an agency under the Ministry of Public Works and Housing responsible for earthquake mitigation. The high seismicity in these regions reflects

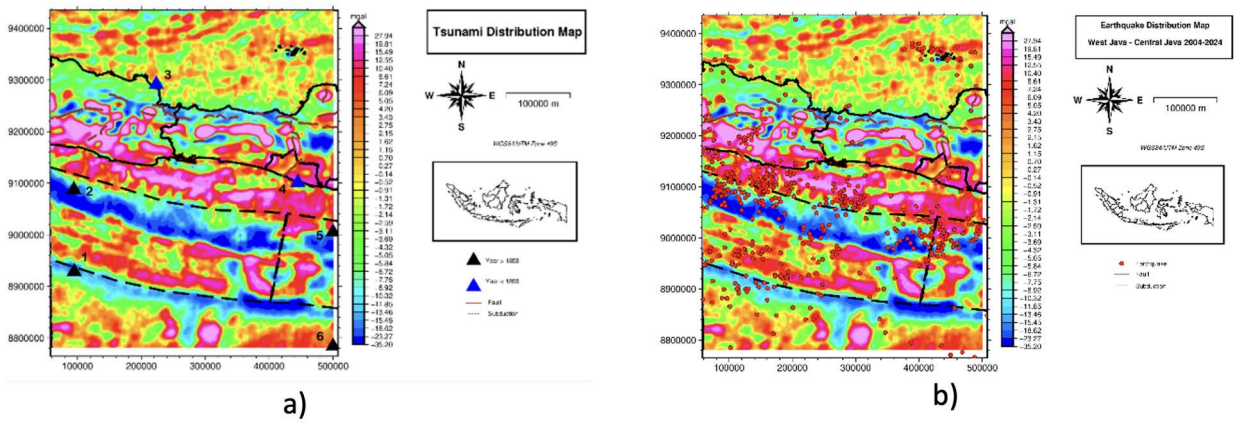

Figure 5. (a) Map showing the locations of tsunami events recorded around Java. (b) Earthquake distribution map illustrating seismic activity in the southern Java region between 2004 and 2024.

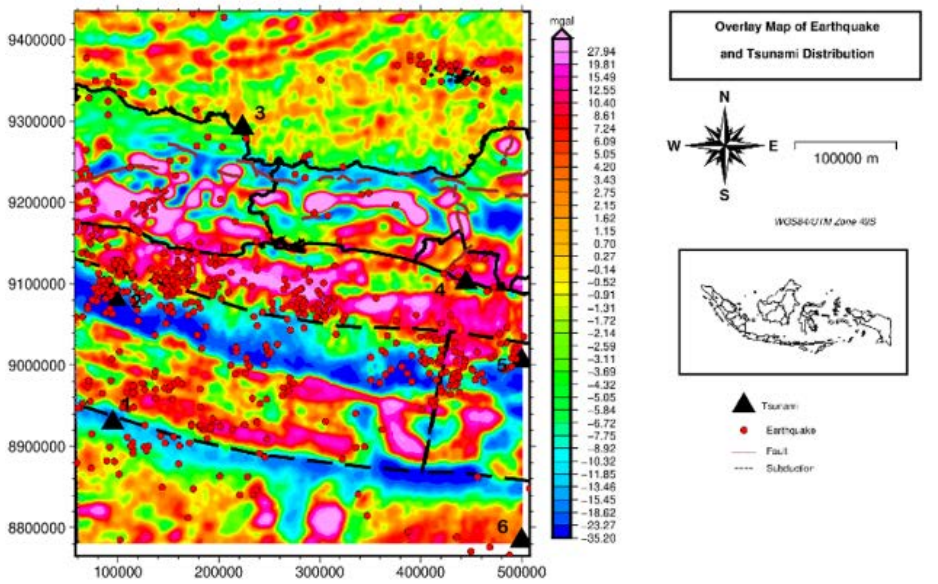

Figure 6. Overlay Map of Earthquake and Tsunami Distribution

ongoing tectonic processes associated with deformation along these active fault systems.

Tsunami occurrences in the study area are generally concentrated near earthquake epicenters and active fault segments, as illustrated in Figure 6. The map shows the distribution of seismic events alongside tsunami-generation points (indicated by black triangles) across southern Java. The presence of these points suggests that certain earthquakes meet the conditions necessary to generate tsunamis. However, tsunami generation is controlled not only by earthquake magnitude but also by fault mechanism, focal depth, event location (offshore vs. onshore), slab geometry, and the extent of seafloor deformation.

The Java subduction zone south of the island is a well-known source of large interplate thrust, or megathrust, earthquakes capable of producing significant tsunamis along the southern coast. A notable example is the Mw 7.7 Pangandaran earthquake in 2006, which triggered a destructive tsunami in West and Central Java due to its shallow thrust mechanism and associated seafloor displacement. It is important to emphasize that not all earthquakes in southern Java generate tsunamis; tsunamigenic events predominantly arise from shallow megathrust earthquakes occurring along the subduction interface.

Red to yellow colors denote high-elevation regions, representing mountainous terrain on land or bathymetric highs such as submarine ridges. In contrast, green to blue colors indicate lower elevations, encompassing coastal lowlands and the seafloor. This pattern shows that much of the southern coast of Java is characterized by low-lying topography, making these areas generally more susceptible to tsunami inundation should a major earthquake occur along the subduction zone.

Higher-elevation areas, such as the mountainous regions of Central Java, are comparatively less exposed to tsunami hazards, provided they lie sufficiently inland or away from steep coastal slopes. Nonetheless, these elevated zones remain seismically active due to the presence of inland fault systems, although not all faults in Central Java produce large earthquakes; several generate only shallow, small-to-moderate magnitude events.

CONCLUSSIONS

Based on the findings of this study, high residual anomaly values are distributed across onshore Java, the Java Trench, and the adjacent subduction zone. The Java subduction system is marked by intense seismicity along the convergent interface between the Indo-Australian and Eurasian plates. The overlay of earthquake and tsunami distributions demonstrates that most seismic events cluster near the subduction boundary, where plate convergence generates substantial tectonic stress. Shallow megathrust earthquakes in this zone are particularly capable of producing tsunamis that pose hazards to the southern coast of Java.

In addition, several earthquake epicenters are dispersed across Java Island, reflecting the presence of active inland fault systems capable of generating tectonic earthquakes within the region.

ACKNOWLEDGEMENTS

We would like to express our deepest gratitude to BRIN and LPDP for the support and funding provided for our research titled 'Earthquake Monitoring System'. This publication is one of the outputs of the research funding program. This support is very meaningful in the development of research aimed at enhancing earthquake monitoring and disaster mitigation in Indonesia.

REFERENCES

Anggarajati, B., Yatini, Y., dan Raharjo, W., 2024. Application of K-means clustering and B-value algorithms for analysis of earthquake dangerous zones in Java Island. *International Journal of Advances in Applied Sciences*, 13(4): 907–915.

Ashar, M.I., 2017. Subsurface modeling of the South West Java subduction zone based on gravity field anomaly data. *Youngster Physics Journal*, 6(4): 382–387.

Basid, A., dan Hidayat, N., 2011. Gravity anomaly analysis as a reference in determining the subsurface geological structure and geothermal potential (Case study in Songgoriti Area, Batu City). *Jurnal Neutrino*, 4(1): 35–47.

Erlangga, W., 2020. Characteristics and parameters of subduction sources of earthquake on Java Island. *TEKNISIA*, 25(2): 88–98.

Haryanto, I., 2006. Paleogen and Neogen geological structure in West Java. *Bulletin of Scientific Contribution: Geology*, 4(1): 88–95.

Helmi, F., dan Haryanto, I., 2008. Regional structural pattern of West Java. *Bulletin of Scientific Contribution: Geology*, 6(1): 57–66.

Hudayat, N., Rahman, S.A.N., Martha, A.A., Sutrisno, S., dan Wulandari, A., 2024. Identification of subsurface structures and potential reservoir zones of geothermal fields based on gravity data analysis in the Karaha–Cakrabuana Area, West Java. *Iranian Journal of Geophysics*, in press.

Indriana, R.D., 2008. Analysis of the subduction plate tilt angle in South Central Java and East Java based on gravity anomalies and volcanic tectonic implications. *Berkala Fisika*, 11(3): 89–96.

Jayadi, H., Janat, N.R., Santosa, B.J., Warnana, D.D., Nugraha, A.D., Leopatty, H., Asyhar, I.F., Meidji, I.U., Fitriana, T., dan Ninasafitri, 2023. Hypocenter relocation of local earthquake using double difference method in Central Sulawesi from BMKG network data: Time periods of July 26 – August 18, 2021. *IOP Conference Series: Earth and Environmental Science*, 1157(1): 012023.

Juwita, W., Juventa, J., Setiawan, A.M., Martha, A.A., Hudayat, N., dan Sutedja, B., 2024. Identification of potential hydrocarbon traps using the gravity method in the Bengkulu Basin. *Iranian Journal of Geophysics*, 18(3): 69–83.

Martha, A.A., Setiawan, A., dan Setiadi, T.A.P., 2023. Utilization of global gravity model plus (GGMPlus) to identify fault structures in Mamasa District, West Sulawesi. *AIP Conference Proceedings*, 030006: 1–6.

Novitri, A., Margiono, R., Pevriadi, A., Zakaria, H., dan Segoro, Y.A., 2025. Modeling of three-dimensional subsurface structures based on gravity anomaly in Southwest Sumba, Indonesia. *Indonesian Physical Review*, 8(1): 253–267.

Prananda, Y., Zera, T., dan Sunarya, D., 2022. Analysis of the spatial and temporal distribution of seismotectonic parameters in the West Java and Banten region based on the A-value and B-value for the period 1971–2021. *Buletin Meteorologi, Klimatologi, dan Geofisika*, 2(3): 24–34.

Sandwell, D.T., dan Smith, W.H.F., 1997. Marine gravity anomaly from Geosat and ERS-1 satellite altimetry. *Journal of Geophysical Research*, 102(B5): 10039–10054.

Saraswati, A.T., dan Anjasmara, I.M., 2014. Analysis of gravity anomaly on the condition of tectonic setting of Sunda Megathrust subduction zone in the west of Sumatera Island. *Geoid*, 10(1): 75–80.

Soehaimi, A., 2008. Seismotectonics and earthquake potential in Java region. *Indonesian Journal on Geoscience*, 3(4): 227–240.

Telford, W.M., Geldart, L.P., dan Sheriff, R.E., 1990. *Applied Geophysics*. Cambridge University Press, Cambridge, 770p.

TOPEX, 2025. Marine gravity from satellite altimetry.

https://topex.ucsd.edu/cgi-bin/get_data.cgi [Accessed on 12 January 2025].

Wibowo, R., Setiadi, I., Firdaus, Y., dan Rahardian, R., 2024. Gravity modeling of subsurface structures and reservoir characterization using seismic inversion in the Nias Basin. *Bulletin of the Marine Geology*, 39(2): 69–84.

GEOCHEMISTRY OF SEABED AND COASTAL SEDIMENTS IN LIMAU WATERS AREA

GEOKIMIA SEDIMEN DASAR LAUT DAN PANTAI DI PERAIRAN LIMAU DAN SEKITARNYA

Muhammad Zulfikar*, Eko Saputro, Ali Albab, Riza Rahardiawan

Marine Geological Institute, Jl. Dr. Junjunan no.236, Bandung

*Corresponding author: muhammad.zulfikar@esdm.go.id

(Received 03 July 2025; in revised from 04 July 2025; accepted 29 December 2025)

DOI : 10.32693/bomg.40.2.2025.953

ABSTRACT: Sediment provenance and weathering history are used to understand sedimentary processes and to explore mineral potential in coastal–marine systems in the Limau Waters. Therefore, the characteristics of seabed and coastal sediments need to be determined. This study aims to identify the source rocks, paleoweathering signatures, and sediment maturity of both seabed and coastal sediments through a geochemical approach. A geochemical approach that integrates major oxide and rare earth element (REE) analyses, the paleoweathering, and sediment maturity indices, is used to identify the source rocks of these sediments. Major oxides elements were measured using X-ray fluorescence (XRF) and REE concentrations were determined using inductively coupled plasma - optical emission spectrometry (ICP-OES) and inductively coupled plasma optical - mass spectrometry (ICP-MS). Geochemical discrimination diagrams indicate that seabed sediments are mainly derived from intermediate to felsic igneous rocks with higher compositional maturity, whereas coastal sediments are influenced by mafic volcanic rocks and are comparatively immature in composition. Both sediment types exhibit weak chemical weathering (CIA < 70), suggesting limited alteration of young volcanic sources. The CIA–ICV relationships portray contrast sediment transport and depositional processes between the coastal and marine environments. This study is expected to provide a geochemical-based framework for provenance analysis and to support the development of insights for future marine mineral exploration in the Limau Waters area.

Keywords: Marine sediment geochemistry, provenance analysis, chemical weathering, Limau Waters

ABSTRAK: *Asal usul sedimen dan sejarah pelapukan digunakan untuk memahami proses sedimentasi dan mengeksplorasi potensi mineral di sistem pesisir-laut Perairan Limau. Oleh karena itu, perlu dilakukan penentuan karakteristik pada sedimen dasar laut dan pesisir. Penelitian ini bertujuan untuk mengidentifikasi batuan sumber, jejak pelapukan purba, dan tingkat kematangan sedimen pada sedimen dasar laut maupun sedimen pantai melalui pendekatan geokimia. Pendekatan geokimia yang mengintegrasikan analisis unsur oksida utama dan unsur tanah jarang (UTJ), pelapukan purba, serta indeks kematangan sedimen, digunakan untuk mengidentifikasi batuan sumber sedimen. Unsur oksida utama diukur dengan menggunakan fluoresensi sinar-X (XRF), sedangkan konsentrasi UTJ ditentukan dengan menggunakan ICP-OES dan ICP-MS. Diagram diskriminasi geokimia, menunjukkan bahwa sedimen dasar laut sebagian besar berasal dari batuan beku intermediet hingga felsik dengan kematangan komposisi yang lebih tinggi, sementara sedimen pantai dipengaruhi oleh batuan vulkanik mafik yang berkomposisi relatif belum matang. Kedua jenis sedimen tersebut menunjukkan pelapukan kimiawi yang lemah (CIA < 70), yang terlihat dari adanya proses alterasi terbatas pada sumber batuan vulkanik muda. Hubungan CIA-ICV menggambarkan kekontrasan transpor sedimen dan*

proses pengendapan pada lingkungan pesisir dan laut. Studi ini diharapkan dapat memberikan kerangka kerja analisis provenans dengan menggunakan data geokimia dan mendukung pengembangan wawasan dalam kegiatan eksplorasi mineral kelautan di Perairan Limau pada masa yang akan datang.

Kata Kunci: *Geokimia sedimen laut, analisis provenans, pelapukan kimia, Perairan Limau*

INTRODUCTION

Limau Waters is a shallow marine area in Tanggamus, South Lampung, that hosts potential occurrences of economic minerals such as gold placer deposits (Darlan, 1997; Sukardjono et al., 1990) and zeolite (Muksin & Heditama, 2016). The presence of these minerals in southern Lampung is associated with the Sumatran fault system, particularly the segment within the Kotaagung and its surroundings. Geologically, the area is composed of the Oligo–Miocene volcanic rocks, dominated by andesite and dacite. Primary gold deposits occur as quartz vein orebodies formed by low-sulphidation epithermal Au–Ag mineralization, while secondary deposits are represented by ancient placer deposits (Crow & Van Leeuwen, 2005).

According to Irzon (2020), lithological units distributed along the coastal regions of Kotaagung and Limau are predominantly Quaternary and Tertiary volcanic rocks. The Tertiary units consist of basaltic trachyandesite, trachyandesite, dacite, and rhyolite, whereas the Quaternary volcanic rocks comprise basalt, basaltic andesite, and andesite. Despite this geological framework, no specific studies have yet focused on the provenance of seabed and coastal sediments in the Limau Waters area.

This study therefore aims to identify the source rocks, paleoweathering signatures, and sediment maturity of both seabed and coastal sediments through a geochemical approach. The analytical framework integrates major oxide geochemistry (Cruz et al., 2021; Cullers, 1994; Roser & Korsch, 1988) and rare earth element (REE) concentrations (Cruz et al., 2021; Ekoa Bessa et al., 2021; Sousa et al., 2022; McLennan, 1989). A clearer understanding of sediment provenance would provide valuable insights for future exploration of mineral-bearing source rocks in Limau Waters and the surrounding region.

Physiography and Geological Setting of Lampung Area and Surroundings

Sumatera Island was formed from the meeting of three terranes, namely: Sibumasu, West Sumatra, and Woyla (Barber & Crow, 2005; Metcalfe, 2017). The Sibumasu was a part of Gondwana that moved relatively northward in the Early Permian which then collided with the West Sumatra in the Late Permian (Barber & Crow, 2005). There was a change in subduction from Cathaysia to the Sibumasu due to the subduction of the Mesotethys Ocean Plate which Advokaat et al. (2018) called the Ngalau Ocean Plate. The formation of the Mid Oceanic Ridge (MOR) on the Ngalau Ocean Plate which was tilted towards subduction caused the formation of a right-hand horizontal fault which caused the West Sumatra to move relatively westward so that the Sibumasu was sandwiched between two terranes associated with Cathaysia (Barber & Crow, 2005).

The stratigraphic framework of the study area generally comprises Tertiary and Quaternary rock units (Amin, 1993). From oldest to youngest, the succession begins with the Hulusimpang Volcanic Rocks Formation (Tomh) of Oligocene–Early Miocene age, characterized by volcanic breccia, lava flows, and andesitic–basaltic tuff. Much of this unit exhibits hydrothermal alteration, which has resulted in the development of quartz veins hosting sulfide minerals. Conformably overlying this formation is the Seblat Sedimentary Rocks Formation (Toms), dated to the Oligocene–Middle Miocene. Its lithology consists of interbedded mudstone, sandstone, tuffaceous sandstone, shale, and calcareous siltstone, locally accompanied by thin limestone beds or nodules.

The stratigraphy continues upward with the Bal Volcanic Rocks Formation (Tmba) of Middle–Late Miocene age, which lies conformably above both the Hulusimpang and Seblat Formations. This unit is dominated by dacitic volcanic breccia, dacite tuff, and sandstone. Emplaced within these older sequences is the Tertiary Granite/Dacite Intrusive Complex (Tmgr/Tmda), representing a Middle Miocene magmatic event. The intrusion consists of felsic plutonic rocks that cut across the Hulusimpang, Seblat, and Bal Formations. Overlying these units is the Simpangaur Sedimentary Rocks Formation (Tmps) of Pliocene age, comprising tuffaceous sandstone, tuffaceous siltstone, tuff, and polymict conglomerate. This formation also contains molluscan macrofossils, shell fragments, and locally

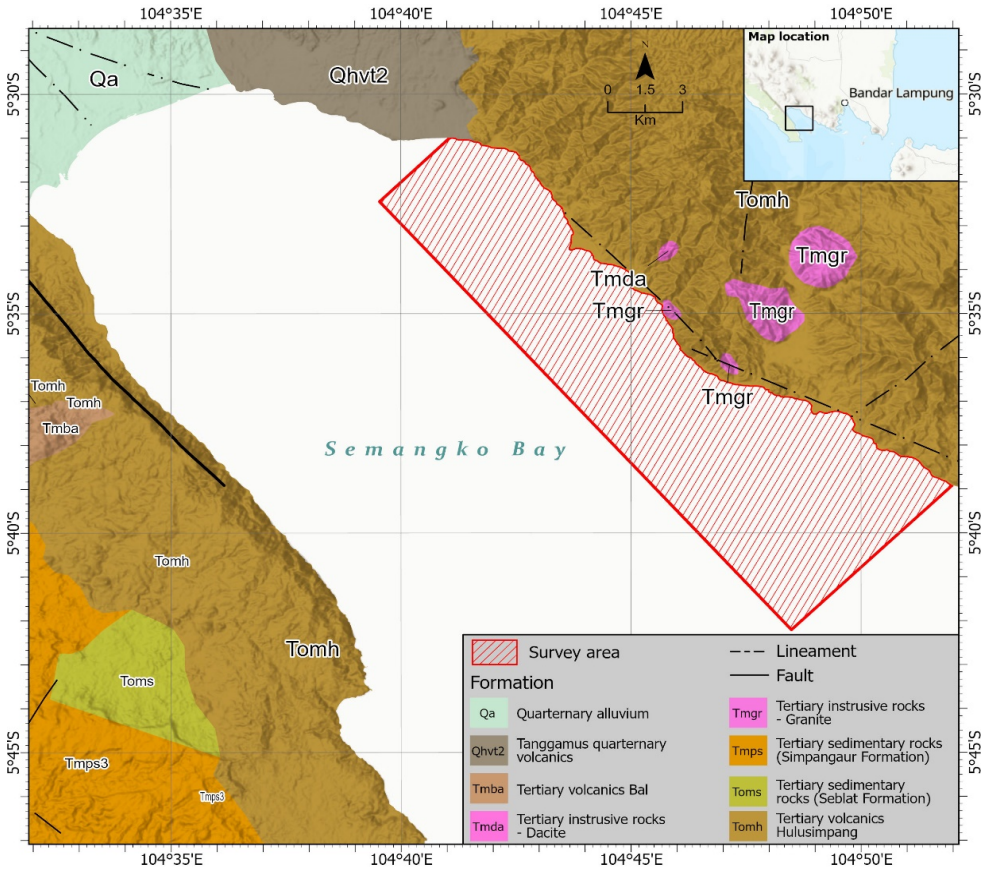

Figure 1. Tanggamus and surroundings area geological map (Modified from Amin, 1993)

thin lignite layers, indicating deposition in a shallow-marine to deltaic environment.

The youngest volcanic unit in the area is the Tanggamus Quaternary Volcanic Rocks (Qhvt), deposited during the Pleistocene–Holocene and sourced from Mount Tanggamus. It consists of volcanic breccia, lava flows, and andesite–basalt tuff. The stratigraphic sequence is capped by Quaternary Alluvium (Qa), an unconsolidated Holocene deposit composed of boulders, gravel, pebbles, sand, silt, clay, and mud, typically accumulated within estuarine and active fluvial environments under ongoing modern sedimentation.

METHODS

Sampling method

The sediment sampling was divided into two parts, namely: coastal sediment sampling and seabed sediment sampling. Seabed sediment sampling used a survey vehicle of a local fishing boat equipped with supporting equipment in the form of a set of navigation tools, winch and grab samplers. The location of the sample points had been determined at intervals of around 1-4 km with a maximum seabed depth of about 80 meters. The seabed depth levels below could not be taken due to limited sampling equipment. Meanwhile, coastal sediment samples were taken by hand auger sediment sampler (Figure 2). The location of the sample points had been determined at intervals of about 1-3 km by considering changes in coastal sediment characteristics in the field.

Sampling activities for collecting seabed samples were carried out by heading towards the planned sampling points, then taken using a grab sampler and winch 2-6 times. After the sediment sample had been successfully taken, the sample was then put into an airtight sample plastic and labeled. A total of 44 samples was taken, consisting of fine fraction sediment (~60–70%) and sand fraction sediment (~30–40%).

Coastal sediment sampling activities were carried out by heading toward the predetermined sampling points. The coastal sediments were collected using a hand auger sampler, taken from approximately 10 cm below the beach surface, and immediately placed into airtight plastic bags, which were then labeled for laboratory analysis. A total of 18 coastal sediment samples were collected, predominantly composed of the sand fraction. Figure 3 shows the 62 sediment samples (both marine and

Figure 2. Coastal sediment sampling with hand auger

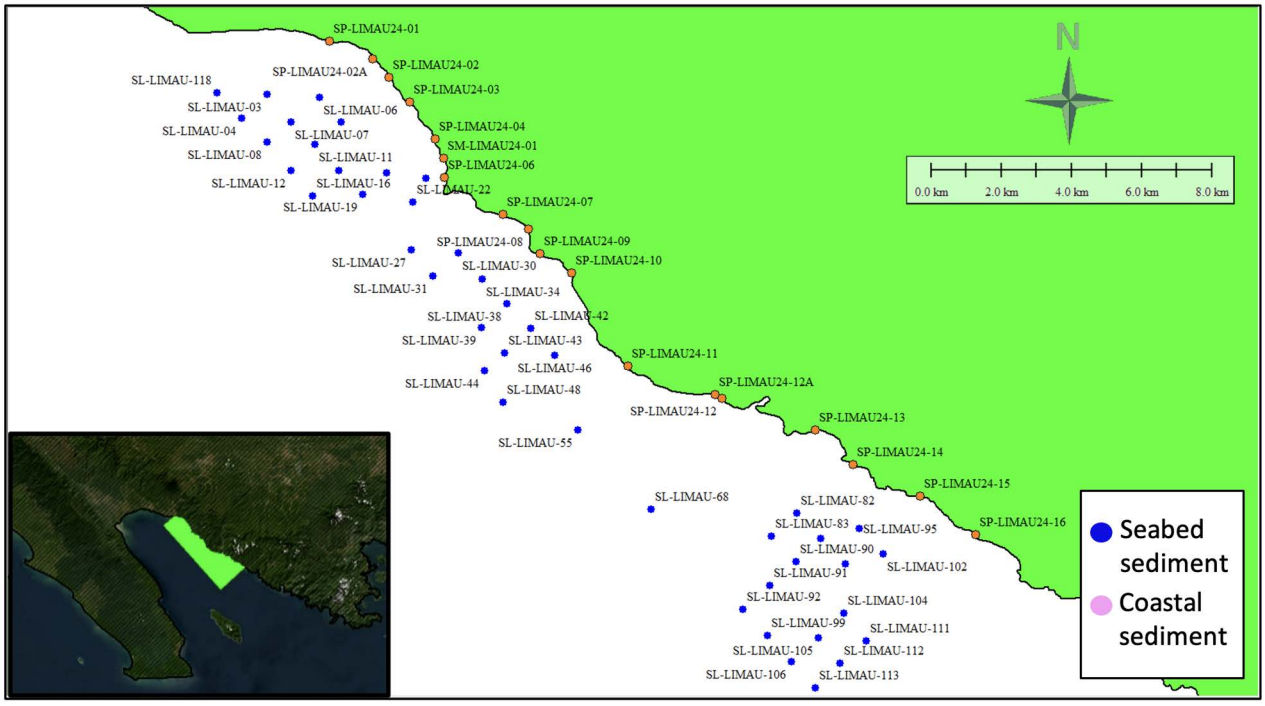

Figure 3. Seabed and coastal sediment sample location map

coastal sediments) collected for geochemical analysis using ICP–OES+MS and XRF.

Analytical method

Geochemical analytical methods used for this research were run by ICP-OES+MS and XRF devices. The ICP-OES+MS method was used to determine the REE content, while XRF was used to determine the content of the major oxide elements. The REE content were normalized to chondrite values. Several geochemical ratios and anomalies were calculated to evaluate REE fractionation and anomalies, including Eu, Ce, and REE enrichment ratios.

The europium anomaly (Eu/Eu*) was calculated using the equation:

$$Eu/Eu* = \frac{Eu(Sample)/Eu\ (Chondrite)}{\sqrt{\frac{Sm(Sample)}{Sm(Chondrite)}\ X\ \frac{Gd\ (Sample)}{Gd\ (Chondrite)}}} \quad (1)$$

The cerium anomaly (Ce/Ce*) was determined by:

$$Ce/Ce^* = \frac{Ce(Sample)/Ce\ (Chondrite)}{\sqrt{\frac{La\ (Sample)}{La\ (Chondrite)}\ X\ \frac{Pr\ (Sample)}{Pr\ (Chondrite)}}} \quad (2)$$

REE fractionation between light and heavy groups was expressed using normalized ratios:

$$(La/Sm)_N = \frac{La(Sample)/La\ (Chondrite)}{Sm(Sample)/Sm\ (Chondrite)} \quad (3)$$

$$(Gd/Yb)_N = \frac{Gd(Sample)/Gd\ (Chondrite)}{Yb(Sample)/Yb\ (Chondrite)} \quad (4)$$

Additionally, for describing the overall REE pattern slope we used:

$$(La/Yb)_N = \frac{La(Sample)/La\ (Chondrite)}{Yb(Sample)/Yb\ (Chondrite)} \quad (5)$$

The discriminant functions (Roser & Korsch, 1988) used to identify the source rock composition are calculated using the following equations:

$$F1 = (-1.773 \times TiO_2)+(0.607 \times Al_2O_3)+ (0.76\times Fe_2O_3) + (-1.5 \times MgO) + (0.616 \times CaO) + (0.509 \times Na_2O) + (-1.22 \times K_2O)+(-9.09). \quad (6)$$

$$F2 = (0.445 \times TiO_2) + (0.07\times Al_2O_3)+(-0.25 \times Fe_2O_3)+(-1.142 \times MgO) + (0.438 \times CaO) +(1.475 \times Na_2O) + (1.426 \times K_2O) + (-6.861) \quad (7)$$

These discriminant functions (F_1 and F_2) are used to classify the provenance of sedimentary rocks into mafic, intermediate, felsic, or quartzose sedimentary source types based on major oxide compositions. Meanwhile, the major oxide element contents are plotted into the discrimination function (Roser & Korsch, 1988) to determine the source rock, and the TiO_2 versus Zr content is used to determine the tectonic setting of the source rock formation. From all of these identification functions, information can be obtained regarding the type of source rock and its formation process.

To further evaluate the degree of chemical weathering and sediment maturity, several weathering indices were calculated, including the Chemical Index of Alteration (CIA), Plagioclase Index of Alteration (PIA), Chemical Index of Weathering (CIW), and Index of Compositional Variability (ICV), as defined by the following equations:

$$CIA\ (\%) = \frac{Al_2O_3}{(Al_2O_3+CaO^*+Na_2O+K_2O)}\ X\ 100 \text{ (Nesbit and Young, 1984)} \quad (8)$$

$$PIA\ (\%) = \frac{Al_2O_3-K_2O}{(Al_2O_3+CaO^*+Na_2O-K_2O)}\ X\ 100 \text{ (Fedo et al., 1995)} \quad (9)$$

$$CIW\ (\%) = \frac{Al_2O_3}{(Al_2O_3+CaO^*+Na_2O)}\ X\ 100 \text{ (Harnois, 1988)} \quad (10)$$

$$ICV\ (\%) = \frac{Fe_2O_3+K_2O+CaO^*+Na_2O+MgO+MnO+TiO_2}{Al_2O_3}\ X\ 100 \text{ (Cox et al., 1995)} \quad (11)$$

These indices provide quantitative measures of chemical weathering intensity and sediment compositional maturity, reflecting the paleoenvironmental and provenance conditions of the studied sediments.

RESULTS

Rare Earth Elements Contents

Results indicate that the total rare earth element (REE) concentrations in the samples range from 38 to 88.93 ppm. For geochemical classification, LREE (light rare earth elements) are defined as the light lanthanides from La to Sm, MREE (middle rare earth elements) comprise the intermediate lanthanides from Eu to Dy, and HREE (heavy rare earth elements) correspond to the heavier lanthanides from Ho to Lu.

The LREE/HREE ratios, which range from 4.41 to 8.79, demonstrate a clear enrichment of LREE relative to HREE. This is further supported by the relatively high La/Yb ratios (Table 1), ranging from 4.9 to 12.59, indicating pronounced LREE enrichment across the samples. Meanwhile, the LREE/MREE ratios, represented by La/Sm, range from 2.13 to 3.58, suggesting fractionation that favors LREE over MREE. In addition, the MREE/HREE ratios, represented by Gd/Yb, range from 1.93 to 2.57, reflecting an enrichment of MREE relative to HREE.

All the REE contents were normalized with chondrite values of McDonough and Sun (1995) to eliminate the natural fractionation patterns and to identify geological processes. Based on the chondrite-normalized REE data, different trend patterns are observed between seabed sediments (Figure 4a) and coastal sediments (Figure 4b).

Seabed sediments exhibit a positive Ce anomaly, with values ranging from 1.14 to 1.27. Conversely, the Ce anomaly in coastal sediments is typically negative or near one, ranging from 0.91 to 1.00. Positive Ce anomalies in seabed sediments may reflect stable open-marine depositional conditions with limited detrital input (Anenburg & Liu, 2024; Zhang & Shields, 2022).

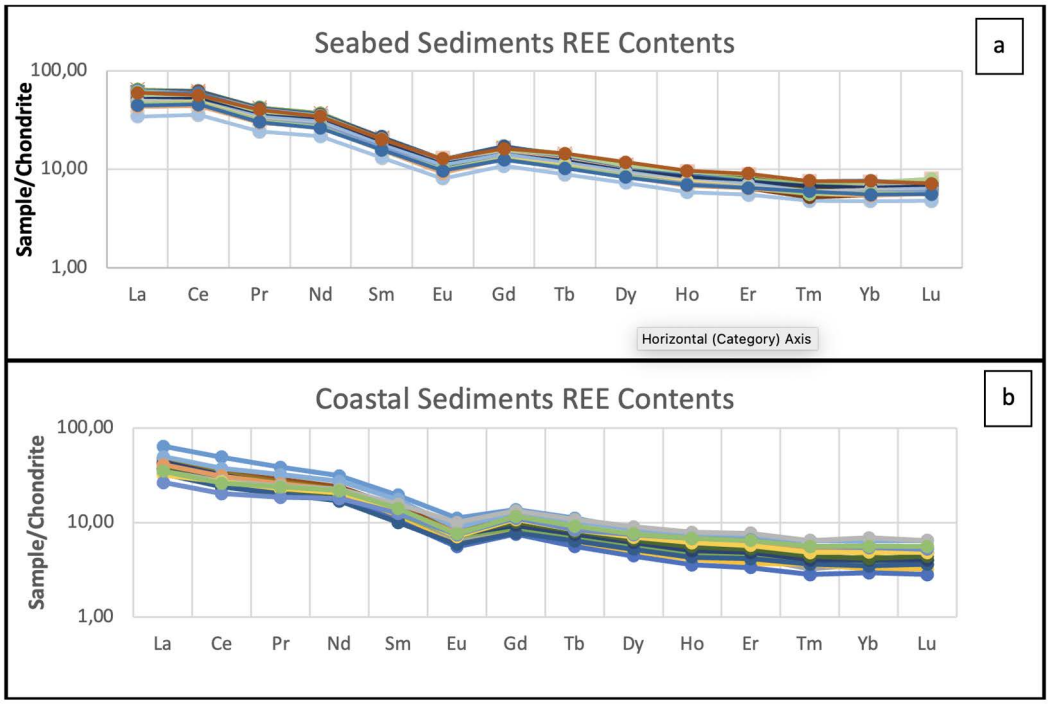

Figure 4. REE contents of the (a) Seabed sediments and (b) Coastal sediments

However, it is also recognized that in some settings positive Ce anomalies can arise from diagenetic processes, particularly the reductive dissolution of Fe–Mn (oxyhydr)oxides under suboxic to anoxic conditions (Bau et al., 1997). Coastal sediments, on the other hand, reflect more variable REE patterns with weaker or negative Ce anomalies, likely driven by dynamic depositional processes, fluctuating redox conditions, and greater input of detrital material from continental sources (Zhang et al., 2024; Sousa et al., 2022). Despite local differences in REE patterns between seabed and coastal samples, a pronounced negative europium anomaly (Eu/Eu < 1) was a pervasive feature across all analyzed samples. Such consistent Eu depletion is widely reported in modern sedimentary studies and is commonly attributed to provenance effects (e.g., plagioclase fractionation in source rocks) and selective mineral sorting during transport and deposition (Sousa et al., 2022; Ramos-Vázquez et al., 2021; Ruban et al., 2024; Li et al., 2024; Anenburg & Liu, 2024).

Major Oxide Elements Contents

Analysis of the major elements was performed on the sediment samples (seabed, n = 44; coastal, n = 18), presented in Table 2. The analysis reveals that SiO_2 is the dominant oxide, with concentrations ranging from 19.4% to 74.43%. Fe_2O_3 concentrations varied significantly, ranging from 4.09% to 18.66%, while Al_2O_3 was present between 3.38% and 15.53%. Based on the exploration report conducted by BBSPGL (2024), the analyzed samples are predominantly composed of clay minerals, which supports the interpretation that the presence of these minerals controls the variability in Al_2O_3 content. This observation is consistent with the well-established understanding that aluminosilicate clay minerals such as kaolinite, illite, and smectite serve as the primary hosts of aluminum in sedimentary environments, making Al_2O_3 a reliable indicator of clay abundance (Guan et al., 2023). Minor element oxides also displayed notable ranges: TiO_2 (0.44% to 2.19%), K_2O (0.29% to 2.78%), MgO (0.98% to 5.66%), MnO (0.04% to 0.28%), Na_2O (1% to 5.77%), and P_2O_5 (0.061% to 0.182%). Loss of Ignition (LOI) values spanned from 1.62% to 28%. Eventually, both Cr_2O_3 and S were consistently detected at trace levels, measuring less than 0.035%.

Based on the results of the Harker diagram plotting of the main oxide elements against Al_2O_3 (Figure 5), both negative and positive. These relationships indicate that some oxides decrease with increasing Al_2O_3, while others increase, reflecting different geochemical behavior during sediment formation. The strongest correlation is observed between Na_2O and Al_2O_3 (r =0.883), suggesting a strong positive association, whereas the weakest is between SiO_2 and Al_2O_3, showing a weak negative association (r = -0.006). Seabed sediments cluster tightly, indicating more stable environmental conditions and a relatively homogeneous source. In

Table 1. Chondrite-normalized REE contents and calculated parameters with following equations (1)–(5)

	SAMPLE ID																													
	SLL-003	SLL-004	SLL-006	SLL-007	SLL-008	SLL-010	SLL-011	SLL-012	SLL-015	SLL-016	SLL-018	SLL-019	SLL-021	SLL-022	SLL-027	SLL-030	SLL-031	SLL-034	SLL-038	SLL-039	SLL-042	SLL-043	SLL-044	SLL-046	SLL-048	SLL-055	SLL-068	SLL-082	SLL-083	SLL-089	SLL-090
La	13,2	14,3	14,5	14,7	14,1	15,4	15	14,7	14,1	11,8	14,4	14,1	14,8	13,3	13	13,7	12,8	14,4	14	12,3	13,2	11,8	12,9	12,7	8,17	13,2	12,1	12	12,5	13,6	11,7
Ce	32	36,3	34,7	36,8	36,1	38,3	38,4	37,6	36,3	30,6	36,8	36,7	36,1	33,2	33,6	34,4	33,4	36	36,3	32,2	34,5	30,7	34	33	21,9	34,1	31,2	31,2	32,9	34,7	30,7
Pr	3,63	3,83	3,84	3,93	3,74	4,11	4	3,92	3,77	3,18	3,87	3,77	3,9	3,56	3,56	3,63	3,47	3,78	3,75	3,34	3,59	3,2	3,52	3,45	2,33	3,56	3,29	3,27	3,44	3,69	3,2
Nd	15,3	15,9	15,8	16,2	15,7	17	16,5	16,2	15,7	13,3	15,9	15,6	16,1	14,6	14,8	15,1	14,5	15,9	15,5	14,2	14,9	13,5	14,6	14,5	9,91	14,8	13,7	13,9	14,5	15,7	13,4
Sm	3,05	3,19	3,06	3,17	3,13	3,22	3,27	3,16	3	2,66	3,03	3,06	3,11	2,85	2,88	3,01	2,84	3,07	3,05	2,75	2,86	2,63	2,84	2,92	2,01	2,88	2,65	2,77	2,79	3,02	2,66
Eu	0,71	0,7	0,69	0,74	0,71	0,73	0,74	0,71	0,71	0,58	0,71	0,69	0,7	0,63	0,63	0,68	0,63	0,71	0,7	0,61	0,65	0,58	0,65	0,65	0,47	0,67	0,61	0,64	0,66	0,75	0,6
Gd	3,31	3,3	3,23	3,27	3,22	3,33	3,42	3,26	3,13	2,66	3,18	3,14	3,12	2,92	2,93	3	2,77	3,16	3,18	2,78	2,95	2,69	2,85	2,86	2,16	2,92	2,79	2,81	2,88	3,15	2,62
Tb	0,5	0,51	0,5	0,51	0,5	0,52	0,5	0,51	0,48	0,41	0,49	0,49	0,48	0,44	0,46	0,46	0,45	0,48	0,48	0,42	0,44	0,41	0,45	0,44	0,32	0,45	0,41	0,42	0,43	0,51	0,41
Dy	2,87	2,86	2,77	2,91	2,73	2,86	2,88	2,86	2,69	2,31	2,75	2,7	2,6	2,5	2,58	2,58	2,46	2,71	2,65	2,45	2,46	2,29	2,53	2,48	1,86	2,51	2,37	2,4	2,46	2,77	2,34
Ho	0,53	0,52	0,51	0,53	0,52	0,51	0,52	0,52	0,49	0,42	0,5	0,49	0,48	0,45	0,47	0,47	0,44	0,5	0,49	0,44	0,45	0,41	0,46	0,45	0,33	0,46	0,43	0,43	0,45	0,53	0,44
Er	1,43	1,40	1,34	1,43	1,39	1,40	1,38	1,41	1,31	1,15	1,31	1,33	1,30	1,22	1,25	1,29	1,21	1,31	1,26	1,12	1,21	1,12	1,23	1,18	0,91	1,24	1,14	1,16	1,22	1,47	1,15
Tm	0,19	0,18	0,17	0,18	0,18	0,17	0,18	0,18	0,17	0,15	0,17	0,17	0,16	0,15	0,17	0,16	0,15	0,18	0,17	0,16	0,16	0,14	0,16	0,16	0,12	0,16	0,15	0,16	0,16	0,19	0,15
Yb	1,29	1,26	1,17	1,22	1,26	1,20	1,24	1,23	1,11	1,01	1,16	1,16	1,08	1,07	1,06	1,09	1,04	1,15	1,11	1,03	1,11	0,98	1,09	1,13	0,80	1,14	1,01	1,09	1,12	1,25	1,03
Lu	0,18	0,18	0,17	0,19	0,18	0,18	0,18	0,18	0,17	0,15	0,17	0,17	0,16	0,16	0,16	0,16	0,16	0,17	0,17	0,15	0,16	0,15	0,16	0,16	0,12	0,17	0,16	0,16	0,17	0,20	0,16
LREE	67,89	74,22	72,59	75,54	73,48	78,76	77,91	76,29	73,58	62,12	74,71	73,92	74,71	68,14	68,47	70,52	67,64	73,86	73,30	65,40	69,70	62,41	68,51	67,22	44,79	69,21	63,55	63,78	66,79	71,46	62,26
HREE	10,30	10,21	9,86	10,24	9,98	10,17	10,30	10,15	9,55	8,26	9,73	9,65	9,38	8,91	9,08	9,21	8,68	9,66	9,51	8,55	8,94	8,19	8,93	8,86	6,62	9,05	8,46	8,63	8,89	10,07	8,30
ΣREE	78,19	84,43	82,45	85,78	83,46	88,93	88,21	86,44	83,13	70,38	84,44	83,57	84,09	77,05	77,55	79,73	76,32	83,52	82,81	73,95	78,64	70,60	77,44	76,08	51,41	78,26	72,01	72,41	75,68	81,53	70,56
LREE/HREE	6,59	7,27	7,36	7,38	7,36	7,74	7,56	7,52	7,70	7,52	7,68	7,66	7,96	7,65	7,54	7,66	7,79	7,65	7,71	7,65	7,80	7,62	7,67	7,59	6,77	7,65	7,51	7,39	7,51	7,10	7,50
Eu/Eu*	0,67	0,65	0,66	0,69	0,67	0,67	0,67	0,67	0,70	0,66	0,69	0,67	0,68	0,66	0,65	0,68	0,68	0,69	0,68	0,66	0,67	0,66	0,69	0,68	0,68	0,70	0,67	0,69	0,70	0,73	0,68
Ce/Ce*	1,14	1,21	1,14	1,19	1,22	1,18	1,22	1,22	1,23	1,23	1,21	1,24	1,17	1,19	1,22	1,20	1,23	1,20	1,23	1,24	1,23	1,23	1,24	1,23	1,24	1,22	1,22	1,23	1,23	1,21	1,23
$(La/Yb)_N$	7,25	8,05	8,79	8,54	7,93	9,10	8,57	8,47	9,00	8,28	8,80	8,62	9,71	8,81	8,69	8,91	8,72	8,88	8,94	8,47	8,43	8,54	8,39	7,97	7,24	8,21	8,49	7,80	7,91	7,71	8,05
$(La/Sm)_N$	2,79	2,89	3,06	2,99	2,91	3,09	2,96	3,00	3,03	2,86	3,07	2,97	3,07	3,01	2,91	2,94	2,91	3,03	2,96	2,89	2,98	2,90	2,93	2,81	2,62	2,96	2,95	2,80	2,89	2,91	2,84
$(Gd/Yb)_N$	2,17	2,21	2,33	2,26	2,16	2,34	2,33	2,24	2,38	2,22	2,31	2,29	2,44	2,30	2,33	2,32	2,25	2,32	2,42	2,28	2,24	2,32	2,21	2,14	2,28	2,16	2,33	2,18	2,17	2,13	2,15

LREE (La, Ce, Pr, Nd, Sm, and Eu) ; HREE (Gd, Tb, Dy Ho, Er, Tm, and Lu)

(*Continued*)

	SAMPLE ID																													
	SLL-091	SLL-092	SLL-095	SLL-096	SLL-099	SLL-102	SLL-104	SLL-105	SLL-106	SLL-111	SLL-112	SLL-113	SLL-118	SML-01	SPL-01	SPL-02	SPL-02A	SPL-03	SPL-04	SPL-06	SPL-07	SPL-08	SPL-09	SPL-10	SPL-11	SPL-12	SPL-12A	SPL-13	SPL-14	SPL-15	SPL-16
La	10,3	10,7	12	12,3	11,5	11,8	10,2	11,8	11	11	11	10,6	14,3	15,1	10,2	9,23	8,91	8,7	9,96	7,73	11,2	9,97	11,3	10,3	8,7	11,7	9,63	8,22	7,53	6,29	8,24
Ce	27,5	28,2	30,8	32,2	30,2	30,2	27,1	29,6	29,9	28,8	28,9	28,1	34,7	30	19,3	17,2	16,7	15,9	19,4	14,5	20,5	18,8	20,4	19,5	17,3	22,9	18,9	16,8	16,5	12,4	15,9
Pr	2,87	2,97	3,34	3,41	3,15	3,28	2,87	3,1	3,06	3,01	3	2,91	3,86	3,68	2,49	2,17	2,14	2,1	2,34	1,92	2,73	2,45	2,58	2,36	2,16	3,07	2,46	2,33	2,17	1,78	2,28
Nd	12,3	12,6	13,9	14,5	13,2	13,9	12,2	13,3	12,7	12,8	12,3	12	15,8	14,3	9,83	8,54	8,47	8,22	9,17	7,73	10,9	9,82	10,2	9,4	8,96	12,4	10,1	10,3	9,31	8,17	9,89
Sm	2,5	2,46	2,71	2,88	2,63	2,73	2,38	2,56	2,47	2,57	2,4	2,41	3,09	2,97	2,06	1,71	1,69	1,61	1,89	1,52	2,23	2,03	2,04	1,96	1,94	2,67	2,08	2,39	2,02	1,91	2,15
Eu	0,56	0,56	0,62	0,66	0,61	0,64	0,53	0,58	0,57	0,58	0,58	0,56	0,74	0,64	0,4	0,37	0,34	0,32	0,41	0,34	0,49	0,43	0,48	0,43	0,43	0,51	0,45	0,58	0,41	0,43	0,44
Gd	2,51	2,53	2,75	2,85	2,73	2,85	2,52	2,6	2,59	2,48	2,52	2,5	3,25	2,74	1,9	1,59	1,56	1,49	1,73	1,54	2,15	1,89	1,98	1,86	2	2,56	2,13	2,63	2,15	2,21	2,31
Tb	0,38	0,39	0,43	0,44	0,42	0,42	0,38	0,4	0,39	0,38	0,38	0,37	0,52	0,4	0,26	0,24	0,22	0,2	0,26	0,23	0,32	0,29	0,3	0,27	0,29	0,37	0,3	0,39	0,3	0,3	0,33
Dy	2,16	2,2	2,41	2,48	2,37	2,41	2,15	2,31	2,18	2,19	2,19	2,11	3	2,15	1,43	1,36	1,24	1,12	1,45	1,32	1,8	1,62	1,7	1,56	1,65	2,17	1,81	2,28	1,77	1,88	1,92
Ho	0,4	0,4	0,45	0,47	0,43	0,43	0,38	0,43	0,42	0,4	0,39	0,39	0,54	0,41	0,27	0,25	0,23	0,2	0,26	0,24	0,33	0,31	0,31	0,28	0,31	0,41	0,36	0,44	0,34	0,38	0,38
Er	1,06	1,09	1,22	1,24	1,12	1,18	1,05	1,12	1,09	1,09	1,09	1,07	1,50	1,11	0,72	0,69	0,61	0,55	0,71	0,68	0,92	0,81	0,83	0,79	0,86	1,15	0,96	1,26	0,94	1,07	1,06
Tm	0,13	0,14	0,16	0,17	0,15	0,15	0,14	0,15	0,14	0,14	0,14	0,15	0,19	0,14	0,09	0,08	0,09	0,07	0,10	0,09	0,12	0,11	0,10	0,10	0,11	0,16	0,13	0,16	0,12	0,14	0,14
Yb	0,92	0,95	1,08	1,10	1,03	1,04	0,91	1,05	0,95	0,98	0,97	0,93	1,28	0,95	0,64	0,61	0,54	0,49	0,64	0,58	0,85	0,70	0,73	0,67	0,70	1,08	0,88	1,15	0,81	0,91	0,94
Lu	0,14	0,15	0,16	0,17	0,16	0,16	0,14	0,15	0,15	0,15	0,14	0,14	0,18	0,13	0,09	0,09	0,08	0,07	0,09	0,09	0,12	0,10	0,10	0,10	0,11	0,16	0,14	0,16	0,12	0,13	0,14
LREE	56,03	57,49	63,37	65,95	61,29	62,55	55,28	60,94	59,70	58,76	58,18	56,58	72,49	66,69	44,28	39,22	38,25	36,85	43,17	33,74	48,05	43,50	47,00	43,95	39,49	53,25	43,62	40,62	37,94	30,98	38,90
HREE	7,70	7,85	8,66	8,92	8,41	8,64	7,67	8,21	7,91	7,81	7,82	7,66	10,46	8,03	5,40	4,91	4,57	4,19	5,24	4,77	6,61	5,83	6,05	5,63	6,03	8,06	6,71	8,47	6,55	7,02	7,22
ΣREE	63,73	65,34	72,03	74,87	69,70	71,19	62,95	69,15	67,61	66,57	66,00	64,24	82,95	74,72	49,68	44,13	42,82	41,04	48,41	38,51	54,66	49,33	53,05	49,58	45,52	61,31	50,33	49,09	44,49	38,00	46,12
LREE/HREE	7,28	7,32	7,32	7,39	7,29	7,24	7,21	7,42	7,55	7,52	7,44	7,39	6,93	8,31	8,20	7,99	8,37	8,79	8,24	7,07	7,27	7,46	7,77	7,81	6,55	6,61	6,50	4,80	5,79	4,41	5,39
Eu/Eu*	0,67	0,68	0,68	0,69	0,68	0,69	0,65	0,68	0,68	0,69	0,71	0,69	0,70	0,67	0,61	0,68	0,63	0,62	0,68	0,67	0,67	0,66	0,72	0,68	0,66	0,59	0,64	0,70	0,59	0,63	0,59
Ce/Ce*	1,24	1,23	1,20	1,22	1,23	1,19	1,23	1,20	1,27	1,23	1,24	1,24	1,15	0,99	0,94	0,95	0,94	0,92	0,99	0,93	0,91	0,94	0,93	0,97	0,98	0,94	0,96	0,94	1,00	0,91	0,90
$(La/Yb)_N$	7,94	7,98	7,88	7,93	7,91	8,04	7,95	7,97	8,21	7,96	8,04	8,08	7,92	11,27	11,30	10,73	11,70	12,59	11,03	9,45	9,34	10,10	10,97	10,90	8,81	7,68	7,76	5,07	6,59	4,90	6,21
$(La/Sm)_N$	2,66	2,81	2,86	2,76	2,82	2,79	2,77	2,98	2,88	2,76	2,96	2,84	2,99	3,28	3,20	3,48	3,40	3,49	3,40	3,28	3,24	3,17	3,58	3,39	2,90	2,83	2,99	2,22	2,41	2,13	2,47
$(Gd/Yb)_N$	2,30	2,25	2,15	2,19	2,24	2,31	2,34	2,09	2,30	2,14	2,19	2,27	2,14	2,43	2,51	2,20	2,44	2,57	2,28	2,24	2,14	2,28	2,29	2,34	2,41	2,00	2,04	1,93	2,24	2,05	2,07

LREE (La, Ce, Pr, Nd, Sm, and Eu) ; HREE (Gd, Tb, Dy Ho, Er, Tm, and Lu)

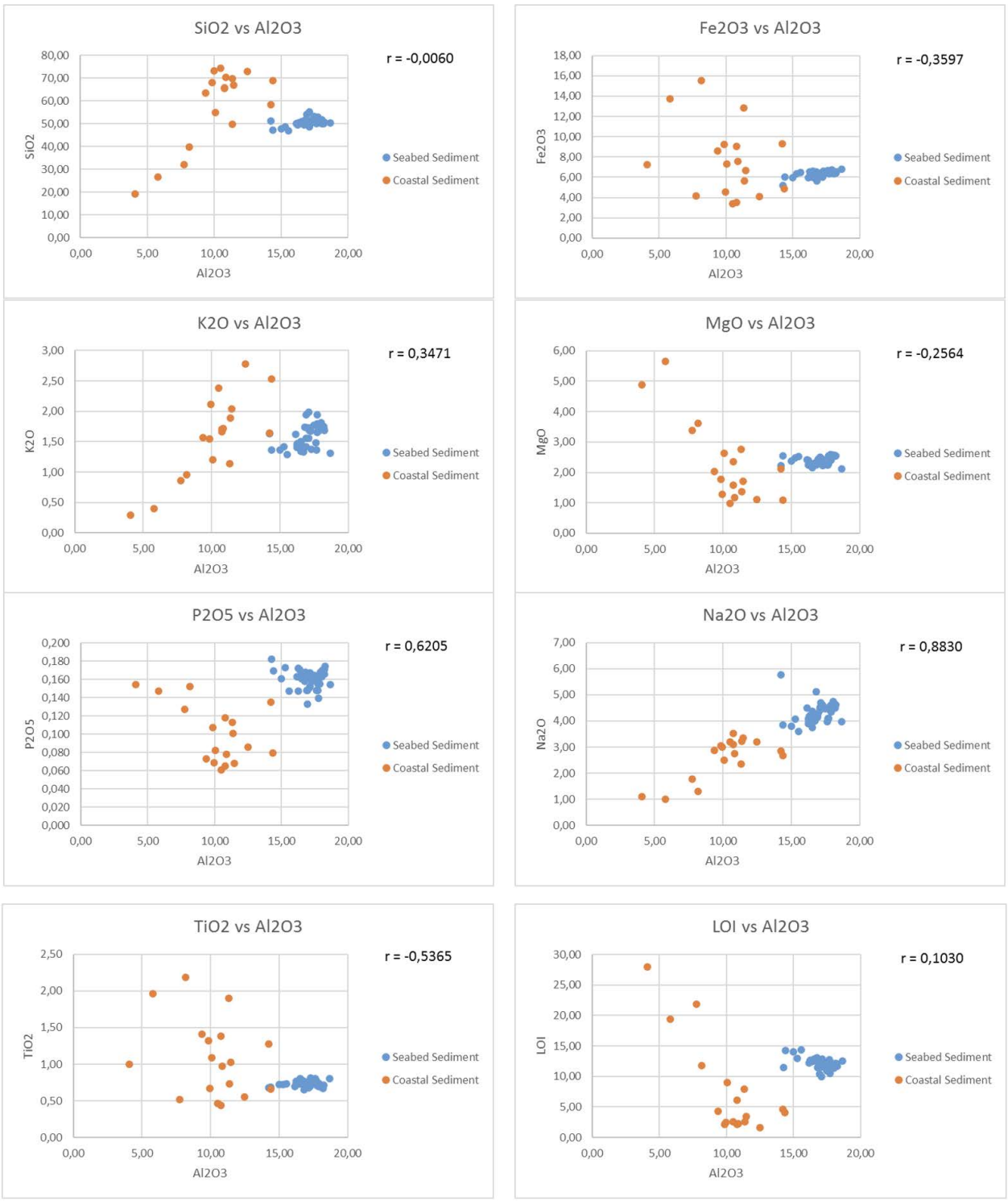

Figure 5. Harker diagram of Al_2O_3 vs selected major oxide elements

Table 2. Major oxides compositions (%) and some elemental ratios along with calculated weathering indices according to equations (8)-(11)

	SAMPLE ID																														
	SLL-003	SLL-004	SLL-006	SLL-007	SLL-008	SLL-010	SLL-011	SLL-012	SLL-015	SLL-016	SLL-018	SLL-019	SLL-021	SLL-022	SLL-027	SLL-030	SLL-031	SLL-034	SLL-038	SLL-039	SLL-042	SLL-043	SLL-044	SLL-046	SLL-048	SLL-055	SLL-068	SLL-082	SLL-083	SLL-089	SLL-090
SiO2	53,20	50,54	55,28	51,65	50,55	53,03	51,14	50,12	50,14	51,57	50,73	50,18	54,08	51,29	49,84	51,54	51,18	51,71	51,42	50,89	51,40	50,05	48,76	50,81	51,33	50,29	49,56	50,51	46,97	50,41	50,55
Al2O3	17,47	18,26	17,11	18,03	18,21	17,74	17,87	18,19	18,07	16,80	17,71	18,13	16,92	17,13	17,16	16,94	17,21	17,76	17,86	17,24	17,72	16,16	17,12	16,91	14,25	17,62	16,25	17,30	15,55	18,66	16,90
Fe2O3	6,47	6,52	6,23	6,49	6,40	6,35	6,44	6,41	6,36	5,65	6,38	6,40	6,20	6,36	6,18	6,40	6,02	6,46	6,40	6,05	6,39	5,96	6,25	6,33	5,22	6,68	6,57	6,62	6,47	6,81	6,30
TiO2	0,74	0,71	0,75	0,71	0,70	0,72	0,70	0,67	0,69	0,65	0,71	0,70	0,73	0,71	0,68	0,73	0,69	0,75	0,74	0,70	0,77	0,70	0,73	0,75	0,68	0,80	0,77	0,81	0,73	0,80	0,76
CaO	1,95	2,72	1,74	2,44	2,84	2,29	2,91	3,05	2,94	3,77	2,81	3,00	2,83	3,39	3,71	3,55	3,92	2,57	2,85	4,17	2,78	5,35	4,58	4,41	6,07	3,35	5,45	3,85	7,28	3,01	4,86
K2O	1,77	1,69	1,99	1,81	1,72	1,94	1,79	1,75	1,74	1,74	1,79	1,72	1,94	1,73	1,69	1,73	1,72	1,68	1,69	1,68	1,65	1,62	1,56	1,56	1,63	1,48	1,41	1,38	1,29	1,31	1,42
MgO	2,26	2,54	2,29	2,52	2,55	2,51	2,60	2,55	2,57	2,24	2,54	2,56	2,38	2,51	2,45	2,45	2,44	2,42	2,40	2,45	2,28	2,41	2,45	2,35	2,22	2,24	2,39	2,22	2,53	2,12	2,30
MnO	0,10	0,12	0,10	0,12	0,11	0,11	0,12	0,11	0,11	0,10	0,10	0,10	0,08	0,09	0,10	0,09	0,09	0,09	0,09	0,10	0,09	0,10	0,10	0,08	0,11	0,08	0,10	0,08	0,08	0,08	0,09
Na2O	4,47	4,62	4,50	4,60	4,63	4,47	4,60	4,49	4,74	5,11	4,49	4,54	4,26	4,53	4,69	4,29	4,62	4,48	4,41	4,62	4,09	4,51	4,43	4,23	5,77	3,98	3,90	4,59	3,61	3,98	4,14
P2O5	0,16	0,17	0,15	0,16	0,17	0,16	0,16	0,17	0,17	0,17	0,16	0,17	0,13	0,15	0,16	0,15	0,16	0,14	0,16	0,16	0,15	0,16	0,17	0,15	0,18	0,15	0,15	0,16	0,15	0,15	0,16
Cr2O3	0,02	<0,01	<0,01	<0,01	<0,01	<0,01	0,01	<0,01	<0,01	0,02	<0,01	0,01	<0,01	<0,01	<0,01	<0,01	0,01	<0,01	<0,01	<0,01	<0,01	0,01	0,01	<0,01	0,03	<0,01	0,01	<0,01	<0,01	<0,01	0,17
S	0,31	0,28	0,23	0,25	0,31	0,27	0,33	0,34	0,29	0,25	0,27	0,31	0,23	0,26	0,26	0,22	0,25	0,43	0,27	0,26	0,27	0,24	0,24	0,24	0,22	0,24	0,21	0,22	0,20	0,24	0,23
LOI	10,91	11,70	9,93	11,38	12,02	10,53	11,49	12,12	12,14	11,47	11,64	12,16	10,45	11,79	12,54	11,43	11,61	11,56	11,67	11,87	11,48	12,20	12,89	12,05	11,42	12,30	12,61	12,40	14,41	12,53	12,36
Total	99,80	99,90	100,00	100,00	100,00	100,00	100,00	100,00	100,00	99,50	99,30	100,00	100,00	100,00	99,50	99,50	100,00	100,00	100,00	100,00	99,10	99,50	99,30	99,90	99,10	99,20	99,40	100,00	99,30	100,00	100,00
K2O/Na2O	0,40	0,37	0,44	0,39	0,37	0,43	0,39	0,39	0,37	0,34	0,40	0,38	0,46	0,38	0,36	0,40	0,37	0,38	0,38	0,36	0,40	0,36	0,35	0,37	0,28	0,37	0,36	0,30	0,36	0,33	0,34
Al2O3/TiO2	23,61	25,72	22,81	25,39	26,01	24,64	25,53	27,15	26,19	25,85	24,94	25,90	23,18	24,13	25,24	23,21	24,94	23,68	24,14	24,63	23,01	23,09	23,45	22,55	20,96	22,03	21,10	21,36	21,30	23,33	22,24
SiO2/Al2O3	3,05	2,77	3,23	2,86	2,78	2,99	2,86	2,76	2,77	3,07	2,86	2,77	3,20	2,99	2,90	3,04	2,97	2,91	2,88	2,95	2,90	3,10	2,85	3,00	3,60	2,85	3,05	2,92	3,02	2,70	2,99
log (K2O/Na2O)	-0,40	-0,44	-0,35	-0,41	-0,43	-0,36	-0,41	-0,41	-0,44	-0,47	-0,40	-0,42	-0,34	-0,42	-0,44	-0,39	-0,43	-0,43	-0,42	-0,44	-0,39	-0,44	-0,45	-0,43	-0,55	-0,43	-0,44	-0,52	-0,45	-0,48	-0,46
log (Al2O3/TiO2)	1,37	1,41	1,36	1,40	1,42	1,39	1,41	1,43	1,42	1,41	1,40	1,41	1,37	1,38	1,40	1,37	1,40	1,37	1,38	1,39	1,36	1,36	1,37	1,35	1,32	1,34	1,32	1,33	1,33	1,37	1,35
log (SiO2/Al2O3)	0,48	0,44	0,51	0,46	0,44	0,48	0,46	0,44	0,44	0,49	0,46	0,44	0,50	0,48	0,46	0,48	0,47	0,46	0,46	0,47	0,46	0,49	0,45	0,48	0,56	0,46	0,48	0,47	0,48	0,43	0,48
CIA	73,68	74,32	72,5	73,77	74,14	73,46	73,66	74,46	73,6	71,04	73,82	74,33	73,18	73,24	72,9	73,78	73,08	74,25	74,54	73,24	75,53	72,5	74,08	74,49	65,82	76,34	75,37	74,34	76,04	77,91	75,24
PIA	77,84	78,2	77,06	77,91	78,08	77,95	77,76	78,55	77,5	74,67	78	78,33	77,86	77,27	76,74	78	77,03	78,21	78,57	77,11	79,71	76,33	77,84	78,4	68,62	80,22	79,19	77,62	79,8	81,34	78,9
CIW	79,63	79,81	79,18	79,67	79,73	79,87	79,53	80,2	79,22	76,68	79,77	79,97	79,89	79,09	78,54	79,79	78,84	79,86	80,2	78,87	81,25	78,18	79,44	79,99	71,18	81,57	80,65	79,03	81,16	82,42	80,32
ICV	0,905	0,887	0,927	0,901	0,885	0,908	0,909	0,879	0,897	0,922	0,904	0,884	0,921	0,93	0,92	0,926	0,905	0,894	0,881	0,905	0,862	0,947	0,907	0,905	1,097	0,866	0,932	0,908	0,946	0,809	0,888

CaO* is the CaO value that has been corrected based on Mc Lennan (1990)

(*continued*)

	SAMPLE ID																														
	SLL-091	SLL-092	SLL-095	SLL-096	SLL-099	SLL-102	SLL-104	SLL-105	SLL-106	SLL-111	SLL-112	SLL-113	SLL-118	SML-01	SPL-01	SPL-02	SPL-02A	SPL-03	SPL-04	SPL-06	SPL-07	SPL-08	SPL-09	SPL-10	SPL-11	SPL-12	SPL-12A	SPL-13	SPL-14	SPL-15	SPL-16
SiO2	47,13	48,69	49,61	50,18	50,27	50,10	47,92	50,01	50,34	50,51	50,68	50,94	51,38	68,80	72,78	63,52	73,31	74,43	66,87	65,52	65,77	69,87	68,11	70,26	54,98	58,32	49,91	26,76	39,85	19,14	32,05
Al2O3	14,40	15,29	16,74	17,68	16,34	16,52	15,01	16,25	16,28	16,55	16,51	16,53	17,91	14,37	12,49	9,37	9,97	10,50	11,46	10,78	10,77	11,38	9,86	10,87	10,07	14,23	11,34	5,81	8,16	4,09	7,75
Fe2O3	6,03	6,36	6,54	6,58	6,12	6,61	5,97	6,12	6,04	6,28	6,03	5,99	6,73	4,84	4,12	8,59	4,54	3,38	6,67	3,51	9,05	5,61	9,26	7,57	7,32	9,33	12,82	13,71	15,53	7,22	4,17
TiO2	0,69	0,72	0,78	0,79	0,73	0,80	0,72	0,74	0,73	0,75	0,73	0,73	0,73	0,66	0,55	1,41	0,67	0,46	1,03	0,44	1,38	0,73	1,32	0,97	1,09	1,28	1,90	1,96	2,19	1,00	0,52
CaO	9,08	6,76	5,20	4,21	5,48	5,57	7,71	5,30	5,34	4,95	4,67	4,80	2,45	1,05	1,42	5,53	2,61	2,20	3,33	6,91	3,66	3,35	2,90	2,55	11,12	5,46	9,85	24,77	15,52	33,22	26,67
K2O	1,37	1,42	1,33	1,36	1,46	1,34	1,37	1,46	1,47	1,43	1,47	1,50	1,71	2,53	2,78	1,57	2,11	2,38	2,04	1,66	1,71	1,89	1,55	1,72	1,20	1,64	1,14	0,40	0,96	0,29	0,86
MgO	2,54	2,48	2,31	2,24	2,31	2,26	2,38	2,25	2,24	2,23	2,16	2,17	2,42	1,09	1,11	2,03	1,29	0,98	1,72	1,59	2,35	1,37	1,77	1,17	2,63	2,11	2,75	5,66	3,62	4,89	3,39
MnO	0,10	0,10	0,09	0,09	0,09	0,09	0,09	0,09	0,09	0,09	0,09	0,09	0,11	0,07	0,07	0,10	0,06	0,04	0,09	0,07	0,12	0,08	0,12	0,10	0,15	0,13	0,17	0,28	0,23	0,21	0,13
Na2O	3,84	4,07	3,99	4,10	4,20	3,76	3,80	4,07	4,15	4,15	4,38	4,30	4,34	2,68	3,21	2,88	3,00	3,21	3,34	3,52	3,11	3,23	3,05	2,76	2,50	2,84	2,34	1,00	1,30	1,10	1,78
P2O5	0,17	0,17	0,16	0,16	0,17	0,16	0,16	0,16	0,17	0,17	0,16	0,17	0,17	0,08	0,09	0,07	0,07	0,06	0,07	0,07	0,12	0,10	0,11	0,08	0,08	0,14	0,11	0,15	0,15	0,15	0,13
Cr2O3	0,02	0,01	<0,01	<0,01	0,02	<0,01	0,02	<0,01	0,01	0,01	0,01	<0,01	0,02	0,01	0,01	<0,01	0,02	0,01	0,02	0,02	0,02	0,01	0,01	0,01	<0,01	<0,01	<0,01	<0,01	0,02	<0,01	0,02
S	0,18	0,18	0,26	0,22	0,19	0,19	0,19	0,20	0,18	0,20	0,23	0,22	0,27	0,01	<0,002	0,04	0,03	0,03	0,03	0,04	0,02	0,01	0,02	<0,002	0,05	0,03	0,05	0,09	0,07	0,11	0,09
LOI	14,27	13,02	13,04	12,75	12,41	12,71	14,03	12,66	12,54	12,91	12,53	12,63	11,45	4,09	1,62	4,34	2,44	2,59	3,45	6,11	2,19	2,64	2,13	2,23	9,06	4,68	7,89	19,38	11,82	28,00	21,88
Total	99,80	99,30	100,00	100,00	99,80	100,00	99,30	99,30	99,60	100,00	99,70	100,00	99,70	100,00	100,00	99,50	100,00	100,00	100,00	100,00	100,00	100,00	100,00	100,00	100,00	100,00	100,00	100,00	99,40	99,40	99,40
K2O/Na2O	0,36	0,35	0,33	0,33	0,35	0,36	0,36	0,36	0,35	0,34	0,34	0,35	0,39	0,94	0,87	0,55	0,70	0,74	0,61	0,47	0,55	0,59	0,51	0,62	0,48	0,58	0,49	0,40	0,74	0,26	0,48
Al2O3/TiO2	20,87	21,24	21,46	22,38	22,38	20,65	20,85	21,96	22,30	22,07	22,62	22,64	24,53	21,77	22,71	6,65	14,88	22,83	11,13	24,50	7,80	15,59	7,47	11,21	9,24	11,12	5,97	2,96	3,73	4,09	14,90
SiO2/Al2O3	3,27	3,18	2,96	2,84	3,08	3,03	3,19	3,08	3,09	3,05	3,07	3,08	2,87	4,79	5,83	6,78	7,35	7,09	5,84	6,08	6,11	6,14	6,91	6,46	5,46	4,10	4,40	4,61	4,88	4,68	4,14
log (K2O/Na2O)	-0,45	-0,46	-0,48	-0,48	-0,46	-0,45	-0,44	-0,45	-0,45	-0,46	-0,47	-0,46	-0,40	-0,03	-0,06	-0,26	-0,15	-0,13	-0,21	-0,33	-0,26	-0,23	-0,29	-0,21	-0,32	-0,24	-0,31	-0,40	-0,13	-0,58	-0,32
log (Al2O3/TiO2)	1,32	1,33	1,33	1,35	1,35	1,31	1,32	1,34	1,35	1,34	1,35	1,35	1,39	1,34	1,36	0,82	1,17	1,36	1,05	1,39	0,89	1,19	0,87	1,05	0,97	1,05	0,78	0,47	0,57	0,61	1,17
log (SiO2/Al2O3)	0,51	0,50	0,47	0,45	0,49	0,48	0,50	0,49	0,49	0,48	0,49	0,49	0,46	0,68	0,77	0,83	0,87	0,85	0,77	0,78	0,79	0,79	0,84	0,81	0,74	0,61	0,64	0,66	0,69	0,67	0,62
CIA	73,43	73,58	75,88	76,4	74,27	76,41	74,38	74,61	74,34	74,79	73,84	74,03	74,75	73,39	67,59	67,8	66,11	65,26	68,05	67,54	69,08	68,97	68,19	70,81	73,13	76,06	76,52	80,58	78,31	74,64	74,59
PIA	77,24	77,31	79,43	79,92	77,99	80,15	78,21	78,42	78,11	78,46	77,45	77,75	78,87	81,54	75,15	73,03	72,38	71,67	73,82	72,15	74,45	74,61	73,15	76,83	78,01	81,59	81,34	84,4	84,71	77,55	79,47
CIW	78,95	78,98	80,75	81,18	79,55	81,46	79,8	79,97	79,69	79,95	79,03	79,36	80,49	84,28	79,55	76,49	76,87	76,59	77,43	75,38	77,59	77,89	76,37	79,75	80,11	83,36	82,89	85,32	86,26	78,81	81,32
ICV	1,012	0,991	0,898	0,857	0,912	0,9	0,955	0,906	0,904	0,902	0,9	0,894	0,896	0,826	1,062	2,36	1,432	1,205	1,59	1,642	1,985	1,429	2,025	1,549	2,583	1,602	2,731	8,224	4,822	11,72	4,841

CaO* is the CaO value that has been corrected based on Mc Lennan (1990)

contrast, coastal sediments show scattered and irregular distributions, reflecting the influence of variable physical processes such as wave action, currents, and fluctuating terrigenous input. This observation is consistent with previous studies reporting that coastal sediments generally exhibit higher geochemical variability than deeper marine sediments due to stronger continental and oceanographic controls (e.g., Morton, 2002; Garzanti et al., 2018).

DISCUSSION

Provenance

The provenance analysis of seabed and coastal sediments from the Limau Waters area was conducted using two geochemical approaches: the discriminant function diagram by Roser & Korsch (1988) and the TiO_2 versus Zr plot by Hayashi et al. (1997), in order to better constrain the nature of the source rocks. The discriminant function diagram (Figure 6), which utilizes multiple major oxide elements (TiO_2, Al_2O_3, Fe_2O_3, MgO, CaO, Na_2O, and K_2O), indicates that the seabed sediments predominantly plot within the intermediate igneous provenance field, with several samples extending toward the mafic domain. In contrast, coastal sediments are more widely scattered, with several samples plotting within the felsic igneous field and others extending into the recycled/mature quartzose sedimentary provenance area. This suggests that coastal sediments were derived from a more mixed and possibly reworked source, which may include older continental or volcanic materials (Cullers, 1994; Roser & Korsch, 1988).

The TiO_2 vs Zr plot (Figure 7), which focuses on magmatic differentiation trends, shows that most seabed sediment samples cluster within the felsic igneous rock field, characterized by relatively low TiO_2 content and enriched Zr values. This distribution may reflect the presence of resistant heavy minerals such as zircon, typically concentrated during sedimentary sorting processes from felsic sources (Hayashi et al., 1997; McLennan et al., 1993). On the other hand, coastal sediments are primarily plotted in the mafic to intermediate igneous fields, indicating higher TiO_2 content and suggesting a more direct input from mafic volcanic rocks, likely of local origin.

The apparent discrepancy between the two diagrams can be explained by the different sensitivities and focuses of each method. The discriminant function diagram is more robust in identifying general provenance trends because it integrates multiple major elements, and is thus less sensitive to grain size effects or mineral sorting (Gaspar et al., 2022; Nagarajan et al., 2023). In contrast, TiO_2–Zr (or TiO_2 vs. Zr) diagrams are particularly sensitive to the selective enrichment of resistant heavy minerals (e.g., zircon, rutile,

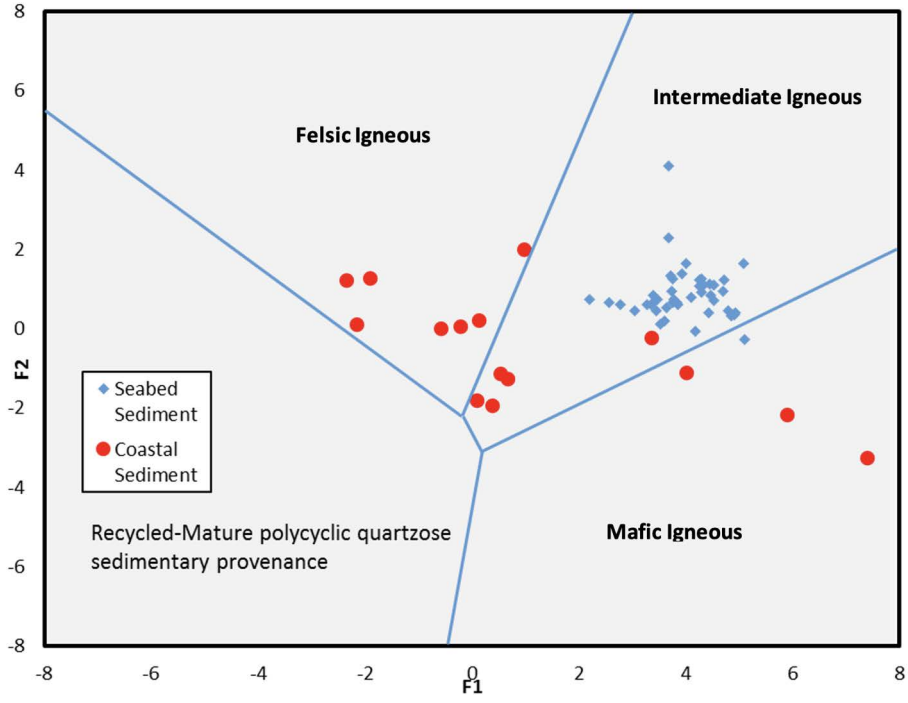

Figure 6. Provenance Discriminant Function Diagram (Roser and Korsch, 1988) with following equation (6) and (7)

ilmenite); hydrodynamic concentration or reworking of these minerals can artificially shift Ti–Zr systematics and bias provenance interpretation toward more felsic signatures (Patias et al., 2024).

Taken together, these results suggest that the seabed sediments are largely derived from intermediate to felsic volcanic sources, possibly influenced by offshore inputs and the enrichment of heavy minerals, while the coastal sediments reflect a more heterogeneous provenance, involving mafic volcanic input and reworked continental or sedimentary material. These interpretations are consistent with the regional geology of the Limau coastal area, which comprises both Tertiary and Quaternary volcanic rocks, including andesitic, basaltic, and rhyolitic lithologies (Irzon, 2020). It also accordance with the regional geological conditions and rock outcrops found in the field, where in the Limau mainland area and its surroundings according to Amin et al. (1993) is predominantly composed of the Hulusimpang volcanic rock formation with some granite intrusion rocks. The Hulusimpang Formation is an Oligocene-Miocene volcanic rock formation consisting of volcanic breccia, lava, and tuff with andesitic - basaltic composition. Meanwhile, the Miocene granite intrusion is an igneous rock that cut through the Hulusimpang Formation. This rock is a felsic intrusive rock with local distribution. It appears that the seabed sediment at the study area has more potential to contain sulfide minerals compared to coastal sediment, because of their correlation to the Hulusimpang Formation.

Paleoweathering and sediment maturity

The paleoweathering conditions and sediment maturity of the seabed and coastal sediments in the Limau Waters area were evaluated using a two-dimensional CIA–ICV plot that integrates geochemical indices reflecting weathering intensity and sediment maturity (Figure 8). This type of plot is commonly constructed using the Chemical Index of Alteration (CIA) and the Index of Compositional Variability (ICV), following the approaches of Nesbitt & Young (1982), and Cox et al. (1995). The vertical axis at approximately CIA = 70 separates weakly weathered (CIA < 70) from intensely weathered (CIA > 70) source terrains (Nesbitt & Young, 1982).

The majority of both seabed and coastal sediment samples fall within the weak weathering field, suggesting limited chemical alteration, likely due to derivation from volcanic or young arc-related sources with minimal exposure to prolonged tropical weathering. A subset of coastal samples, however, lies beyond the CIA = 70 threshold, suggesting contribution from more weathered or older continental sources (McLennan, 1993).

Sediment maturity in Limau Waters area is inferred from the horizontal axis at ICV = 1, where values <1 indicate mature sediments (quartz-rich and compositionally stable), while values >1 reflect immature sediments (feldspar- or mafic-rich, less altered) (Cox et al., 1995). The results show that Seabed sediments cluster mostly fall near or just

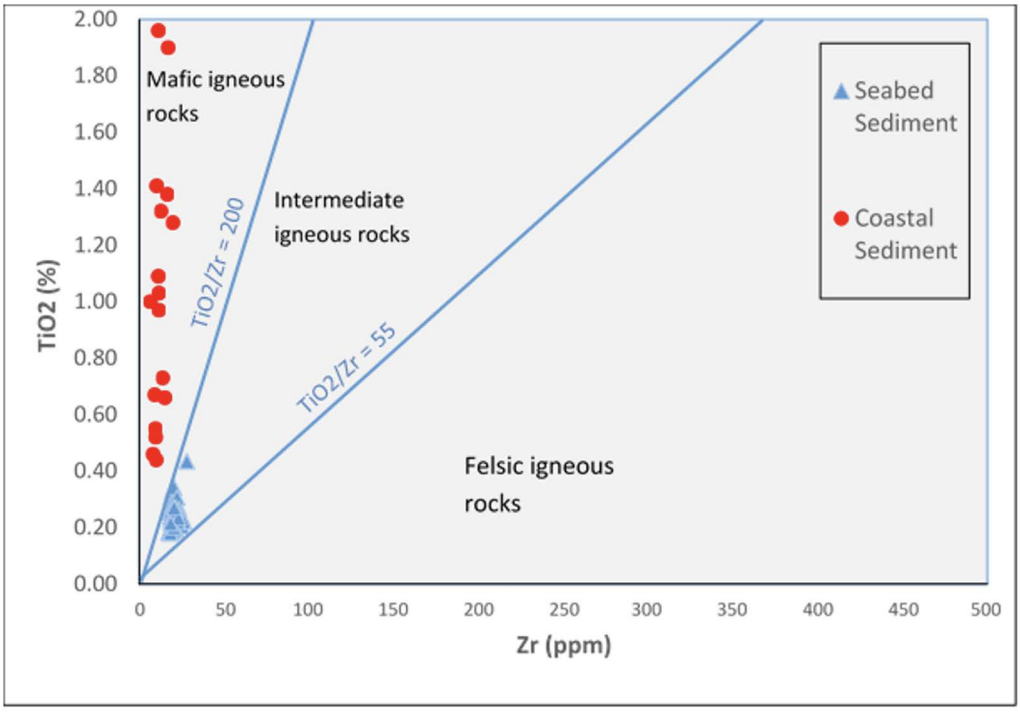

Figure 7. TiO_2 vs Zr plot (Hayashi et al., 1997)

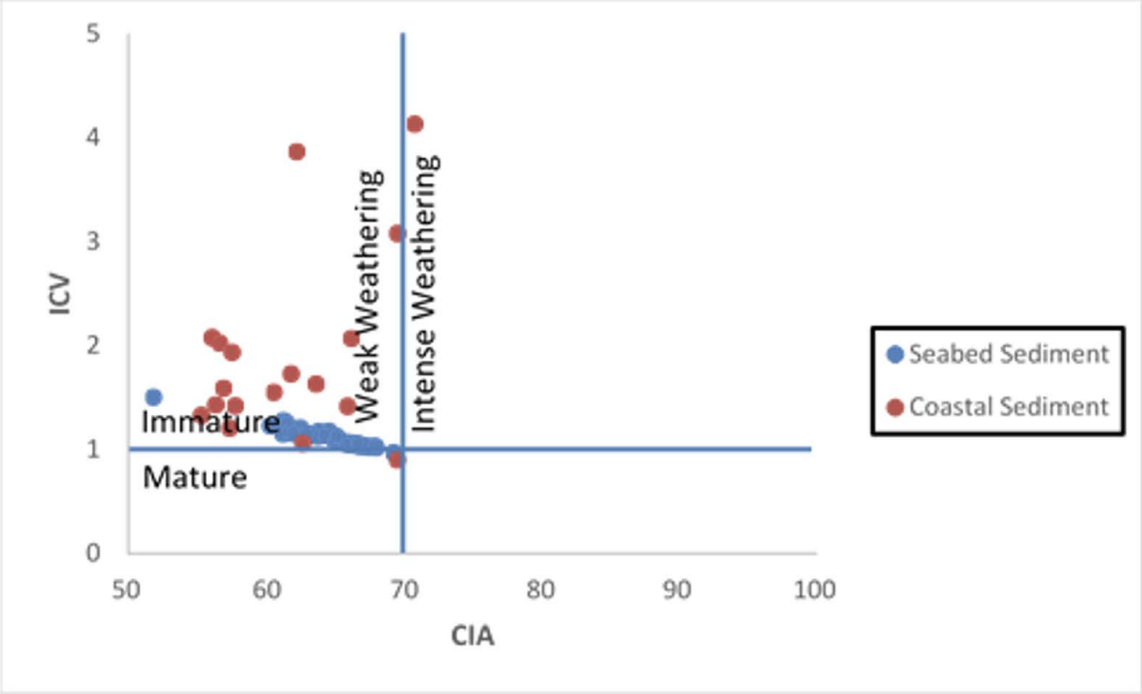

Figure 8. ICV vs CIA diagram (Nesbit and Young 1984; Cox et al. 1995)

below the ICV = 1, implying a dominance of stable mineral components and possible sedimentary reworking or recycling. Meanwhile, Coastal sediments predominantly fall into the immature field, consistent with derivation from first-cycle volcanic sources, with minimal transport or chemical weathering.

The seabed sediments, being more compositionally mature, likely underwent longer transport or offshore reworking, resulting in enrichment of stable mineral phases such as quartz and depletion of labile elements. In contrast, the coastal sediments retain the signature of proximal volcanic sources, characterized by limited chemical weathering and short transport distances, consistent with active arc settings. These findings complement the provenance interpretations derived from major element discrimination diagrams (Hayashi et al., 1997; Roser & Korsch, 1988), in which seabed sediments show felsic to intermediate igneous affinities, while coastal sediments exhibit stronger mafic volcanic signatures.

CONCLUSSIONS

The integration of provenance and geochemical weathering–maturity data reveals distinct differences in the sedimentary characteristics of seabed and coastal sediments in the Limau Waters area. These differences reflect variations in source rock composition, weathering intensity, and depositional processes. Provenance analysis indicates that seabed sediments are predominantly derived from intermediate to felsic igneous sources, as evidenced by their low TiO_2 and relatively high Zr contents. This suggests possible contributions from felsic volcanic rocks and enrichment of resistant heavy minerals such as zircon. In contrast, coastal sediments display a geochemical affinity toward mafic to intermediate igneous sources, likely reflecting direct input from nearby Quaternary volcanic rocks. Paleoweathering and maturity analysis-supports this distinction. Seabed sediments are generally geochemically mature (ICV < 1) and exhibit low chemical weathering intensity (CIA < 70), indicating a stable mineralogical composition possibly resulting from longer transport or sedimentary reworking. Coastal sediments, on the other hand, are immature (ICV > 1) and more compositionally variable, with a few samples showing signs of moderate to intense chemical weathering (CIA > 70), suggesting limited transport and derivation from less altered, first-cycle volcanic sources. Together, the data suggest that seabed sediments have undergone more extensive geochemical stabilization and sedimentary processing, while coastal sediments represent more proximal and compositionally diverse inputs, reflecting the active volcanic geology of the region. These findings provide a comprehensive

understanding of sediment dispersal and source rock contributions in the Limau Waters area.

ACKNOWLEDGEMENTS

The authors sincerely acknowledge the support and facilitation provided by the Head of the Marine Geological Institute, Ministry of Energy and Mineral Resources of the Republic of Indonesia. We are also deeply grateful to all members of the Marine Geological Institute survey team whose dedication, technical assistance, and collaborative spirit have significantly contributed to the completion of this scientific work. Their efforts during field surveys, sample processing, data analysis, and insightful discussions were essential to the success of this study.

REFERENCES

Advokaat, E. L., Bonger, M. L. M., Rudyawan, A., BouDagher-Fadhel, M. K., Langereis, C. G., & van Hinsbergen, D. J. J., 2018. Early Cretaceous origin of the Woyla Arc, Sumatra. *Earth and Planetary Science Letters, 498,* 348–361.

Anenburg, M., & Liu, Y., 2024. A Global Marine Sediment Compilation and a Cerium Anomaly Perspective on Metasomatized Mantle Sources for REE-Mineralized Carbonatites. Journal of Geophysical Research: Solid Earth, 129(7), e2023JB028546. https://doi.org/10.1029/2023JB028546

Amin, T. C., Sidarto, Santosa, S., & Gunawan, W., 1993. *Peta geologi bersistem lembar Kotaagung skala 1:250.000.* Pusat Penelitian dan Pengembangan Geologi, Departemen Pertambangan dan Energi.

Barber, A. J., & Crow, M. J., 2005. Structure and structural history. In A. J. Barber, M. J. Crow, & J. S. Milsom (Eds.), *Sumatra: Geology, resources, and tectonic evolution* (Geological Society Memoir No. 31, pp. 295–310). Geological Society, London.

Bau, M., Möller, P., & Dulski, P., 1997. Yttrium and lanthanides in eastern Mediterranean seawater and their fractionation during redox-cycling. Marine Chemistry, 56(1-2), 123-131. https://doi.org/10.1016/S0304-4203(96)00091-6

BBSPGL., 2024. *Laporan Survei Prospeksi Mineral Letakan Emas (Au Placer) Di Perairan Limau Dan Sekitarnya, Teluk Semangko, Provinsi Lampung.* Balai Besar Survei dan Pemetaan Geologi Kelautan. [Internal report, unpublished].

Cox, R., Lowe, D. R., & Cullers, R. L., 1995. The influence of sediment recycling and basement composition on evolution of mudrock chemistry in the southwestern United States. *Geochimica et Cosmochimica Acta, 59*(14), 2919–2940. https://doi.org/10.1016/0016-7037(95)00185-9

Crow, M. J., & van Leeuwen, T. M., 2005. Metallic mineral deposits. In A. J. Barber, M. J. Crow, & J. S. Milsom (Eds.), *Sumatra: Geology, resources and tectonic evolution* (Geological Society Memoir No. 31, pp. 147–174). Geological Society, London.

Cruz, A., Dinis, P. A., Gomes, A., & Leite, P., 2021. Influence of sediment cycling on the rare-earth element geochemistry of fluvial deposits. *Geosciences, 11*(9), 384. https://doi.org/10.3390/geosciences11090384

Cullers, R. L., 1994. The controls on the major and trace element evolution of shales, siltstones, and sandstones of Ordovician to Tertiary age in the western United States. *Chemical Geology, 114,* 297–323.

Darlan, Y., 1997. Sedimen permukaan dasar laut sebagai perangkap endapan emas letakan di perairan Teluk Semangko, Lampung Selatan. In *Proceedings of the Indonesian Geologists Association at the XXVI Annual Scientific Meeting* (pp. 913–922). Jakarta.

Ekoa Bessa, A. Z., Ndjigui, P. D., Fuh, G. C., Armstrong-Altrin, J. S., & Betsi, T. B., 2021. Mineralogy and geochemistry of the Ossa Lake Complex sediments, Southern Cameroon: Implications for paleoweathering and provenance. *Arabian Journal of Geosciences, 14,* 322. https://doi.org/10.1007/s12517-021-06646-3

Fedo, C. M., Nesbitt, H. W., & Young, G. M., 1995. Unraveling the effects of potassium metasomatism in sedimentary rocks and paleosols, with implications for paleoweathering conditions and provenance. *Geology, 23,* 921–924.

Garzanti, E., Resentini, A., & Andò, S., 2018. Provenance of passive-margin sand (southern Africa). *Journal of Sedimentary Research*, 88(1), 47–64.

Gaspar, L., Blake, W. H., Lizaga, I., Latorre, B., & Navas, A., 2022. Particle size effect on geochemical composition of experimental soil mixtures relevant for unmixing modelling. *Geomorphology*, *403*, 108178. https://doi.org/10.1016/j.geomorph.2022.108178

Guan, Y., Chen, Y., Sun, X., Xu, L., Xu, D., Zhu, Z., & He, W., 2023. The Clay Mineralogy and Geochemistry of Sediments in the Beibu Gulf, South China Sea: A Record of the Holocene Sedimentary Environmental Change. *Journal of Marine Science and Engineering*, *11*(7), 1463. https://doi.org/10.3390/jmse11071463

Hayashi, K. I., Fujisawa, H., Holland, H. D., & Ohmoto, H., 1997. Geochemistry of ~1.9 Ga sedimentary rocks from northeastern Labrador, Canada. *Geochimica et Cosmochimica Acta, 61,* 4115–4137.

Harnois, L., 1988. The CIW index: A new chemical index of weathering. *Sedimentary Geology, 55,* 319–322.

Irzon, R., 2020. Komparasi geokimia batuan gunung api Kuarter dan Tersier di Tepian Selatan Lampung. Eksplorium, 41(2), 101–114. https://doi.org/10.17146/eksplorium.2020.41.2.6053

Li, X., Ge, J., Zhao, X., Qi, K., Jones, B. G., & Fang, X., 2024. Geochemistry of Quaternary sediments in the northwestern South China Sea: Sediment provenance and mid-Pleistocene transition. *Marine Geology*, *477*, 107371. https://doi.org/10.1016/j.margeo.2024.107371

McDonough, W. F., & Sun, S. -s., 1995. The composition of the Earth. Chemical Geology, 120(3), 223–253. https://doi.org/https://doi.org/10.1016/0009-2541(94)00140-4

McLennan, S. M., 1989. Rare earth elements in sedimentary rocks: Influence of provenance and sedimentary processes. In B. R. Lipin & G. A. McKay (Eds.), Geochemistry and mineralogy of rare earth elements (Reviews in Mineralogy, Vol. 21, pp. 169–200). Mineralogical Society of America. https://doi.org/10.1515/9781501509032-010

McLennan, S. M., Hemming, S. R., McDaniel, D. K., & Hanson, G. N., 1993. Geochemical approaches to sedimentation, provenance, and tectonics. In Processes *controlling the composition of clastic sediments* (Geological Society of America Special Paper 284, pp. 21–40). Geological Society of America.

Metcalfe, I., 2017. Tectonic evolutions of Sundaland. *Bulletin of the Geological Society of Malaysia, 63,* 27–60. https://doi.org/10.7186/bgsm63201702

Morton, A. C., 2002. Provenance indicators and their value in sedimentary petrology. In: *Provenance of Arenites* (pp. 113–142). Springer, Dordrecht.

Muksin, I., & Heditama, D. M., 2016. *Laporan eksplorasi umum endapan zeolit Kecamatan Limau, Kabupaten Tanggamus Provinsi Lampung.* Pusat Sumber Daya Mineral, Batubara dan Panas Bumi. [Internal report, unpublished].

Nagarajan, R., Eswaramoorthi, S. G., Anandkumar, A., & Ramkumar, M., 2023. Geochemical fractionation, mobility of elements and environmental significance of surface sediments in a Tropical River, Borneo. *Marine Pollution Bulletin*, *192*, 115090. https://doi.org/10.1016/j.marpolbul.2023.115090

Nesbitt, H. W., & Young, G. M., 1982. Early Proterozoic climates and plate motions inferred from major element chemistry of lutites. *Nature, 299,* 715–717. https://doi.org/10.1038/299715a0

Nesbitt, H. W., & Young, G. M., 1984. Prediction of some weathering trends of plutonic and volcanic rocks based on thermodynamic and kinetic considerations. *Geochimica et Cosmochimica Acta, 48,* 1523–1534.

Patias, D., Zhou, R., Aitchison, J. C., Cluzel, D., Ireland, T., Lian, D., & Yang, J., 2024. Beyond zircon fingerprinting: Zircon and TiO2 polymorphs constrain genealogy and evolution of the New Caledonian ophiolite. Chemical Geology, 644, 121841. https://doi.org/10.1016/j.chemgeo.2023.121841

Ramos-Vázquez, M.A., Armstrong-Altrin, J.S. Provenance of sediments from Barra del Tordo and Tesoro beaches, Tamaulipas State, northwestern Gulf of Mexico. J. Palaeogeogr. 10, 20, 2021. https://doi.org/10.1186/s42501-021-00101-4

Roser, B. P., & Korsch, R. J., 1988. Provenance signatures of sandstone–mudstone suites determined using discriminant function analysis of major-element data. *Chemical Geology, 67,* 119–139.

Ruban, A., Dudarev, O., Rudmin, M., & Semiletov, I., 2024. Rare Earth Elements in Sediments from the Laptev Sea Shelf: Insight into Sources and Distribution Factors. *Quaternary*, *7*(1), 12. https://doi.org/10.3390/quat7010012

Sousa, T. A., Venancio, I. M., Marques, E. D., Figueiredo, T. S., Nascimento, R. A., Smoak, J. M., Albuquerque, A. L., Valeriano, C. M., & Vieira, E., 2022. REE Anomalies Changes in Bottom Sediments Applied in the Western Equatorial Atlantic Since the Last Interglacial. *Frontiers in Marine Science*, *9*, 846976. https://doi.org/10.3389/fmars.2022.846976

Sukardjono, H., Kurnio, H., Hardjawidjaksana, K., Lugra, I. W., Silitonga, F., & Budiman., 1990. *Laporan penyelidikan geologi dan geofisika di kawasan Kompleks Teluk Semangko, Lampung Selatan.* Pusat Pengembangan Geologi Kelautan. [Internal report, unpublished].

Taylor, S. R., & McLennan, S. M., 1985. *The Continental Crust: Its Composition and Evolution*. Oxford: Blackwell.

Zhang, K., & Shields, G. A., 2022. Sedimentary Ce anomalies: Secular change and implications for paleoenvironmental evolution. Earth-Science Reviews, 229, 104015. https://doi.org/10.1016/j.earscirev.2022.104015

Zhang, Y., Zhang, Z., Stephenson, W., & Chen, Y., 2024. Geochemical Behavior of Rare Earth Elements in Tidal Flat Sediments from Qidong Cape, Yangtze River Estuary: Implications for the Study of Sedimentary Environmental
Change. *Land*, *13*(9), 1425. https://doi.org/10.3390/land13091425

FORAMINIFERA DISTRIBUTION AS AN INDICATOR OF PALEOCEANOGRAPHY IN WAIPOGA WATERS, NORTHERN PAPUA

DISTRIBUSI FORAMINIFERA SEBAGAI INDIKATOR PALEOSEANOGRAFI DI PERAIRAN WAIPOGA, PAPUA UTARA

Joleen Felicia Wijaya[1], Resti Samyati Jatiningrum[1*], Luli Gustiantini[2], Mardhatillah Kurnia Putri[3], Yulinar Firdaus[2]

[1] Geological Engineering Study Program, Faculty of Exploration and Production Technology, Universitas Pertamina, Jl. Teuku Nyak Arief, Jakarta

[2] Marine Geological Institute, Jl. Dr. Junjunan no.236, Bandung

[3] Department of Oceanography, Faculty of Earth Sciences and Technology, Bandung Institute of Technology, Jl. Ganesha No. 10, Bandung

*Corresponding author: resti.sj@universitapertamina.ac.id

(Received 16 September 2025; in revised from 17 September 2025; accepted 29 December 2025)

DOI : 10.32693/bomg.40.2.2025.965

ABSTRACT: Foraminifera are widely used as indicators for reconstructing past marine environmental conditions. This study aims to investigate the ecological conditions of Waipoga waters, North Papua, by analyzing the distribution of foraminifera during the late Middle Holocene to Late Holocene. The study area plays an important role in the dynamics of the Indonesian Throughflow (ITF/ITF) and ENSO. Sediment core samples were prepared and identified for foraminifera, followed by quantitative analyses including relative abundance, P/B ratio, and ecological indices. In addition, sortable silt analysis was applied as an environmental proxy to support the reconstruction of past environmental changes. The results show that foraminiferal abundance throughout the sediment core varies. Planktonic foraminifera are more dominant, comprising 12 genera with 22 species. The most dominant species are *Globigerinoides ruber* (41,7%), *Neogloboquadrina dutertrei* (11%), *Neogloboquadrina incompta* (13,2%), *Pulleniatina obliquiloculata* (4%), *Hastigerina pelagica* (6,65%), and *Globigerinoides immaturus* (6,7%). Meanwhile, benthic foraminifera consist of 42 genera with 62 species, dominated by *Bulimina marginata* (1,8%), *Cibicidoides pachyderma* (1,89%), and *Lenticulina calcar* (1,3%). During the late Middle Holocene to Late Holocene, the Waipoga waters were influenced by variations in bottom current intensity and thermocline stability. Zones I and III reflect oligotrophic conditions with weak circulation, while Zone II indicates increased bottom current intensity, high productivity, and dysoxic conditions, suggesting possible intensification of upwelling events.

Keywords: Distribution, Foraminifera, Holocene, Waipoga Waters

ABSTRAK: *Foraminifera merupakan indikator yang sering digunakan untuk merekonstruksi kondisi lingkungan perairan masa lampau. Penelitian ini bertujuan untuk mengetahui kondisi lingkungan Perairan Waipoga, Papua Utara, dengan menganalisis distribusi foraminifera selama Kala akhir Holosen Tengah hingga Holosen Akhir. Wilayah penelitian berperan dalam dinamika ITF dan ENSO. Sampel inti sedimen dianalisis melalui preparasi dan identifikasi foraminifera, kemudian dilakukan analisis kuantitatif berupa perhitungan kelimpahan relatif, rasio P/B, dan indeks ekologi. Selain itu, analisis ukuran butir sedimen digunakan sebagai proksi kondisi lingkungan untuk mendukung rekonstruksi perubahan lingkungan purba. Hasil penelitian menunjukkan kelimpahan foraminifera sepanjang inti sedimen bervariasi. Foraminifera*

planktonik lebih dominan terdiri atas 12 genus dengan 22 spesies. Spesies yang lebih dominan adalah Globigerinoides ruber (41,7%), Neogloboquadrina dutertrei (11%), Neogloboquadrina incompta (13,2%), Pulleniatina obliquiloculata (4%), Hastigerina pelagica (6,65%), dan Globigerinoides immaturus (6,7%). Sementara itu, foraminifera bentonik terdiri dari 42 genus dengan 62 spesies, didominasi oleh Bulimina marginata (1,8%), Cibicidoides pachyderma (1,89%), dan Lenticulina calcar (1,3%). Sepanjang akhir Holosen Tengah hingga Holosen Akhir, kondisi perairan Waipoga dipengaruhi oleh variasi intensitas arus dasar laut dan stabilitas termoklin. Zona I dan III mencerminkan kondisi oligotrofik dengan sirkulasi lemah, sementara Zona II menunjukkan peningkatan intensitas arus dasar laut, produktivitas tinggi, dan kondisi disoksik yang mengindikasikan kemungkinan intensifikasi peristiwa upwelling.

Kata Kunci: *Distribusi, Foraminifera, Holosen, Perairan Waipoga*

INTRODUCTION

The Waipoga waters are located in the eastern part of Cenderawasih Bay (Figure 1), north of Papua Island in the Pacific Ocean, and hold a strategic position as an area that is passes through by New Guinea Coastal Current (NGCC) and New Guinea Coastal Under Current (NGCUC) which flow from the Pacific Ocean enters the Indonesian Waters as the Indonesian Throughflow (ITF) (Gordon, 1986). The Indonesian Throughflow (ITF) is a flow of water masses between the Pacific Ocean and the Indian Ocean that passes through Indonesian waters, with the ITF pathways shown in Figure 2. The ITF transports warm water masses from the Pacific Ocean toward the Indian Ocean, which has relatively cooler temperatures (Wyrtki, 1987). The ITF occurs due to density differences influenced by pressure, temperature, and salinity between the two oceans (Hasanudin, 1998; Nining, 2002 in Azis, 2006). In addition, as the source of the Indonesian Throughflow, the northern Papua waters are also situated within the Western Pacific Warm Pool (WPWP), thus influenced by the El Niño Southern Oscillation (ENSO). WPWP is a pool of warm water located in the western Pacific region, including the eastern Indonesian waters, that can shift eastward or westward across the Pacific, generating a circulation known as the ENSO cycle or El Niño Southern Oscillation. ENSO is a periodic phenomenon caused by unusual interactions between the ocean and atmosphere along the equatorial Pacific Ocean, which impacts climate variability in the region as well as in several other parts of the world. El Niño occurs when sea surface temperatures in the eastern Pacific Ocean rise, while those in the western Pacific decline (with the WPWP shifting further eastward), resulting in reduced rainfall in the western Pacific and increased rainfall in the eastern Pacific. La Niña, on the other hand, has the opposite effect, with sea surface temperatures decreasing in the eastern Pacific while increasing in the western Pacific, leading to higher rainfall in the western Pacific, including Indonesian waters (Ashok & Yamagata, 2009; Darmawan et al., 2021), meaning the WPWP shifts further westward. The variation in sea surface temperatures in the northern Papua waters influenced by ENSO is related to the formation of cyclonic and anticyclonic eddies, which drive upwelling and downwelling processes (Simanungkalit et al., 2018). The formation of anticyclonic eddies is caused by high sea surface temperatures during La Niña conditions, leading to the accumulation of water masses at the eddy's center. Cyclonic eddies, in turn, can trigger upwelling processes by bringing cooler water masses to the sea surface. ENSO events affect the ITF and monsoon circulation, hence influence the climate over the Asian region.

Foraminifera are unicellular microorganisms that are commonly found from shallow to deep marine environments, as well as in brackish waters, and exhibit very high diversity. Foraminifera tend to prefer specific environmental conditions, although some species can thrive in a wide range of settings. Therefore, foraminifera are known as proxies for paleoclimate changes, and their presence can reflect the ecological conditions of their habitats. Both benthic and planktonic foraminifera are recognized as potential indicators of environmental, ecological, oceanographic, and climatological conditions, both in the past and present. Based on their characteristics—such as a simple body structure with a hard shell, relatively short life cycles, wide distribution in aquatic environments, and high adaptability to environmental changes—foraminifera are often considered bioindicators with great potential for understanding environmental conditions in both ancient and modern waters(Nurruhwati et al., 2012). The distribution,

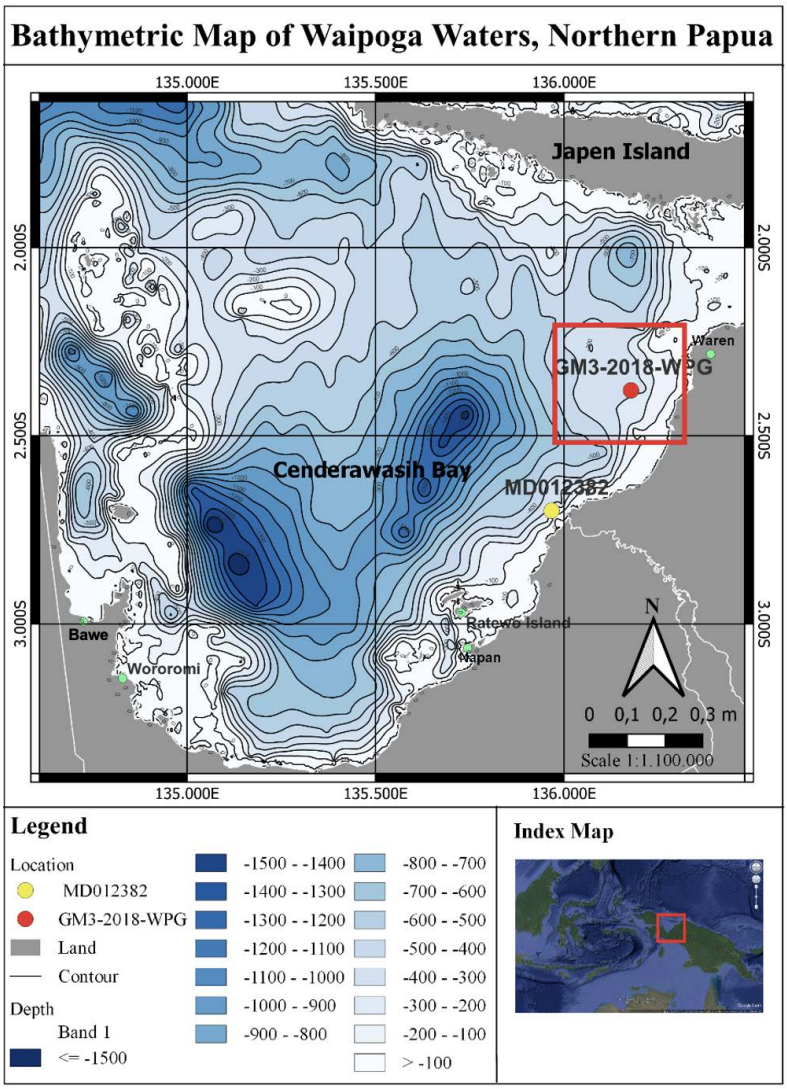

Figure 1. Bathymetric map of Waipoga waters, Northern Papua, red dot is the sediment core for this study, yellow dot is the sediment core for age modelling (Maryunani, 2009).

morphology, and abundance of foraminifera are influenced by various environmental factors in their habitats, such as depth, salinity, temperature, nutrient availability, oxygen concentration, and others (Boltovskoy and Wright, 1976; Jurnaliah et al., 2019). Previous studies (e.g. Peeters et al., 2001; Gustiantini, 2018; Gustiantini et al., 2018; Jurnaliah et al., 2019; Damanik et al., 2020; Fabbrini et al., 2023; Jatiningrum et al., 2023) have concluded that the distribution of foraminifera in different marine regions is influenced by climate change. Therefore, this research was conducted to further study the distribution of foraminifera in relation to paleoceanographic conditions in Waipoga waters.

METHODS

The data used in this study consist of marine sediment core sample from Waipoga waters with the code NAME GM3-2018-WPG.04. The collection of marine sediment core was carried out by the Marine Geological Institute (MGI/BBSPGL) of the Geological Agency, Ministry of Energy and Mineral Resources, using a gravity corer on aboard the survey vessel Geomarin III in 2018, retrieved from a water depth of 462 m.

Observations and data collection began with the description of a 206 cm-long gravity core sediment sample. The core description included color, grain size classification following Wentworth (1922), and observed structures. Preparation of sediment samples for foraminiferal analysis started with the extraction

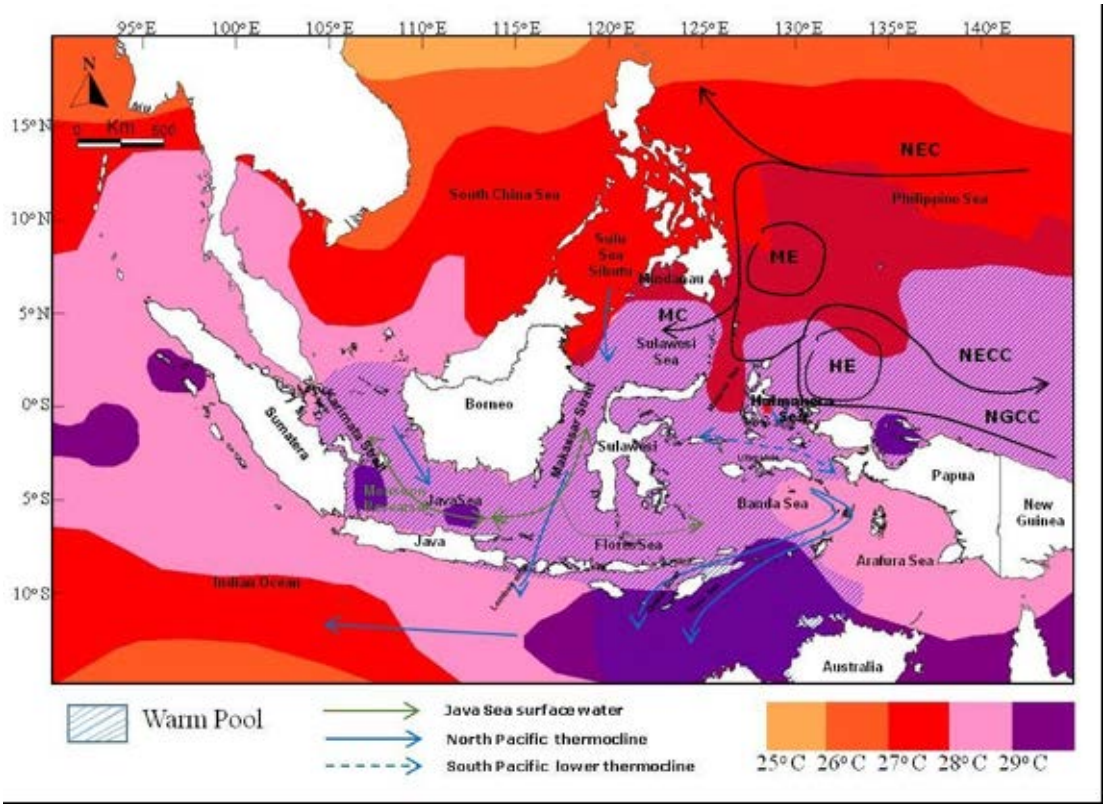

Figure 2. Oceanography and climatology within Indonesian waters**.** Black arrows indicate the major ocean currents influencing Indonesian waters, including the NGCC (New Guinea Coastal Current), NEC (North Equatorial Current), NECC (North Equatorial Counter Current), HE (Halmahera Eddy), ME (Mindanau Eddy), while blue arrows show the pathway of the Indonesian Throughflow (ITF) (Gustiantini, 2018).

of 5–7 cc of sample using a syringe at 2 cm depth intervals. Sediment samples were firstly weighed, before and afterwards they were dried to obtain wet and dry weights, then soaked, washed with a 0.063 mm sieve, and dried again. Subsequently, splitting and picking of foraminifera were carried out, with approximately 300 specimens separated from the sediment. Identification referred to Loeblich & Tappan (1994), Hemleben et al. (1989), and Holbourn et al. (2013). Quantitative analysis was then performed, including normalization, relative abundance (%), P/B ratio, ecological indices (diversity index, evenness index, and dominance index), and clustering. The calculation of ecological indices and the construction of clustering dendrograms were carried out using the PAST (Paleontological Statistics) software version 4.03, available at https://paleoelectronica.org/2001_1/past/pastprog/index.html, developed by Paul D. Ryan (1995) in Hammer et al. (2001), with manual book of PAST (Hammer, 1999-20224).

Normalization to the number of splits (dividers) with the sample weight and the number of individual specimens in the normalized sample can be carried out by (Ardi et al., 2019) :

$$(N) = 2^n \, x \, A \qquad (1)$$

$$(Nz) = \left(\frac{Ma}{Mb}\right) \qquad (2)$$

Where:

N = number of individuals of a species in the total sample
n = number of splits (dividers)
A = number of individuals of a species in one split
Nz = number of individuals in the normalized sample
Ma = measured mass
Mb = expected mass

Relative abundance analysis was carried out to calculate the percentage of abundance of each species present in the sample (Junita et al., 2020)

.

Relative Abundance = $\frac{Ni}{N}$ (3)

Where:
Ni : Total individuals of the species
N : Total foraminifera in one sample

The calculation of the ratio between the number of planktonic and benthic foraminifera (P/B ratio) in each sample indicates paleobathymetric changes based on the classification of Grimsdale & Morkhoven (1955), using the following formula, according to the study conducted by van Marle (1989) dalam Jurnaliah et al. (2017):

$$P/B\ Ratio = \frac{P}{P+B}\ x\ 100\% \quad (4)$$

Where:
P = number of planktonic individuals
B = number of benthic individuals

Ecological Indices

Diversity Index

Hammer et al. (2009) explained that the Shannon index, also called entropy, considers both the number of taxa and their relative abundances. Its value approaches 0 when only a single taxon is present, while higher values indicate richer and more even communities. The calculation of the diversity index uses the Shannon-Weaver formula (Bakus, 1990, in Jurnaliah et al., 2019):

$$H' = -\Sigma\, pi \log pi \quad (5)$$

Where:
H' = Diversity index
Pi = $\frac{Ni}{N}$
S = Number of species
Ni = Number of individuals of i1, i2, i3, etc.
N = Total number of individuals

With the H' value range as follows:

1. H' < 1.0: Low, indicating high ecological stress, low productivity, and a disturbed ecosystem
2. 1.0 < H' < 3.0: Moderate, indicating moderate ecological stress, moderate productivity, and a slightly disturbed ecosystem
3. H' > 3.0: High, indicating low ecological stress, high productivity, and a stable ecosystem

Evenness Index

Evenness can also be expressed as Shannon diversity divided by the logarithm of the number of taxa, reflecting how evenly individuals are spread among taxa (Hammer et al., 2009). Evenness index obtained from the formula of Buzas and Gibson's evenness in Hammer (1999-2024):

$$Buzas\ and\ Gibson'evenness = \frac{e^H}{S} \quad (6)$$

Where:
E = Evenness index
H' = Diversity index
Hmax = log2 S
S = Number of species

With the E criteria as follows:

1. E > 0.6: High species evenness
2. 0.6 ≥ E ≥ 0.4: Moderate species evenness
3. E < 0.4: Low species evenness

Dominance Index

The dominance index is closely related to Simpson's index, reflecting the probability that two randomly chosen individuals belong to the same taxon (Hammer et al., 2009). The calculation of the dominance index uses Simpson's dominance index, range from 0 (all taxa are equally present) to 1 (one taxon dominates the community completely):

$$D = \Sigma_i[\frac{ni}{N}]^2 \quad (7)$$

Where:
D = Dominance index
ni = Number of individuals of genus i
N = Total number of individuals

With C evaluated based on the following criteria (Odum, 1996 in Munthe et al., 2011):

1. 0 < C < 0.5: No dominant genus (low)
2. 0.5 < C < 1: Presence of a dominant genus (high)

Clustering

Foraminiferal biozonation was carried out using cluster analysis with the hierarchical single linkage method and the Euclidean similarity index, through the PAST application. Indicator species reflecting certain environmental conditions were determined based on the formula by Dufrêne & Legendre (1977):

IndVal= A_ij B_ij×100(8)

Where:

A_ij = ⟦Nindividuals⟧_ij/⟦Nindividuals⟧_i

B_ij = ⟦Nsites⟧_ij/⟦Nsites⟧_i

With the following explanation:

⟦Nindividuals⟧_ij = mean abundance of species/ genus j in cluster i

⟦Nindividuals⟧_i = total mean abundance of all species/genera in cluster i

⟦Nsites⟧_ij = number of sites in cluster i where species/genus j occurs

⟦Nsites⟧_i = total number of sites in cluster i

The determination of sediment type from the collected samples was carried out using grain size analysis with the Particle Size Analyzer (PSA) method, employing a Malvern Mastersizer 3000, available at the laboratory of Marine Geological Institute (MGI), Geological Agency, Ministry of Energy and Mineral Research of Indonesia, to obtain the grain size distribution of each sample. The results of the grain size distribution obtained from the Particle Size Analyzer (PSA) method were then analyzed using the GRADISTAT v9.1 application, developed by Blott and Pye (2001). For the intensity of bottom current estimation, we considered only silt sediment type (10-63 μm size fraction), by calculating it's sortable silt mean size ($\overline{ss}$), that were translated into bottom current intensity following the equation of Ledbetter (1986). According to McCave et al. (1995), this silt size fraction reflects the bottom current intensity better, because it is not influenced by surface currents dynamics, and is non-cohesive. Bottom currents generally rarely move sand fractions (>63 μm in size), while sediment fraction <10 μm tends to be cohesive. The detailed grain size preparation and analysis have been described in Putri (2023).

The age estimation of the GM3-2018-WPG.04 sediment core, was reconstructed by using the MD012382 sediment core studied by Maryunani (2009) as a reference (Figure 1), also has been described in Putri (2023). The determination of the GM3-2018-WPG.04 sediment age was obtained from the correlation between the mean size sortable silt pattern of GM3-2018-WPG.04 and the abundance of *Cibicides* spp (benthic microfauna influenced by bottom current) from the MD012382 sediment core (Maryunani, 2009).

RESULTS

Sediment Core Description of Site GM3-2018-WPG.04

The sediment core description shows no lithological changes. The core is dominated by dark gray silt with a uniform texture and the presence of bioturbation structures. This indicates that the sediments were deposited in a deep-sea environment with low depositional energy. The description of core GM3-2018-WPG.04 is summarized in the lithological column shown in Figure 3.

Grain size

The grain size analysis using the GRADISTAT v9.1 application also shows that the largest fraction in the GM3-2018-WPG.04 samples is silt, with all samples ranging from 53.6% to 90.0%. Some samples contain sand (6.2–44.5%), while a small portion contains clay (1.5–4.3%). Therefore, this study uses silt-sized sediments. The sediment types, based on the classification of Blott and Pye (2001), are presented in Table 1.

The mean grain size of the sediment at the bottom of the core shows relatively finer material (medium silt), then becomes coarser (coarse silt–very coarse silt) in the 120–40 cm interval, and returns to finer material (medium silt) at the top of the core (Figure 4). Afterwards, we calculated the mean size of sortable silt fraction ($\overline{\mathbf{SS}}$) to identify the bottom current variability. The ($\overline{\mathbf{SS}}$) value was then translated into deep-sea current velocity following the calculation of Ledbetter (1986), yielding values ranging from a minimum of 33.8 cm/s at a core depth of 130 cm to a maximum of 49 cm/s at a depth of 40 cm (Figure 5 and Table 2).

Darmawan et al. (2021) stated that at 50-1000 m water depth of the northern Papua flows an undercurrent water (New Guinea Coastal Undercurrent - NGCUC). Previous research on the NGCUC was conducted by Lindstrom et al. (1987) and Kuroda et al. (2000) in the waters of Papua New Guinea. According to Lindstrom et al. (1987), the current velocity of NGCUC is around 50 cm/s, while according to Kuroda et al. (2000), the average speed of NGCUC in northern Papua New Guinea is 54 cm/ s with a standard deviation of 15 cm/s. These finding suggest that our bottom current velocity estimation in this study are not very different compared to those two previous studies.

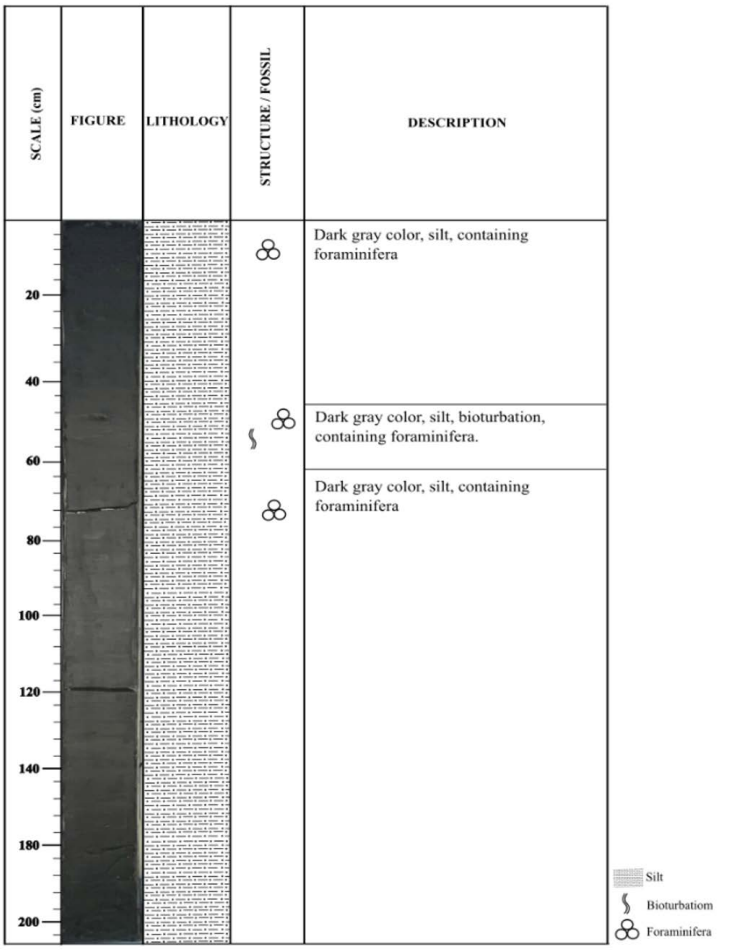

Figure 3. Lithological column of sediment core GM3-2018-WPG.04

Table 1. Sediment classification of sample GM3-2018-WPG.04

Depth of Layer Sediment Core (cm)	Sediment Classification
0	medium silt
10	medium silt
20	medium silt
30	medium silt
40	very coarse silt
50	medium silt
60	coarse silt
70	coarse silt
80	coarse silt
90	coarse silt
100	coarse silt
110	coarse silt
120	coarse silt
130	medium silt
140	medium silt
150	medium silt
160	medium silt
170	medium silt
180	medium silt
190	medium silt

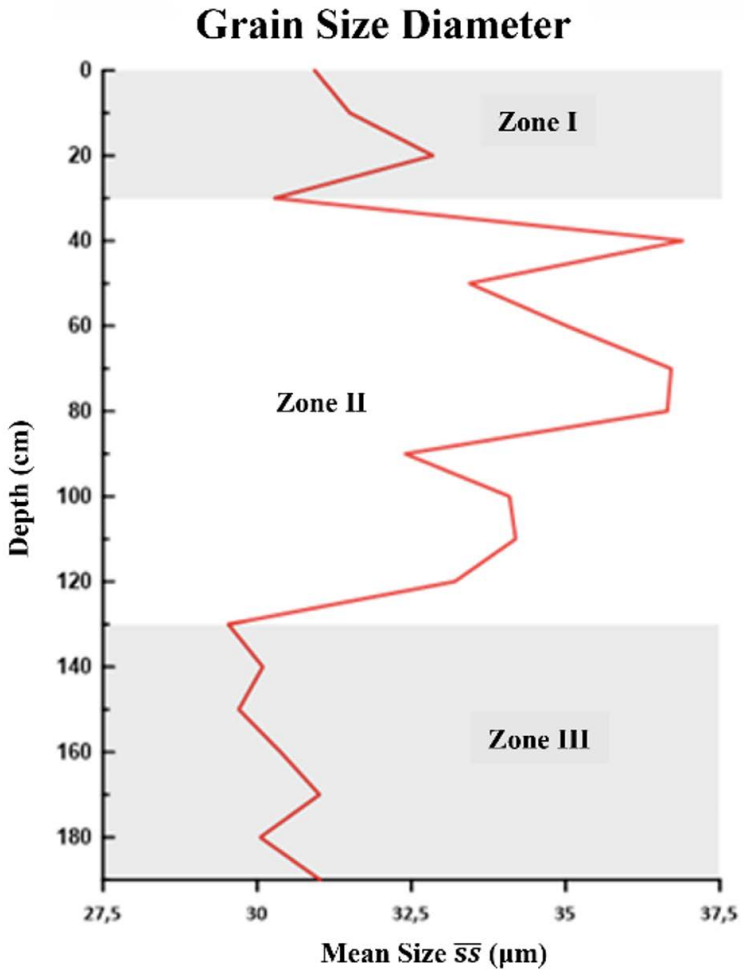

Figure 4. Mean grain size diameter of sediment core GM3-2018-WPG.04 (µm)

Table 2. Velocity of bottom current translated from the sortable silt mean size ($\overline{ss}$) value (Ledbetter, 1986)

Depth Intervals (cm)	Mean size of Sortable Silt (µm)	Bottom Current of Ledbetter (1986) (cm/s)
0	30,930	36,72994
10	31,50	37,903
20	32,85	40,6813
30	30,28	35,39224
40	36,90	49,0162
50	33,44	41,89552
60	35,02	45,14716
70	36,71	48,62518
80	36,65	48,5017
90	32,40	39,7552
100	34,09	43,23322
110	34,19	43,43902
120	33,20	41,4016
130	29,53	33,84874
140	30,09	35,00122
150	29,70	34,1986
160	30,38	35,59804
170	31,01	36,89458
180	30,05	34,9189
190	31,02	36,91516

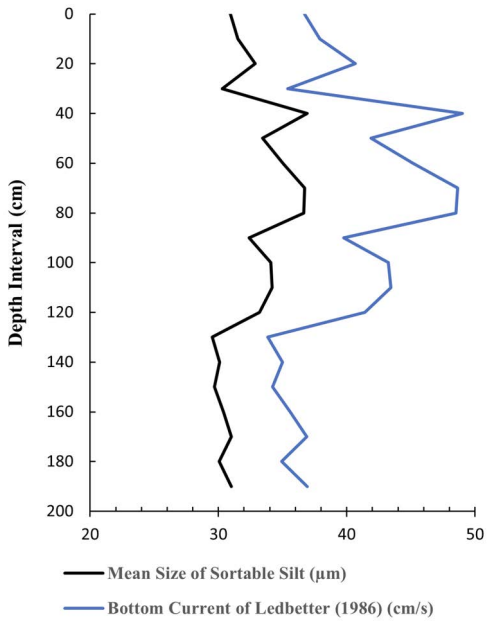

Figure 5. Fluctuations of mean size of sortable silt and estimated deep-sea current velocity based on Ledbetter's (1986) equation

Foraminifera in Waipoga Waters

Foraminiferal Distribution and P/B Ratio

Foraminifera in sample GM3-2018-WPG.04 were found throughout the sediment core intervals and exhibited good preservation conditions, such as intact shells with no discoloration. Based on the identification results, the foraminifera in the study area consist of 12 planktonic genera with 22 species and 41 benthic genera with 61 species, with varying abundances at different depths. The abundance of planktonic foraminifera was more dominant compared to benthic foraminifera. In the analysis of 20 sediment samples, the total number of planktonic individuals was 818200, while the number of benthic individuals was 114000.

Planktonic Foraminifera

In the Waipoga waters sediment samples, planktonic foraminifera species were found in abundant numbers at all depths (Figure 6), with *Globigerinoides ruber* being the most dominant species (41.7%). The abundance of *G. ruber* indicates that the waters at the study site had warm surface temperatures and oligotrophic conditions (low nutrient content). This species is generally found above the thermocline (within the mixed layer) and is associated with low-productivity environments (Fairbanks et al., 1982; Troelstra and Kroon, 1989).

In addition to *G. ruber*, the species *G. immaturus* (6.7%) was also found in abundance across all depths. This finding emphasize the indication that the study area represents warm waters with low productivity levels. However, unlike *G. ruber*, *G. immaturus* is more common found in waters with higher salinity.

Other planktonic foraminifera found in high abundance and present at all sampled depths in Waipoga waters include *Neogloboquadrina incompta* (13.2%), *Neogloboquadrina dutertrei* (11%), *Hastigerina pelagica* (6.65%), and *Globigerinoides immaturus*. *Neogloboquadrina dutertrei* and *Neogloboquadrina incompta* are species abundant above the pycnocline, preferring warmer and shallower surface waters, as well as eutrophic (nutrient-rich) environments, often associated with upwelling events (Curry et al., 1983; Fairbanks et al., 1982; Ortiz et al., 1995; Cannariato and Ravelo, 1997; Kawahata et al., 2002; Kuroyanagi and Kawahata, 2004). *Hastigerina pelagica* generally inhabits warm, shallow waters with high salinity (Bé and Hutson, 1977).

The species *Pulleniatina obliquiloculata* (4%) was also found in considerable abundance at several depths. This species is known to commonly live within the thermocline layer and prefers eutrophic conditions, often associated with upwelling processes(Ravelo et al., 1990; Baohua et al., 1997; Pflaumann and Jian, 1999).

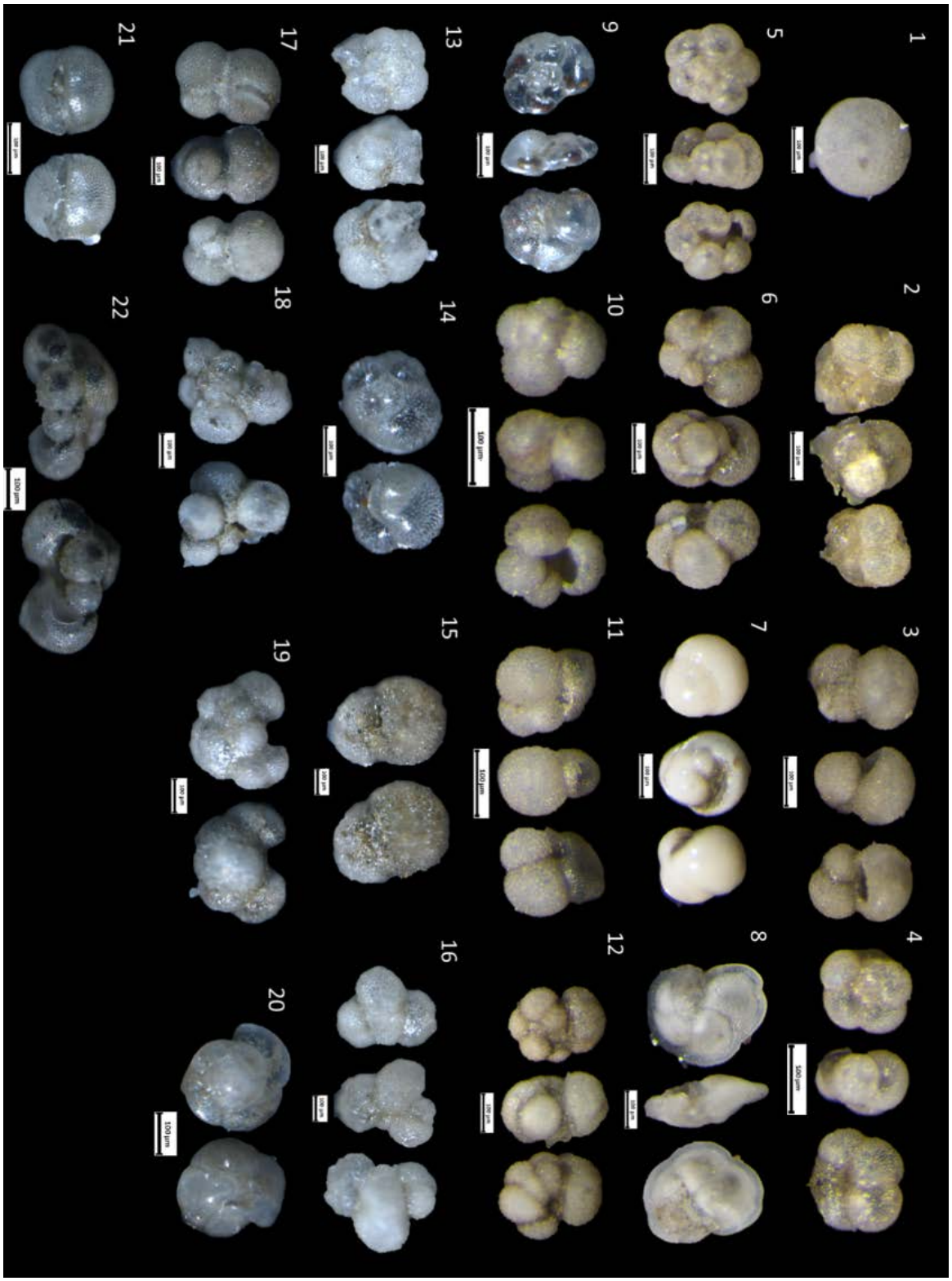

Figure 6. The planktonic foraminifera identified in this study are: (1) *Orbulina universa*, (2) *Tinophodella ambitacrena*, (3) *Globigerinoides ruber*, (4) *Neogloboquadrina incompta*, (5) *Neogloboquadrina dutertrei*, (6) *Hastigerina pelagica*, (7) *Pulleniatina obliquiloculata*, (8) *Globorotalia tumida*, (9) *Globorotalia wilesi*, (10) *Globigerina bulloides*, (11) *Globigerinoides sacculiferus*, (12) *Alloglobigerinoides conglobatus*, (13) *Neogloboquadrina* sp., (14) *Globigerinita uvula*, (15) *Globigerinoides trilobus*, (16) *planktonik unidentify*, (17) *Globigerinoides immaturus*, (18) *Hastigerinella* sp., (19) *planktonik unidentify* (1), (20) *Globorotalia hirsuta*, (21) *Sphaeroidinella excavata*, dan (22) *Neogloboquadrina blowi*.

Benthic Foraminifera

Benthic foraminifera were found in relatively smaller numbers compared to planktonic foraminifera. However, their diversity was higher than that of planktonic species. The most abundant benthic foraminifera identified in the study area include *Bulimina marginata* (1.8%), *Cibicidoides pachyderma* (1.89%), and *Lenticulina calcar* (1.3%) (Figures 7 and 8).

Bulimina marginata is known as a species adapted to low-oxygen (dysoxic) conditions, commonly associated with upwelling processes and high organic carbon content in the seafloor sediments (Rathburn et al., 1996; Martins et al., 2015). *Cibicidoides pachyderma* is considered an indicator species of environments with strong bottom currents. It can inhabit both eutrophic and oligotrophic settings. In oligotrophic conditions, *C. pachyderma* tends to live shallower within the sediments, while in eutrophic conditions, it can burrow deeper (Wollenburg et al., 2018). *Lenticulina calcar* is recognized as a species that thrives in environments with intermediate oxygen levels (suboxic conditions) (Kaiho, 1994).

From the planktonic and benthic foraminifera species, it can be inferred that, in addition to variations in productivity, the study area also experiences fluctuations in salinity and nutrient availability, which may influence the distribution of foraminifera species.

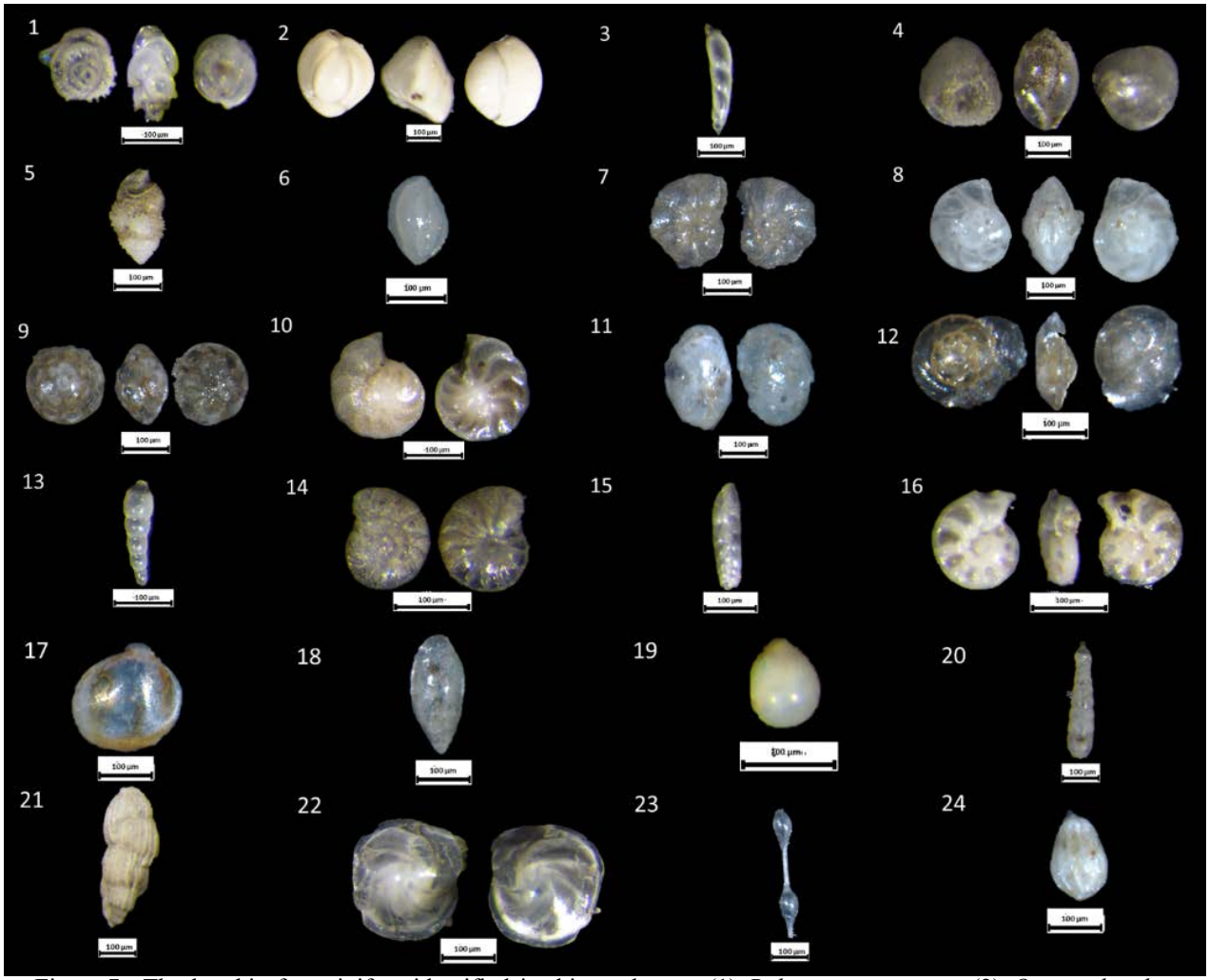

Figure 7. The benthic foraminifera identified in this study are: (1) *Bulimina marginata,* (2) *Quinqueloculina seminulum,* (3) *Enantiodentalina timorensis,* (4) *Praeglobobulimina spinescens,* (5) *Uvigerina proboscidea,* (6) *Quinqueloculina* sp., (7) *Hyalinea balthica,* (8) *Lenticulina lamarck,* (9) *Ammonia* sp., (10) *Cibicidoides pachyderma,* (11) *Globocassidulina subglobosa,* (12) *Epistominella exigua,* (13) *Laevindentalina* sp., (14) *Cibicidoides alazanensis,* (15) *Bolivina spathulata,* (16) *Hyalinea florenceae,* (17) *Parafissurina subventricosa,* (18) *Oolina baukalionilla,* (19) *Triloculina triquetrella,* (20) *Laevidentalina translucens,* (21) *Euuvigerina reineri,* (22) *Lenticulina calcar,* (23) *Grigelis orectus,* (24) *Oolina portseaensis*

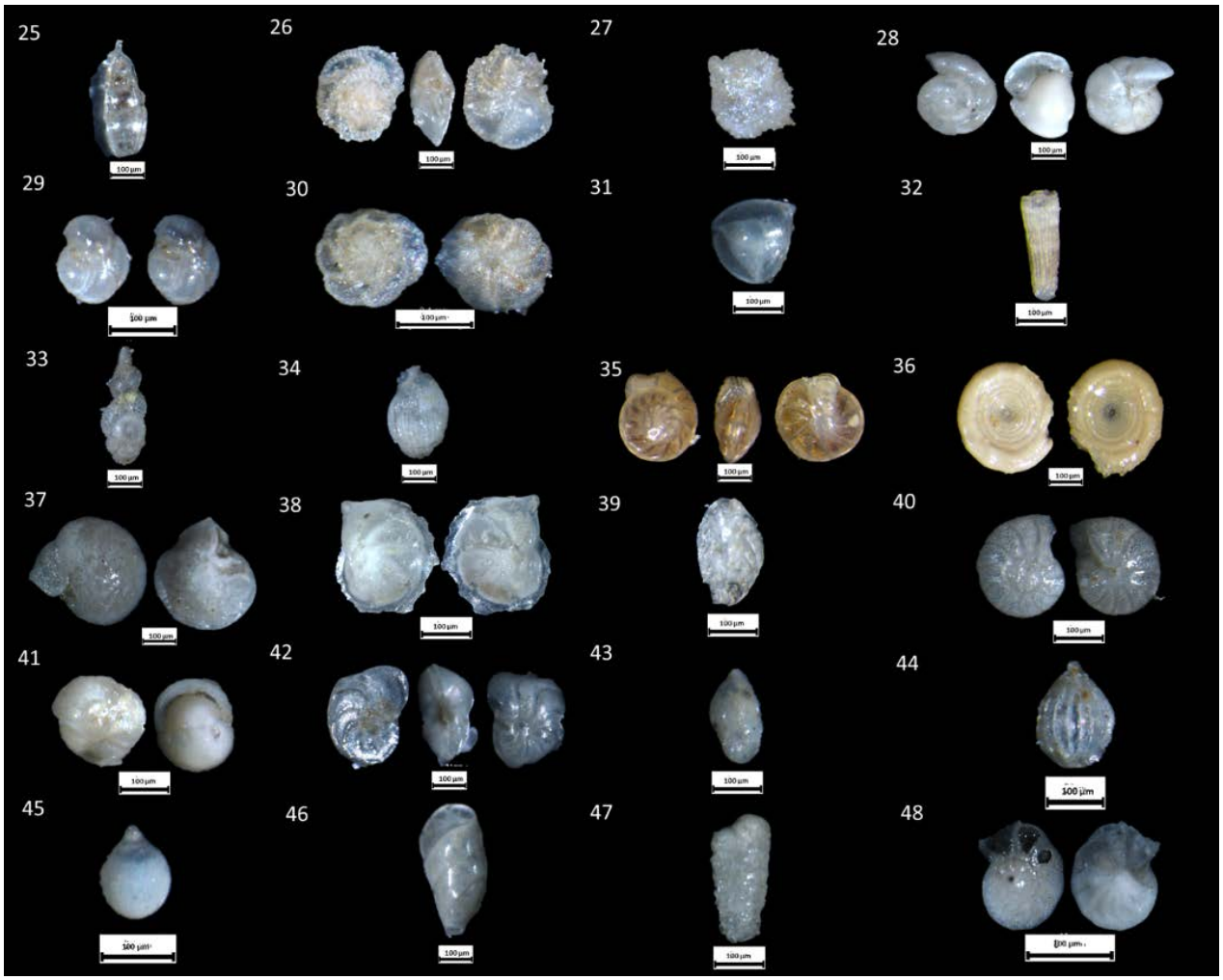

Figure 8. The benthic foraminifera identified in this study are: (25) *Bolivinita quadrilatera*, (26) *Siphonina australis*, (27) *Uvigerina aculeata*, (28) *Gyroidina soldanii*, (29) *Hansenisca soldanii*, (30) *Osangulariellodes rugosus*, (31) *Neolenticulina peregrina*, (32) *Siphogenerina* sp., (33) *Neouvigerina ampullacea*, (34) *Uvigerina dirupta*, (35) *Hoeglundina elegans*, (36) *Ammodiscus intermedius*, (37) *Heterolepa praecincta*, (38) *Lenticulina* sp., (39) *Bolivina vadescens*, (40) *Hanzawaia concentrica*, (41) *Pullenia bikiniensis*, (42) *Discorbinella bertheloti*, (43) *Pyrulina cylindroides*, (44) *Lagena sulcata*, (45) *Reussoolina stellula*, (46) *Laevidentalina antartica*, (47) *Siphotextularia concava*, (48) *Cibicides* sp.

The average P/B ratio across all depths is 87.7%, with values ranging from 77.8% to 94.6% (Figure 9). A high P/B ratio indicates that the study area is dominated by planktonic foraminifera, with only a small proportion of benthic foraminifera at each depth. Based on the P/B ratio results, the study area can be classified as an upper bathyal environment, with all sediment samples representing depths greater than 200 m (the core samples were taken from a depth of 462 m). However, within the depth intervals of 20–22 cm to 2–4 cm, the P/B ratio values show a decrease compared to other depth intervals.

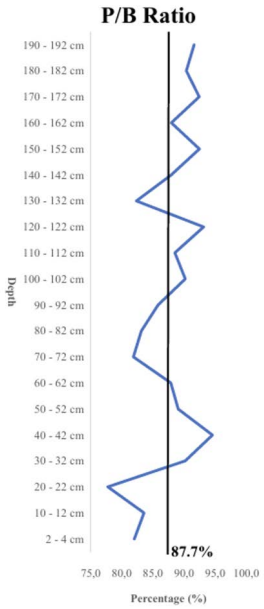

Figure 9. P/B Ratio Graph

Ecological Indices

The foraminiferal diversity index in all sediment samples from Waipoga waters ranges between 1.702 and 2.284, which falls into the moderate category. This indicates a fairly good species diversity and a relatively stable ecosystem, although still experiencing moderate ecological stress. The evenness index ranges from 0.2462 to 0.4318, indicating low to moderate evenness, where the distribution of individuals among species is not uniform. Meanwhile, the dominance index is relatively low, ranging from 0.1662 to 0.3209, suggesting that no single species strongly dominates the foraminiferal community in the sediment samples from the study area (Figure 10).

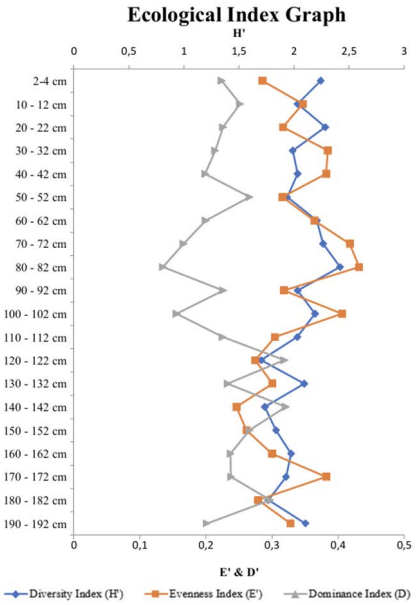

Figure 10. Ecological Index Graph

Cluster

Cluster analysis was conducted to group each depth based on the similarity of foraminiferal composition. The clustering results were grouped using a distance value of 20,000. This distance index value was chosen because it represents the distribution of foraminifera based on ecological similarity. The dendrogram results (Figure 11) show that the samples are divided into six main zones, reflecting changes in foraminiferal communities.

In each zone, the species *Globigerinoides ruber* is highly abundant; therefore, this species is not a major factor in cluster formation. Instead, species with more significant fluctuations in abundance, such as *Neogloboquadrina dutertrei*, *Hastigerina pelagica*, *Neogloboquadrina incompta*, and *Globigerinoides immaturus*, play a greater role in distinguishing between zones.

Zone 1 (190–192 cm)

Zone 1 is characterized by an average foraminiferal abundance of around 300 specimens/g. The dominant species are *Neogloboquadrina dutertrei* (15.35%), *Globigerinoides immaturus* (12.87%), and *Hastigerina pelagica* (8.13%), indicating that the waters in this zone were deposited under relatively deep thermocline conditions, warm, and oligotrophic. The abundance of *N. dutertrei* suggests that this zone may be associated with a stable thermocline layer, while *G. immaturus* reflects waters with low nutrient content and high oxygen levels (oxic).

Zone 2 (150-182 cm)

Zone 2 shows an increase in *Neogloboquadrina incompta* (14.18%), with a decrease in *Globigerinoides immaturus* (7.83%) and *N. dutertrei* (9.41%). *Cibicidoides pachyderma* (1.69%) increased compared to Zone 1 (0.90%); this species is typically found in environments with stronger currents and can adapt to both oligotrophic and eutrophic conditions. *Lenticulina calcar* (2.54%) also increased, indicating suboxic conditions. These increases may suggest enhanced ocean currents and nutrient input, resulting in more eutrophic conditions with intermediate oxygen levels (suboxic).

Zone 3 (110-142 cm)

This zone is marked by the dominance of *Neogloboquadrina incompta* (16.8%), which further increased compared to the previous zone, along with decreases in *Globigerinoides immaturus* (5.83%) and *H. pelagica* (5.03%). The high abundance of *N. incompta* indicates more eutrophic conditions and an increase in nutrient supply, which may be related to changes in thermocline stability

Zone 4 (100-102 cm)

This zone is dominated by *Pulleniatina obliquiloculata* (16.3%), *Neogloboquadrina dutertrei* (14.67%), and *Globigerinoides immaturus* (13.59%), with a decrease in *Cibicidoides pachyderma* (0.54%). *Globigerinoides ruber* shows a drastic decline in this zone, which may indicate disruption in surface water stability and cooler conditions. The increase in *P. obliquiloculata*, typically associated with the thermocline and eutrophic conditions, suggests the possibility of a shallower thermocline, potentially linked to

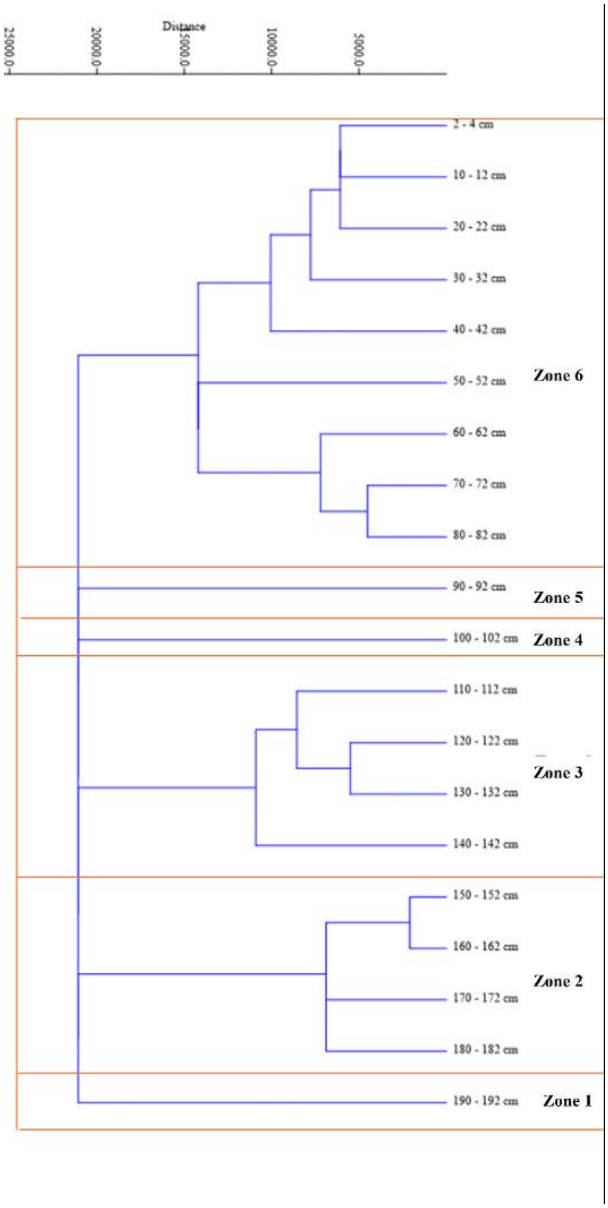

Figure 11. Dendrogram of foraminifera abundance cluster analysis

upwelling events, though further confirmation is needed.

Zone 5 (90-92 cm)

This zone is dominated by *Neogloboquadrina incompta* (12.93%), *Hastigerina pelagica* (10.17%), *Bulimina marginata* (3.67%), and *Cibicidoides pachyderma* (2.82%). Meanwhile, *N. dutertrei* (6.5%), *Pulleniatina obliquiloculata* (5.93%), and *Globigerinoides immaturus* (5.65%) declined. The increase in *Bulimina marginata* indicates low oxygen levels (dysoxic). *Globigerinoides ruber* rebounded after its previous decline in Zone 4, suggesting a return to warmer conditions and a deeper thermocline following a possible earlier upwelling event.

Zone 6 (2-82 cm)

This zone is still dominated by *Neogloboquadrina incompta* (11.93%) and *Neogloboquadrina dutertrei* (12.63%), indicating eutrophic conditions and warm waters. The decrease in *H. pelagica* (6.23%) may suggest a shift toward lower salinity conditions compared to the previous zone.

Age Reconstruction of The Sediment Core

According to Maryunani (2009) study, the abundance of *Cibicides* spp. in sediment core MD012382, which was also collected from Waipoga waters (Figure 1), served as a proxy for bottom ocean current velocity. This was then correlated with the sortable silt mean size from the core in this study,

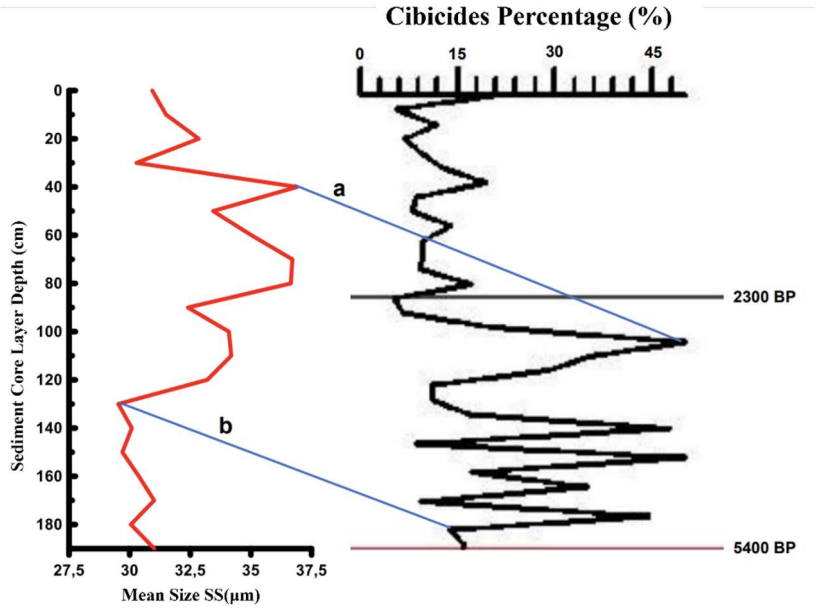

Figure 12. Age model reconstruction by correlated mean size sortable silt of GM3-2018-WPG.04 sediment core to the *Cibicides* spp. assemblages of the MD012382 (Putri, 2023).

Table 3. Age model reconstruction

Depth Interval (cm)	Age (yr BP)
40	3170
60	3651
80	4133
100	4614
120	5095
130	5336

which also reflects bottom current velocity. The sediment core MD012382 already has absolute age constraints, as radiocarbon dating and Pb-210 analyses were conducted on that core. Therefore, when correlating the abundance of *Cibicides* spp. in core MD012382 with the mean size sortable silt in this study's core, the correlated intervals can be considered to represent the same age. Derived from age model reconstruction in Figure 12, we can suggest that the interval depth of 40 cm, which has a maximum average sortable silt grain size (36.9 µm), which occurs just after a minimum value in the deeper (older) interval, and then decreases sharply afterwards, associated with the age of 3170 yr BP of the MD012382, which characterized by maximum abundance of the *Cibicides* group (> 45% in average), which also occurs after a minimum abundance at an older age, and abruptly decrease again afterwards. Another interval that can be associated and considered as a tie point is the 130 cm depth interval of GM3-2018-WPG.04, correlated to the age of 5336 Yr BP of the MD012382. This interval is characterized by relatively low value of mean size sortable silt and low abundances of *Cibicides* group. These two tie points will later be used as the basis for age modeling through interpolation and extrapolation, which is presented in Table 3. Based on the age model reconstruction, the age of this studied core can be inferred to fall within the Middle to Late Holocene. The more detailed of this age reconstruction method has been described by Putri (2023).

DISCUSSION

Several oceanographic parameters can be interpreted from the assemblage of foraminifera found in the sediment core from Waipoga waters. The P/B ratio indicates an upper bathyal environment; however, in the depth interval between 20–22 cm and 2–4 cm, there is a relative decrease in the P/B ratio. Thermocline variability can be interpreted from the group of thermocline-dwelling planktonic foraminifera, such as *Neogloboquadrina blowi*,

Neogloboquadrina incompta, *Neogloboquadrina eggeri*, *Neogloboquadrina* sp., and *Pulleniatina obliquiloculata*. These species inhabit the thermocline layer, so variations in their abundance indicate changes in thermocline depth and productivity levels, which may be linked to the influence of upwelling that lead to the more productive Waipoga waters. Another parameter observed is the oxygenation level of the seafloor, inferred from benthic foraminifera that characterize dysoxic conditions, such as *Bulimina* spp., *Ceratobulimina* spp., *Uvigerina* spp., and *Bolivina* spp. In addition, *Globigerinoides ruber* is also observed due to its highest abundance compared to other planktonic species. *G. ruber* serves as an indicator of warm and oligotrophic surface ocean conditions. These oceanographic proxy parameters were then compared with element ratio data as well as silt grain-size data, as presented in Figure 13.

The variability in sortable mean size ($\overline{ss}$) can reflect changes in bottom current energy related to the Indonesian Throughflow (ITF), with each zone representing different bottom current conditions. That study identified three distinct zones based on this mean of sediment grain size. In Zone III, at the depths interval of 190–130 cm (the deepest/oldest interval), the sediments are relatively finer (medium silt). In Zone II, sediments become coarser (coarse silt–very coarse silt) between 120–40 cm. Finally, sediments return to finer (medium silt) in Zone I, at 30–0 cm. In this study, the *Cibicides* group was combined with the *Cibicidoides* group, which shares the same ecological characteristics. This includes species such as *Cibicidoides pachyderma*, *Cibicidoides alazanensis*, *Cibicidoides pseudoungerianus*, *Cibicidoides mundulus*, *Cibicides refulgens*, and *Cibicides* sp. *Cibicidoides* and *Cibicides* are benthic foraminifera that characterize high-energy marine environments influenced by strong currents (Pérez et al., 2024). The *Cibicides* and *Cibicidoides* groups were then correlated with foraminiferal parameters such as the P/B ratio, ecological index, the abundance of thermocline dwellers, dysoxic groups, and *G. ruber*.

Zone III (depth interval 190–130 cm; 5653–5336 yrs BP) is characterized by relatively finer silt-sized sediments (medium silt) compared to the younger Zone II, reflecting lower bottom current energy. This interpretation is supported by the lower abundance of *Cibicides* and *Cibicidoides* groups—indicators of high-energy bottom environments—as well as by the reduced occurrence of dysoxic taxa, suggesting better-oxygenated (suboxic) conditions. Ecological indices support this; the diversity index and evenness are lower in Zone III than in Zone II, indicating that species were less evenly distributed, while dominance values are higher, suggesting that a few species dominated the assemblage. In contrast, dominance values are higher, indicating that a few species contributed significantly more to the assemblage. Furthermore, the decreased abundance of thermocline dwellers indicates a deeper thermocline layer and lower nutrient availability. This is also consistent with the relatively higher proportion of *G. ruber*, a species that thrives in oligotrophic conditions, where higher abundances reflect lower nutrient levels. The cluster analysis also supports this interpretation, grouping Zone III within clusters that represent a deep thermocline, warm temperatures, and low to moderate nutrient levels. In addition, the relatively higher P/B ratio in this zone indicates an increase in water depth. Altogether, these conditions suggest a weakening of bottom current circulation and a deepening of the thermocline, likely linked to enhanced precipitation and subsequent sea-level rise. A deeper thermocline further reflects warmer, oligotrophic surface waters, in agreement with the observed increase in *G. ruber*.

In contrast, Zone II (depth interval 120–40 cm; 5095–3170 yrs BP) is characterized by coarser grain sizes (coarse–very coarse silt), indicating stronger bottom current energy, which is also supported by a slight increase in the ln(Zr/Rb) ratio (a grain-size proxy). This is accompanied by an increase in the *Cibicides* and *Cibicidoides* groups, which reflect high-energy, more oxygen-demanding (dysoxic to oxic) bottom-water environments. The ecological indices also confirm these conditions, as diversity and evenness reach their highest values in this interval, while dominance is lowest, suggesting a more balanced and diverse foraminiferal community supported by stronger circulation and nutrient availability. The increased abundance of *Cibicides* and *Cibicidoides* indicates that Zone II represents a dynamic setting, with oxygen levels beginning to decline. In addition, the higher abundance of thermocline dwellers suggests a shallower thermocline, often associated with upwelling that enhances nutrient supply, or possibly linked to stronger bottom currents transporting nutrients upward. Cluster analysis places Zone II within clusters 3, 4, and 5, which depict conditions of elevated nutrient availability and thermocline instability. This interpretation is further supported by the decreased abundance of *G. ruber*, a warm-water oligotrophic indicator species, confirming a shift

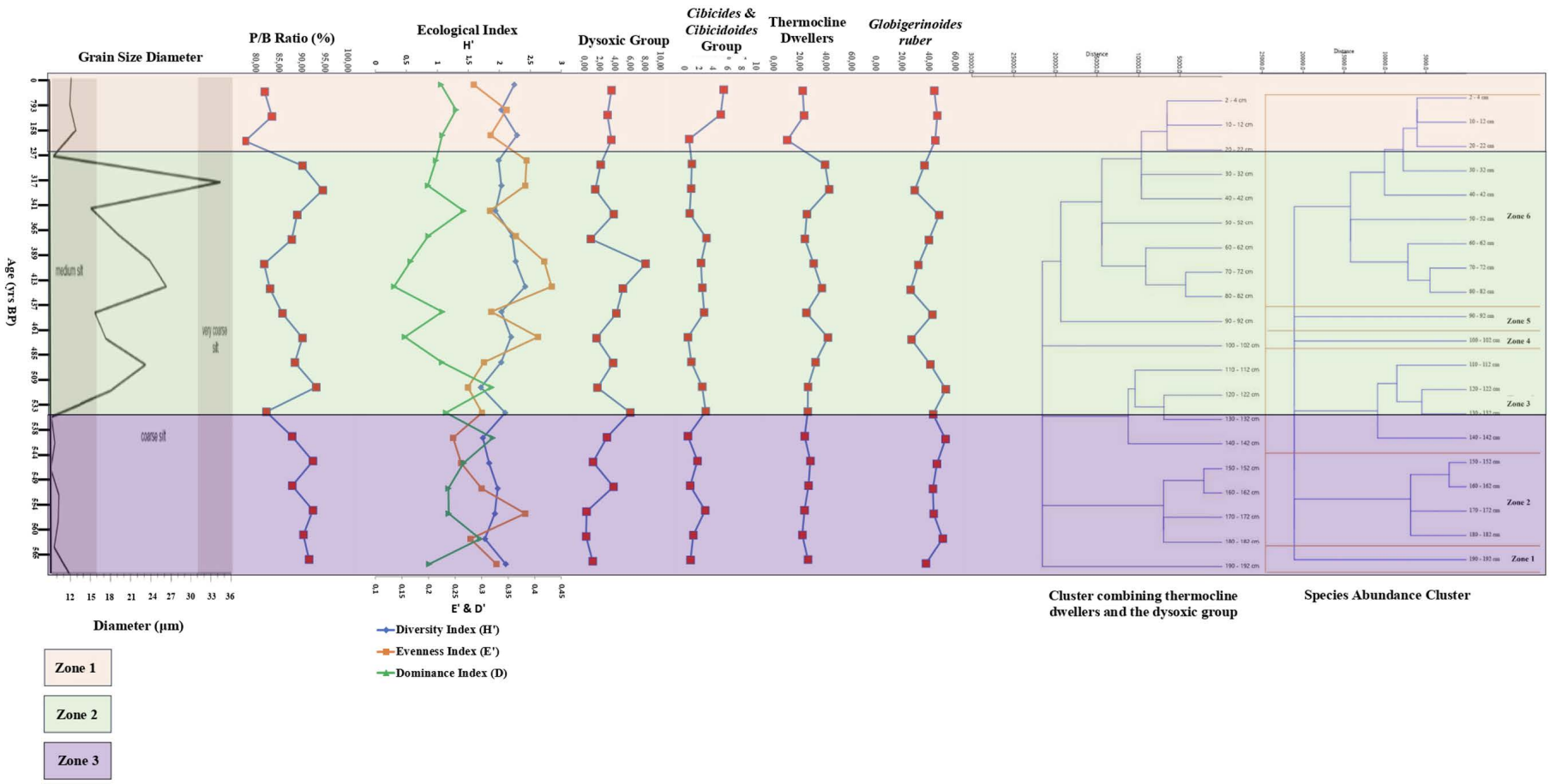

Figure 13. Correlation of the dendrogram of foraminiferal abundance cluster analysis and the combined cluster of thermocline dwellers and the dysoxic group with the grain size diameter graph, P/B ratio (%), ecological index, thermocline dwellers, dysoxic group, as well as the *Cibicides* and *Cibicidoides* groups.

toward more eutrophic conditions during this interval. Meanwhile, the increased abundance of dysoxic benthic foraminifera indicates a reduction in bottom-water oxygenation to dysoxic levels. Overall, Zone II reflects an intensification of bottom current circulation, which likely contributed to enhanced productivity, both through upwelling processes and through stronger current activity. This interpretation is consistent with the maximum current velocity of ~49 cm/s recorded at a depth of 40 cm, dated to approximately 3170 yrs BP. This period correlates with Zone II in this study, which indicates intensified ocean circulation and higher productivity. The increased abundance of *Cibicides* and *Cibicidoides*, as indicators of high-energy and dysoxic environments, also aligns with stronger deep-ocean circulation and with the increased frequency of El Niño-like events during the Middle Holocene (Maryunani, 2009). These phenomena likely contributed to a shallower thermocline and enhanced upwelling in Waipoga waters, as further reflected in the higher abundance of thermocline dwellers in this study.

In Zone I (depth interval 30–0 cm; 2378–0 yrs BP), the silt grain size becomes finer again (medium silt), similar to the conditions observed in Zone III. This indicates a weakening of bottom current energy. Ecological indices also reflect this transition, diversity and evenness decrease compared to Zone II, while dominance increases, suggesting that the community became less diverse and less evenly distributed, with certain species becoming more dominant. In addition, the abundance of thermocline dwellers decreases, suggesting a deepening of the thermocline. Based on the cluster results, this interval falls into Zone 6, which characterizes warm, eutrophic surface-water conditions with lower salinity and a relatively more stable environment. On the other hand, *G. ruber* once again shows relatively high abundance, indicating warmer and oligotrophic surface-water conditions. The abundance of dysoxic benthic foraminifera decreases, suggesting that bottom-water oxygenation increased, returning toward suboxic conditions. Zone I therefore, reflects a transitional phase into a more stable environment, with reduced current energy and weakened bottom-water circulation, implying that the inflow of ITF into Indonesian waters also diminished. Furthermore, the decrease in dysoxic taxa supports the interpretation that oxygen conditions improved, becoming more suboxic.

This indicates that deep-sea/bottom-water dynamics (which constitute the source of ITF entering Indonesian waters) exert a strong influence on foraminiferal abundance. The circulation of Southern Ocean bottom waters, as the source of ITF, is considered to significantly affect the oceanographic conditions in Waipoga waters, including the distribution and abundance of foraminiferal communities.

CONCLUSSIONS

Based on the study conducted to reconstruct past ocean productivity using foraminiferal distribution from sediment core GM3-2018-WPG.04, several conclusions can be drawn as follows:

1. Sediment sample analysis from Waipoga waters, North Papua, revealed various species of planktonic and benthic foraminifera. The dominant planktonic species are *Globigerinoides ruber*, *Neogloboquadrina dutertrei*, *Neogloboquadrina incompta*, *Pulleniatina obliquiloculata*, *Hastigerina pelagica*, and *Globigerinoides immaturus*. The dominant benthic species include *Bulimina marginata*, *Cibicidoides pachyderma*, and *Lenticulina calcar*. Planktonic foraminifera are more dominant, as the study site is located in a deep-sea (bathyal) zone.

2. The distribution of foraminifera in Waipoga waters during the late Middle to Late Holocene was strongly influenced by bottom-water circulation dynamics (the source of ITF), which affected thermocline stability, nutrient levels, and oxygenation. Zones III and I reflect oligotrophic and suboxic conditions with weakened bottom-water circulation, while Zone II represents an intensification of bottom-water currents, higher nutrient levels and productivity, as well as more dysoxic conditions, likely related to upwelling events. Deep-ocean circulation in the Southern Hemisphere, which serves as the source of ITF, exerts a significant influence on the abundance and composition of foraminifera in eastern Indonesian waters.

ACKNOWLEDGEMENTS

The author would like to express gratitude to the Head of BBSPGL or Marine Geological Institue (MGI), Geological Agency, Ministry of Energy, and Mineral Resources of Indonesia, for granting permission to conduct research at the MGI. Sincere thanks are also extended to all team members of Waipoga Cruise, the captain of the Geomarine III

vessel of MGI, and the ship's crew for their support during the survey and sample collection in Waipoga waters, which greatly contributed to the smooth progress of this research. Appreciation is also given to the MGI laboratory staff for their assistance and guidance throughout the laboratory work.

REFERENCES

Ardi, R.D.W., Maryunani, K.A., Yulianto, E., Putra, P.S., Nugroho, S.H., 2019. Biostratigrafi dan Analisis Perubahan Kedalaman Termoklin di Lepas Pantai Barat Daya Sumba Sejak Pleistosen Akhir Berdasarkan Kumpulan Foraminifera Planktonik. *Bulletin of Geology*, 3(2): 355–362. https://doi.org/10.5614/bull.geol.2019.3.2.3

Ashok, K., Yamagata, T., 2009. Climate change: The El Niño with a difference. *Nature*, 461(7263): 481-484. https://doi.org/10.1038/461481a

Azis, M.F., 2006. Gerak Air di Laut. *Oseana*, Vol. 31, no. 4. pp 9-21.

Baohua, L., Zhimin, J., Pinxian, W., 1997. *Pulleniatina obliquiloculata* as a paleoceanographic indicator in the southern Okinawa Trough during the last 20,000 years. *Marine Micropaleontology*, 32, 59-69.

Bé, A.W.H., Hutson, W.H., 1977. Ecology of Planktonic Foraminifera and Biogeographic Patterns of Life and Fossil Assemblages in the Indian Ocean. *Micropaleontology,* 369-414.

Blott, S.J., Pye, K., 2001. Gradistat: A Grain Size Distribution and Statistics Package for The Analysis of Unconsolidated Sediment. *Earth Surface Processes and Landforms*, 26: 1237–1248.

Boltovskoy, E., Wright, R., 1976. *Recent Foraminifera*, Dr. W. Junk, The Hague, Boston, 515p. https://doi.org/10.1007/978-94-017-2860-7

Cannariato, K.G., Ravelo, A.C., 1997. Pliocene–Pleistocene evolution of eastern tropical Pacific surface water circulation and thermocline depth. *Paleoceanography*, 12: 805–820. https://doi.org/10.1029/97PA02514

Curry, W.B., Thunell, R.C., Honjo, S., 1983. Seasonal changes in the isotopic composition of planktonic foraminifera collected in Panama Basin sediment traps. *Earth and Planetary Science Letters*, 64(1), 33-43.

Damanik, A., Maryunani, K.A., Nugroho, S.H., Putra, P.S., 2020. Climate Variability Since Last Glacial Maximum Based on Distribution of Foraminifera in North Papua Waters, Pacific Ocean. *Marine Research in Indonesia*, 45(2): 59–66. https://doi.org/10.14203/mri.v45i2.572

Darmawan, A., Atmadipoera, A.S., Nugroho, D., Kamal, M.M., Koch-Larrouy, A., 2021. Sirkulasi Laut dan Biogeokimia di Kawasan Teluk Cendrawasih. *POSITRON*, 11(2): 63-76. https://doi.org/10.26418/positron.v11i2.46780

Dufrêne, M., Legendre, P., 1977. Species assemblages and indicator species: the need for a flexible asymmetrical approach. *Ecological Monographs*, 67: 345–366.

Fabbrini, A., Greco, M., Iacoviello, F., Kucera, M., Ezard, T.H.G., Wade, B.S., 2023. Bridging the extant and fossil record of planktonic foraminifera: implications for the *Globigerina* lineage. *Palaeontology*, 66(6), e12676. https://doi.org/10.1111/pala.12676

Fairbanks, R.G., Sverdlove, M., Free, R., Wiebe, P.H., Bé, A.W.H., 1982. Vertical Distribution and Isotopic Fractionation of Living Planktonic Foraminifera from the Panama Basin. *Nature*, 298(5877), 841-844.

Grimsdale, T.F., Morkhoven, F.P.C.M.V., 1955. The Ratio Between Pelagic and Benthonic Foraminifera As A Means of Estimating Depth of Deposition of Sedimentary Rocks. *Micropaleontology*, 1: 473–491.

Gustiantini, L., 2018. *Paleoclimate Reconstructions by Multiproxy Approaches in the Halmahera Sea since the Late Pleistocene–Holocene*. Dissertation, Institut Teknologi Bandung, Bandung.

Gustiantini, L., Piranti, S.A., Zuraida, R., Hyun, S., Ranawijaya, D.A.S., Harkinz, F.X., 2018. Foraminiferal Analysis Related to Paleoceanographic Changes of Arafura Sea and Surrounding During Holocene. *Bulletin of the Marine Geology*, 33(2).

Hammer, Ø., Harper, D.A.T., Ryan, P.D., 2001. PAST: Paleontological Statistics Software Package for Education and Data Analysis. *Palaeontologia electronica*, *4*(1), 1.

Hammer, Ø., Harper, D.A.T., Ryan, P.D., 2009. PAST – Palaeontological Statistics, ver. 1.89. *Palaeontologia Electronica*, 12(1): 1–9. https://www.researchgate.net/publication/228393561

Hammer, Ø., 1999-2024. *PAST – PAleontological STatistics. Version 4.17 Reference Manual*. Natural History Museum, University of Oslo.

Hasanudin, O.M., 1998. Arus Lintas Indonesia (ARLINDO). *Oseana*, 23(2), 1-9.

Hemleben, Ch., Spindler, M., Anderson, O.R., 1989. *Modern Planktonic Foraminifera*. Springer Science & Business Media, 363p.

Holbourn, A., Henderson, A.S., MacLeod, N., 2013. *Atlas of Benthic Foraminifera*. John Wiley & Sons, 651p. https://doi.org/10.1002/9781118452493

Jatiningrum, R.S., Mutika, A., Gustiantini, L., Gerhaneu, N.Y., Latuputty, G., Divina, A.R., 2023. Distribution Of Benthic Foraminifera In The Waters From Off Putri Island, Northern Batam, Riau Archipelago. *Bulletin of The Marine Geology*, 37(2). https://doi.org/10.32693/bomg.37.2.2022.783

Junita, D.R., Gustiantini, L., Sartimbul, A., Sahudin, 2020. Study of microfauna foraminifera as bioindicator for coral reef condition in Tambelan Island, Riau Island Province. In *IOP Conference Series: Earth and Environmental Science* (Vol. 429, No. 1, p. 012005). IOP Publishing.

Jurnaliah, L., Muhamadsyah, F., Barkah, M.N., 2017. Lingkungan Pengendapan Formasi Kalibeng Pada Kala Miosen Akhir di Kabupaten Demak Dan Kabupaten Semarang, Jawa Tengah Berdasarkan Rasio Foraminifera Planktonik dan Bentonik (Rasio P/B). *Bulletin of Scientific Contribution*, 14(3): 233-238. https://doi.org/10.24198/bsc.vol14.yr2016.art10965

Jurnaliah, L., Syafri, I., Sudradjat, A., Kapid, R., 2019. Biofasies dan Ekologi Perairan Jawa Tengah Bagian Utara Berdasarkan Kumpulan Foraminifera Bentik Kecil. *Jurnal Geologi Kelautan*, 17(2). https://doi.org/10.32693/jgk.17.2.2019.614

Kaiho, K., 1994. Benthic foraminiferal dissolved-oxygen index and dissolved-oxygen levels in the modern ocean. *Geology*, 22(8): 719-722.https://doi.org/10.1130/00917613(1994)022%253C0719:BFDOIA%2532.3.CO;2

Kawahata, H., Nishimura, A., Gagan, M.K., 2002. Seasonal change in foraminiferal production in the western equatorial Pacific warm pool: evidence from sediment trap experiments. *Deep-Sea Research II: Topical Studies in Oceanography,* 49(13-14), 2783-2800.

Kuroyanagi, A., Kawahata, H., 2004. Vertical distribution of living planktonic foraminifera in the seas around Japan. *Marine Micropaleontology*, 53: 173–196. https://doi.org/10.1016/j.marmicro.2004.06.001

Ledbetter, M.T., 1986. A Late Pleistocene Time-Series of Bottom Current Speed in the Vema Channel. *Palaeogeography, Palaeoclimatology, Palaeoecology*, 53: 97–105.

Loeblich, A.R., Tappan, H., 1994. *Foraminifera of the Sahul Shelf and Timor Sea, Cushman Foundation Special publication,* 31, Cushman Foundation for Foraminiferal Research. Cambridge, U.S.A., 661p.

Martins, M.V.A., Zaaboub, N., Aleya, L., Frontalini, F., Pereira, E., Miranda, P., Mane, M., Rocha, F., Laut, L., Bour, M.E., 2015. Environmental quality assessment of Bizerte Lagoon (Tunisia) using living foraminifera assemblages and a multiproxy approach. *PLoS ONE*, 10(9), e0137250. https://doi.org/10.1371/journal.pone.0137250

Maryunani, K.A., 2009. *Microfossil Approach Based on Cendrawasih Bay Data, to Interpreting and Reconstructing Equatorial Western Pacific Paleoclimate Since Last Glacial (Late Pleistocene)*. Dissertation, Institut Teknologi Bandung. Unpublished.

Munthe, Y.V., Aryawati, R., Isnaini, 2011. Struktur Komunitas dan Sebaran Fitoplankton di Perairan Sungsang, Sumatera Selatan. *Maspari Journal*, 4(1), 122-130.

Nurruhwati, I., Kaswadji, R., Bengen, D.G., Isnaniawardhani, V., 2012. Kelimpahan Foraminifera Bentik Resen pada Sedimen Permukaan di Perairan Teluk Jakarta. *Jurnal Akuatika*, 3(1): 11–18.

Ortiz, J.D., Mix, A.C., Collier, R.W., 1995. Environmental control of living symbiotic and asymbiotic foraminifera of the California

Current. *Paleoceanography*, 10(6), 987-1009.

Peeters, F.J.C., Brummer, G.-J.A., Ganssen, G., 2001. The effect of upwelling on the distribution and stable isotope composition of *Globigerina bulloides* and *Globigerinoides ruber* (planktic foraminifera) in modern surface waters of the NW Arabian Sea. *Global and Planetary Change*, 34(3-4), 269-291.

Pérez, S.R., Bernasconi, E., Candel, M.S., 2024. Benthic foraminifera diversity from the South Atlantic Ocean: Tierra del Fuego and surrounding waters (South America). *Anais da Academia Brasileira de Ciências*, *96*, e20231342. https://doi.org/10.1590/0001-3765202420231342

Pflaumann, U., Jian, Z., 1999. Modern distribution patterns of planktonic foraminifera in the South China Sea and western Pacific: a new transfer technique to estimate regional sea-surface temperatures. *Marine Geology*, *156*(1-4), 41-83.

Putri, R., 2020. *Rekonstruksi Perubahan Lingkungan Laut Berdasarkan Foraminifera di Perairan Selatan Jawa*. Tesis, Program Pascasarjana, Institut Teknologi Bandung, 87p.

Rathburn, A.E., Corliss, B.H., Tappa, K.D., Lohmannt, K.C., 1996. Comparisons of the ecology and stable isotopic compositions of living (stained) benthic foraminifera from the Sulu and South China Seas. *Deep Sea Research Part I: Oceanographic Research Papers*, *43*(10), 1617-1646.

Ravelo, A.C., Fairbanks, R.G., Philander, S.G.H., 1990. Reconstructing Tropical Atlantic Hydrography Using Planktontic Foraminifera and an Ocean Model. *Paleoceanography*, 5(3), 409-431.

Simanungkalit, Y.A., Pranowo, W.S., Purba, N.P., Riyantini, I., Nurrahman, Y., 2018. Influence of El Niño Southern Oscillation (ENSO) phenomena on Eddies Variability in the Western Pacific Ocean. *IOP Conference Series: Earth and Environmental Science* (Vol. 176, No. 1, p. 012002). IOP Publishing. https://doi.org/10.1088/1755-1315/176/1/012002

Supono, 2008. Analisis Diatom Epipelic sebagai Indikator Kualitas Lingkungan Tambak untuk Budidaya Udang. Thesis, Universitas Diponegoro.

Troelstra, S.R., Kroon, D., 1989. Note on Extant Planktonic Foraminifera from the Banda Sea, Indonesia (Snellius-II Expedition, Cruise G5). *Netherlands Journal of Sea Research,* 24(4), 459-463.

Wollenburg, J.E., Zittier, Z.M.C., Bijma, J., 2018. Insight Into Deep-Sea Life – *Cibicidoides pachyderma* Substrate and pH-dependent Behaviour Following Disturbance. *Deep-Sea Research Part I: Oceanographic Research Papers*, 138: 34–45. https://doi.org/10.1016/j.dsr.2018.07.006

Wyrtki, K., 1987. Indonesian through flow and the associated pressure gradient. *Journal of Geophysical Research: Oceans*, 92: 12941–12946. https://doi.org/10.1029/jc092ic12p12941

Guide for Authors - Geoscience Publications
Bulletin of the Marine Geology

Writing should be submitted according to the following restrictions:

1. Manuscript should be written in English and be submitted online via journal website http://ejournal.mgi.esdm.go.id. Online Submission will be free. The author must login in order to make submission.
2. Manuscript should contains at least 2.000 words and at least 8 pages of manuscript that including embedded figures and tables, without any appendix, and the file should be in Microsoft Office (.doc/.docx) format. It should be prepared in A4 paper (21cm x 29.7cm) using 2.5 cm for left and right margins and 2 cm for top and bottom margins, additionally the paragraph should be used 1 line spacing, 11 TNR.
3. Title, Abstract, and Keywords should be written in English
   - Abstract should be written in English and Bahasa Indonesia version
   - Title should be less than 15 words, title case, small caps, centered, bold, font type Times New Roman (TNR), font size 16, and single spaced.
   - Abstract contains neither pictures nor tables, justified, in 11 TNR, single spaced, and should not exceed 250 words.
   - Keywords contain four to six words/phrases separated with coma and should be justified, 10 TNR and single spaced.
   - Please provide all email address of all authors for our database concern, however, in the published version, only the email address of the first author will be appeared.
4. Manuscript body consists of: Introduction, Method, Result, Discussion, and Conclusion completed by Acknowledgment and References in capital and bold.
5. Heading should be made in four levels. Level five cannot be accepted.
   - Heading 1: title caps, left aligned, bold, 14 TNR, single spaced
   - Heading 2: title case, left aligned, bold, 11 TNR, single spaced
   - Heading 3: title case, left aligned, italic, 11 TNR, single spaced
   - Heading 4 is not recommended, however, it could still be accepted with the format of: sentence case, left indent 5 mm, hanging indent 5 mm, italic, 11 TNR, single spaced
   - Heading 5 cannot be accepted in the manuscript.
6. Figure and table can be either in black and white or in color, they should be clearly readable and in a proportional measure to the overall page. Caption should be numbered, in 9 TNR and single spaced. For lay outing purpose, please provide the respective captioned figure/table with extension .tif/.jpg/.jpeg within a particular folder apart from the manuscript. Please note the figure source/citation/reference if it is taken and/or modified from previous publication.
7. Mathematical equation should be clearly written, numbered orderly, and accompanied with any information needed.
8. Header and footer including page number must not be used. All hypertext links and section bookmarks will be removed from papers. If you need to refer to an Internet email address or URL in your paper, you must type out the address or URL fully in Regular font.
9. Citation and Reference. Following are the detail organization of the references guidelines:
   a. References are written in alphabetical order according to the family name of the first author.
   b. If there is more than one references made by similar author, References are arranged in order of time, and then in alphabetical order.
   c. All the references should be cited in the text. In the text, reference is cited with author family name and the year of publication. If it is written by 2 authors, the family name of both authors are noted, followed by the year of publication, if it is written by more than 2 authors, the reference is cited with the first author family name, followed by *et al.,* and the year of publication. For example: (Kennett, 1981); (Usman and Panuju, 2013); (Susilohadi *et al.*, 2009). Several references are written in alphabetical order, for example: (Kennett, 1981; Susilohadi *et al.,* 2009; and Usman and Panuju, 2013).
   d. References are consist of paper, proceeding, or book that are published, or unpublished report including internal report, dissertation, or thesis.
   e. References can be taken from website, by writing the hyperlink, and the time when it is accessed. Wikipedia, personal blog, or non scientific website is not allowed to be taken into account.

f. References should be ten references in minimum, at least two of them were published in the last five years.

g. Only the family name of the authors are written, followed by the abbreviation of their first name and middle name (if available). If the reference is written by more than one author, all authors should be written, abbreviation (e.g. dkk, *et al,* or drr) is not allowed..

h. All the information of the references must be noted, including publisher, journal volume, number (if available), and page number.

- For book, the book title should be written in italic, for example:

  Kennett, J.P., 1981. *Marine Geology.* Prentice Hall, 813p.

- For periodicals, the name of the journal should be written in italic, for example:

  Susilohadi, S., Gaedicke, C., and Djajadihardja, Y.S., 2009. Structures and sedimentary deposition in the Sunda Strait, Indonesia, *Tectonophysics,* 467 (1): 55-71.

- (Tectonophysics is the name of the journal, 467 is the volume, 1 is issued number, 55 – 71 is page number)

  Usman, E., and Panuju, 2013. Study of Gas Potency Based on Gravity Anomaly Modeling And Seismic Profile Analysis at Banggai-Sula Basin. *Bulletin of the Marine Geology,* 28 (2): 51-60.

- For edited symposia, special issues, etc. published in periodical:

  Kenneth, S. J., 2009. Marine biogeochemistry in 2025. In: D. Glickson (Editor), *Oceanography in 2025: Proceedings of a workshop.* The National Academic Press, Washington D. C.: 130 – 134.

- For websites:

  <http://palaeo-electronica.org/2003_1/benthic/issue1_03.htm> [Accessed on 30 November 2011].

- Unpublished references:

  Darlan, Y., Kamiludin, U., Kurnio, H., Rahardian, R., Hutagaol, J. P., Sianipar, A. H., and Sinaga, A. C., 2005. *Eksplorasi prospektif gas biogenik kelautan di Perairan Muara Kakap dan sekitarnya - Kalimantan Barat.* Pusat Penelitian dan Pengembangan Geologi Kelautan, Bandung, Badan Penelitian dan Pengembangan Energi dan Sumberdaya Mineral, Departemen Energi dan Sumberdaya Mineral. Internal report, 104p. Unpublished.

SERTIFIKAT

Direktorat Jenderal Penguatan Riset dan Pengembangan,
Kementerian Riset, Teknologi, dan Pendidikan Tinggi

RISTEKDIKTI

Kutipan dari Keputusan Direktur Jenderal Penguatan Riset dan Pengembangan,
Kementerian Riset, Teknologi, dan Pendidikan Tinggi Republik Indonesia
Nomor: 21/E/KPT/2018, Tanggal 9 Juli 2018
Tentang Hasil Akreditasi Jurnal Ilmiah Periode I Tahun 2018

Nama Jurnal Imiah

Bulletin of the Marine Geology

E-ISSN: 2527-8843
Penerbit: Puslitbang Geologi Kelautan, Kementerian ESDM

Ditetapkan sebagai Jurnal Ilmiah

TERAKREDITASI PERINGKAT 2

TERAKREDITASI

Akreditasi berlaku selama 5 (lima) tahun, yaitu
Volume 31 Nomor 1 Tahun 2016 sampai Volume 35 Nomor 2 Tahun 2020

Jakarta, 9 Juli 2018
Direktur Jenderal Penguatan Riset dan Pengembangan

Dr. Muhammad Dimyati
NIP. 195912171984021001

MARINE GEOLOGICAL INSTITUTE

GEOLOGICAL AGENCY
MINISTRY OF ENERGY AND MINERAL RESOURCES
Jalan Dr, Junjunan No. 236, Bandung-40174, Indonesia
http://www.mgi.esdm.go.id, E-mail: ejournal.p3gl@gmail.com

ISSN 1410 - 6175
9 771410 617003